LAYER-BY-LAYER ASSEMBLED THIN FILMS
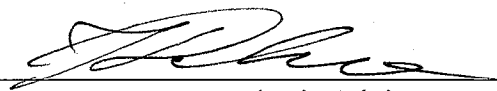
OF NANOCOLLOIDS

By

ARIF AKIFOVICH MAMEDOV

Bachelor of Science
Belarussian State University
Minsk, Belarus
1994

Master of Science
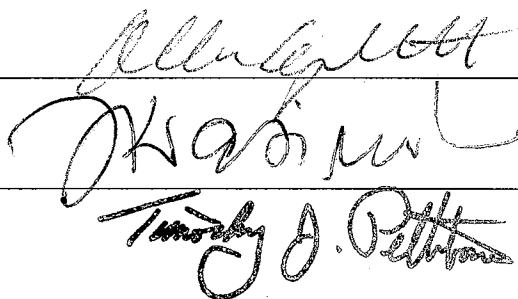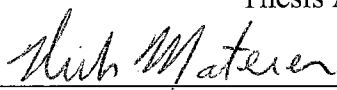Belarussian State University
Minsk, Belarus
1995

Submitted to the Faculty of the
Graduate College of the
Oklahoma State University
in partial fulfillment of
the requirement for
the Degree of
DOCTOR OF PHILOSOPHY
December, 2002

LAYER-BY-LAYER ASSEMBLED THIN FILMS

OF NANOCOLLOIDS

Thesis Approved:

_____

Thesis Advisor

_____

_____

_____

Dean of the Graduate College

DEDICATION

Dedicated
To my two wonderful daughters

ACKNOWLEDGMENTS

TABLE OF CONTENTS

III. LAYER-BY-LAYER ASSEMBLED FILMS OF SEMICONDUCTOR
NANOPARTICLES

LIST OF TABLES

LIST OF FIGURES

Figure   Page

Chapter I

Chapter II

LIST OF SYMBOLS AND ABBREVIATIONS

AFM   Atomic forcr microscopy

C   Clay; sodium nontmorillonite

CA   Cellulose acetate

DI   Deionized

Ga-film   Gallium substrate

H_c Coercivity

HRTEM   High resolution transmission electron microscopy

IR   Infrared

ITO   Indium thin oxide

LBL   Layer-by-layer

M   Magnetite

M_s Saturation magnetization

N Number of deposited bilayers

NC   Nanocolloids

NP   Nanoparticles

O.D.   Optical density

PAA   Poly(acrylic acid)

PAAm   Poly(acryl amide)

PAn   Polyaniline

PDDA   Poly(dimethyldiallylammonium chloride)

PE	Polylectrolyte
PEI-b	Branched poly(ethyleneimine)
PEO	Poly(ethylene oxide)
PET	Poly(ethyleneterephthalate)
PSS	Poly(styrenesulfonate) sodium salt
PVA	Poly(vinyl alcohol)
PVP	Poly(vinyl pyrrolidone)
SEM	Scanning electron microscopy
SWNT	Single wall carbon nanotubes
T	Ultimate tensile stress
TEM	Transmission electron microscopy
TGA	Thioglycolic acid
UV	Ultraviolet
Vis.	Visible
v.%	Volume percent
XPS	X-ray photoelectron spectroscopy
YIG	Yttrium iron garnet
ε	Strain
σ	Stress

CHAPTER I

INTRODUCTION

Over the past two decades, the control of material dimensions at the micrometer and nanometer size scale has been a major point of interest in the materials research area. This interest originated from the fact that the properties of nanomaterials (optical, electrical, mechanical, chemical, *etc.*) are a function of their size, composition, and structural order. Therefore, the ability to prepare nanomaterials with predicted properties and to arrange them in macrosized materials is required in order to meet the ever-increasing demands of nanotechnology.

This thesis focuses on the preparation of advanced organic/inorganic composite thin films from aqueous solutions of nanosized materials, utilizing the method of layer-by-layer (LBL) assembly. LBL assembly has been proven to be a simple and versatile method of multilayer preparation and is widely used for the composition of various complex materials. Since the process occurs in a layer-by-layer mode the control over the structure of the growing film is possible on each deposition step, which allows for the obtaining of films with a high degree of structural organization. This is not achievable by traditional thin film deposition methods, such as sputtering, Langmuir-Blodgett, or spin-coating.

Nanosized inorganic materials

Small particles and colloids with diameters exceeding several micrometers have been studied and used for at least the past several hundred years. However, the science and engineering of nanometer sized particles has developed only in the last two decades. These particles are referred to by many names in the literature. When one refers to particles as a collection of atoms and their non-bulk nature the term "nanoclusters" is used. Single-crystal nanoparticles are often referred to as "nanocrystals". The term "quantum dots" is mostly used for semiconductor particles that exhibit quantum confinement effects. The term "nanoparticles" (NP) will be used in this thesis as a generic term for particles of the nanometer size without connoting a particular structure or property.

Historically, small particles have been important in heterogeneous catalysis where reactants interact at specific sites on the catalyst surface. Their enhanced catalytic activity is achieved through high surface-to-volume ratios and their selectivity through controlled surface features. NP with a significant number of surface atoms continue to receive attention for their catalytic properties.

Magnetic nanoparticle arrays are at the heart of magnetic storage media, such as embedded particles in magnetic tape and segregated grains in magnetic discs [1]. Particles with a $0.1 - 1$ μm diameter have been the mainstay of magnetic storage media. In particles with diameters of about $10 - 20$ nm the spontaneous flip of the magnetization can occur by thermal activation at room temperature (superparamagnetic limit). On the other hand, an increase of magnetic storage density requires the use of smaller particles in magnetic storage devices. Regular well packed arrays of particles are desirable for

achieving the ultimate goal of single-particle-per-bit recording. This is accomplished by producing single domain particles close to the superparamagnetic limit with uniform switching properties [1-5].

Much of the recent interest in nanoparticles has been driven by the quantum confinement effects observed and predicted in small sized particles. Such nanoparticles exhibit spectroscopic features that result from an incomplete band structure caused by the limited number of atoms. Semiconducting nanoparticles have electronic structures between that of the individual atoms and bulk materials. The effect of an incomplete band structure on exciton interactions is an object of particular interest. An exciton is an electron-hole pair that behaves as one particle due to Columbic attractions. It is characterized by a Bohr exciton size. When the size of nanoparticles becomes smaller than the Bohr exciton the spacing between energy levels increases and the band gap widens. Quantum confinement results in a blue-shift of the adsorption edge and a corresponding shift in the photo- and electroluminescence. Therefore, the optical absorption and emission characteristics of semiconducting nanoparticle can be tuned by changing its size. That makes it possible to use them as light-emitting diodes, where one type of semiconductor can be used to produce a whole spectrum of visible light [6-13].

Since a significant number of atoms in a nanoparticle is located at the surface, their surface structure and surface modification have to be considered. Through controlled modification of the surface structure, the desirable properties of nanoparticles can be obtained. One important modification of the nanoparticle surface involves the controlled electronic passivation of the surface. This can be accomplished by the formation core-shell nanoparticles, where a material with a much larger band gap is

chemisorbed on the surface. Either another semiconductor material [14-16] or an organic molecule [17,18] can serve as the shell material.

The surfaces of nanoparticles often need to be modified for compatibility with a host. The preparation of stable aqueous colloidal solutions of NP and the surface interactions between NP and polyelectrolytes (PE) are particularly important in the formation of NP/PE composite materials. One of the possible ways to modify the surfaces on nanoparticles is to attach a charged organic group. The hydrocarbon chain will result in efficient attraction to similar organic groups in the PE through hydrophobic interactions [19], while the surface charge will prevent irreversible coagulation of the nanoparticle colloid. These organic molecules, so called "stabilizers", can be attached to the particles both during synthesis as well as through surface modification of already synthesized NP. The organic molecules form a charged shell around the nanoparticle and prevent their coagulation (Figure 1).

One of the most interesting novel materials discovered in the last decade is the carbon nanotubes, which can be regarded as rolled graphite sheets with as many as a million or more carbon atoms. Due to their similarity to buckyballs, these cylindrical shells of carbon atoms, discovered by Iijima [20], are often called 'buckytubes'[21]. The carbon atoms are arranged in a hexagonal pattern while the closed ends of the nanotube resemble half of a buckyball. The typical diameters for single-wall carbon nanotubes (SWNT) are on the order of 1 - 2 nm [22,23]. Multi-wall carbon nanotubes consisting of concentric shells of increasing diameter can be much larger in diameter [24,25]. The average length of the SWNT can be up to several microns or more.
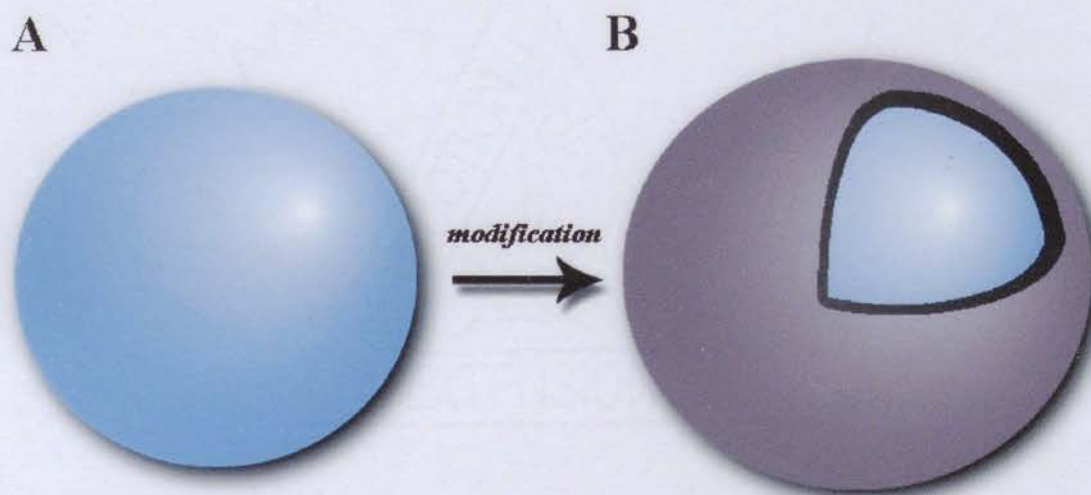
Figure 1. Schematic view of (A) "naked" nanoparticle and (B) particle with the shell of modificator around it.

SWNT self-organize into bundles or 'ropes' consisting of 100 or more tubes in a regular lattice [26-30]. They have the potential to be used as miniature molecular wires [31], and are under development for use in nanoscale electronic devices. The preparation of field-effect transistors consisting of a carbon nanotube deposited over gold contacts have already been developed [32,33]. Besides their intriguing electronic properties, carbon nanotubes also appear to be amongst the strongest fibres known [25] and will be of great potential use in reinforcing other materials.

One drawback of SWNT is their inherently poor solubilization in solvents and polymeric matrices, leading to the phase segregation of SWNT composites. Severe structural inhomogeneities result in the physical separation of the carbon nanotubes when mechanical stress is applied, and hence premature failure of the composite. Uniform distribution of SWNT within the matrix and strong interactions between the matrix and SWNT are believed to be essential requirements for strong SWNT composites. Recent advances in the chemical modification of the surface of SWNT [34-38] afford new approaches to improving the mechanical properties of SWNT composites and to mitigating the solubility problem. Wrapping the SWNT with polymers has also provided a supramolecular approach to the solubilization of them [39].

Layer-by-layer assembly

In 1966, Iler presented a technique for building films of controlled uniform thickness by the alternate adsorption of positively and negatively charged colloidal particles [40]. Afterwards several other singular attempts have been reported [41,42]. However, only after the work of Decher and coworkers with polymer pairs [43-47] LBL

assembly technique has been demonstrated to be a simple and universal method of thin film preparation. This method is based on the consecutive absorption of oppositely charged single molecular layers onto a surface by electrostatic attraction. Besides polymers, this method has been successfully applied to many other systems. These include multilayered films prepared from proteins [48], DNA [49], dyes [50-53], metal and semiconductor nanoparticles [54-63]. The simplicity and universality of LBL method has made it an attractive alternative to many thin film deposition methods, such as Langmuir-Blodget deposition, spin-coating and sputtering.

A schematic representation of a typical LBL deposition cycle is shown in Figure 2. In the initial step (Figure 2 A, step 1) a substrate is immersed in an aqueous colloidal solution of a charged species. Usually a charged polyelectrolyte is used on this first step since it can cover a large area of substrate and can form a uniform distribution of charges on the surface. Upon finishing the deposition, the substrate is rinsed with de-ionized (DI) water to remove all unattached molecules (Figure 2 A, step 2) and transferred into an aqueous dispersion of an oppositely charged species to that used in the initial step (Figure 2 A, step 3). Finally, the substrate is rinsed with DI water (Figure 2 A, step 4). This cycle can be repeated until a film of desired thickness or structure is obtained. The sketch on Figure 2 B shows layer-by-layer growth of the polyelectrolyte/nanoparticle composite film during first two dipping cycles. Some common polyelectrolytes, in particular those of interest to this current work, are shown in Figure 3. Polymers such as PDDA and PSS are referred to as strong polyelectrolytes because the degree of their ionization is high in a wide range of pH. The others, such as
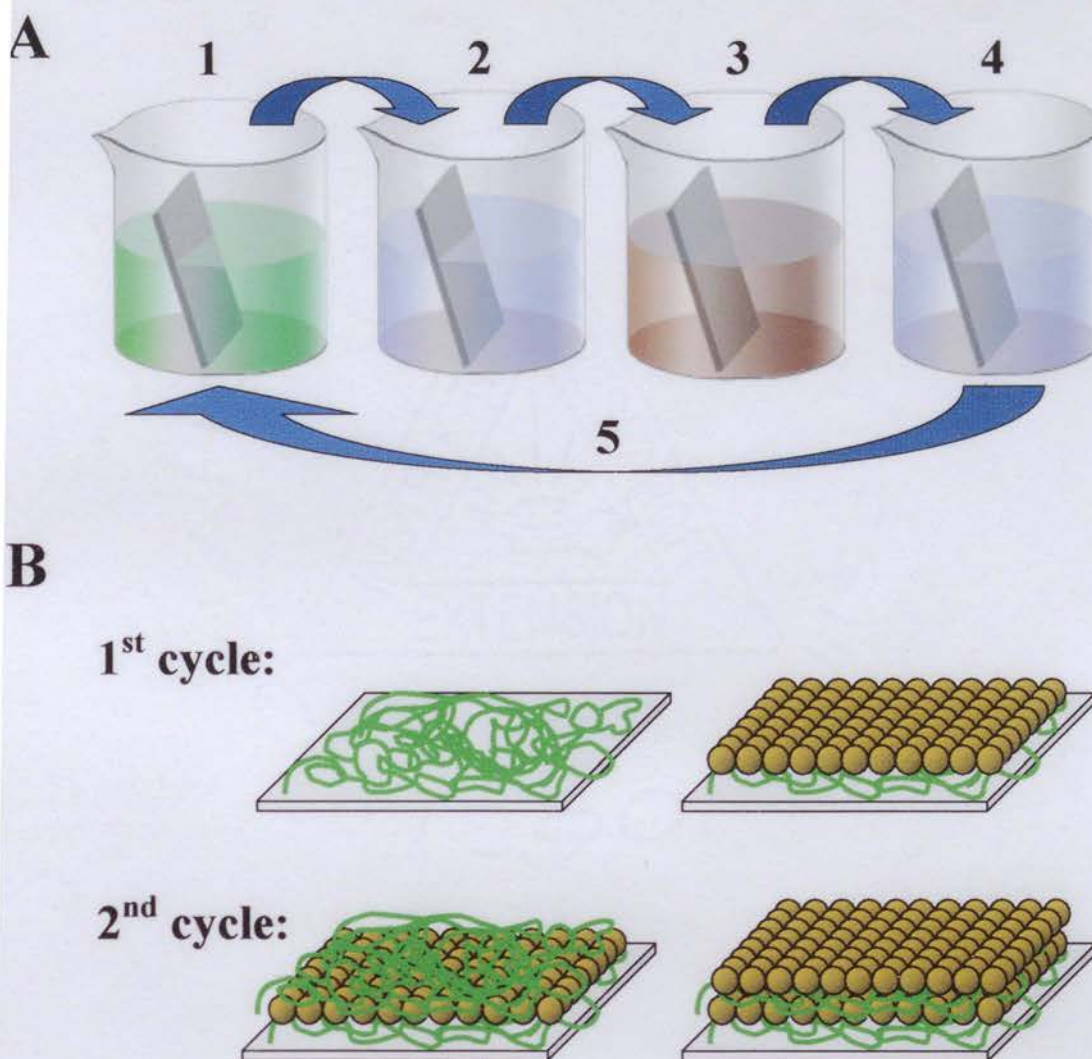
Figure 2. (A) Schematic representation of the LBL deposition cycle: 1 and 3 – deposition of oppositely charged species from their aqueous colloidal solutions, 2 and 4 – washing with DI water, 5 – repetition of dipping cycle. (B) Sketch of the ideal layer-by-layer growth of polyelectrolyte/nanoparticle composite during first two dipping cycles. The interpenetration of the layers into each other is observed in the reality.
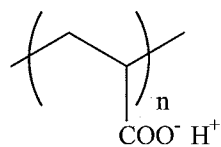
poly(acrylic acid), PAA
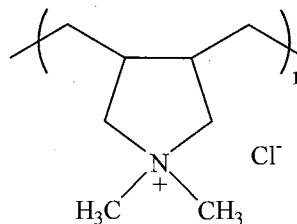
poly(dimethyldiallylammonium chloride), PDDA
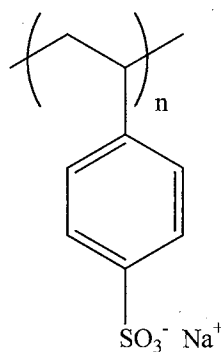
poly(styrenesulfonate) sodium salt, PSS
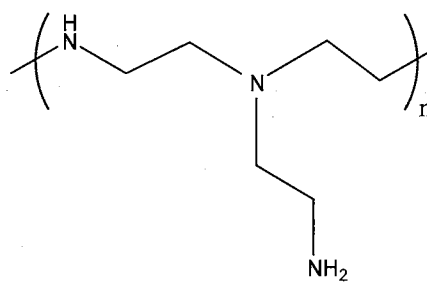
Branched poly(ethyleneimine), PEI-b

Figure 3. Common polyelectrolytes used in LBL assembly. In aqueous dispersions PAA and PSS are polyanions, PDDA and PEI-b are polycations. PAA and PEI-b are weak, while PSS and PDDA are strong.

PAA and PEI-b, are referred to as weak polyelectrolytes since the degree of their ionization is pH dependent.

The growth of a multilayer stack is achieved due to the electrostatic attraction and Van-der-Waals interactions between the oppositely charged components. For a successful LBL process two major requirements have to be fulfilled: (1) colloidal solutions of oppositely charged species have to be used and (2) complete recharge of the surface must be obtained on each deposition step. The latter means that after adsorption of a new layer during LBL deposition the surface charge has to change sign. When both of these demands are satisfied, formation of films with thicknesses from nanometers to micrometers with uniform structures is possible through the layer-by-layer assembly procedure. There seems to be no limitation to the maximum number of layers that can be deposited, and films with up to 1000 layers have been made [64-66]. The coverage area is limited only by the substrate size and polyelectrolyte solution volume. When dried, the obtained films are stable and mechanically strong. The alternations in the dipping sequence allow for the preparation of many different variations on the LBL films. Three-dimensional heterostructures may be created with photolithography, soft-lithography, and inkjet printing techniques [67-73].

LBL assembled polyelectrolyte multilayers

Multilayered films composed of organic compounds on solid substrates have been studied since the mid 20th century for their potential in the preparation of tailored multicomposite materials. Classical methods used for this task, such as Langmuir-

Blodgett and chemisorption, do not provide a diversity in starting materials, since they require certain classes of molecules. It is not surprising, that the initial works on LBL assembly have been done with PE/PE systems [43-47,74]

Polyelectrolyte multilayers can be obtained on many different supports. The roughness of the initially deposited layers will be close to that of the substrate. Nevertheless, continuation in the dipping procedure under carefully chosen conditions will result in the production of a smoother film substrate [75]. The roughness of the obtained PE films also depends on the ionic strength of the solution. The addition of NaCl into an aqueous dispersion of fully ionized strong polyelectrolyte results in the screening of its charges, which leads to coiling and entangling and, consequently, absorption of a thicker PE layer of greater roughness [76,77]. On the other hand, when an already prepared film is immersed in a salt solution it results in its swelling. The degree of swelling is a strong function of the LBL assembly composition and can be explained by the interpenetration of Na^+ and Cl^- ions inside of the film structure. When the ionic strength of the solution is high enough, a smoothing of the film surface is observed [78,79].

When a weak PE is used for LBL stack preparation, the pH of its dispersion becomes the factor affecting the growth process and structure of the obtained film. At a pH range where the polyelectrolyte is fully ionized, formation of smooth thin layers is observed. A shift in the pH value away from its optimum range results in PE molecule entangling. This leads to the formation of a thick film with greater degree of roughness. Figure 4 shows preliminary data obtained by our group that shows the dependence of the surface structures of the (PDDA/PAA)$_5$ multilayer stack assembled in a PDDA dispersion
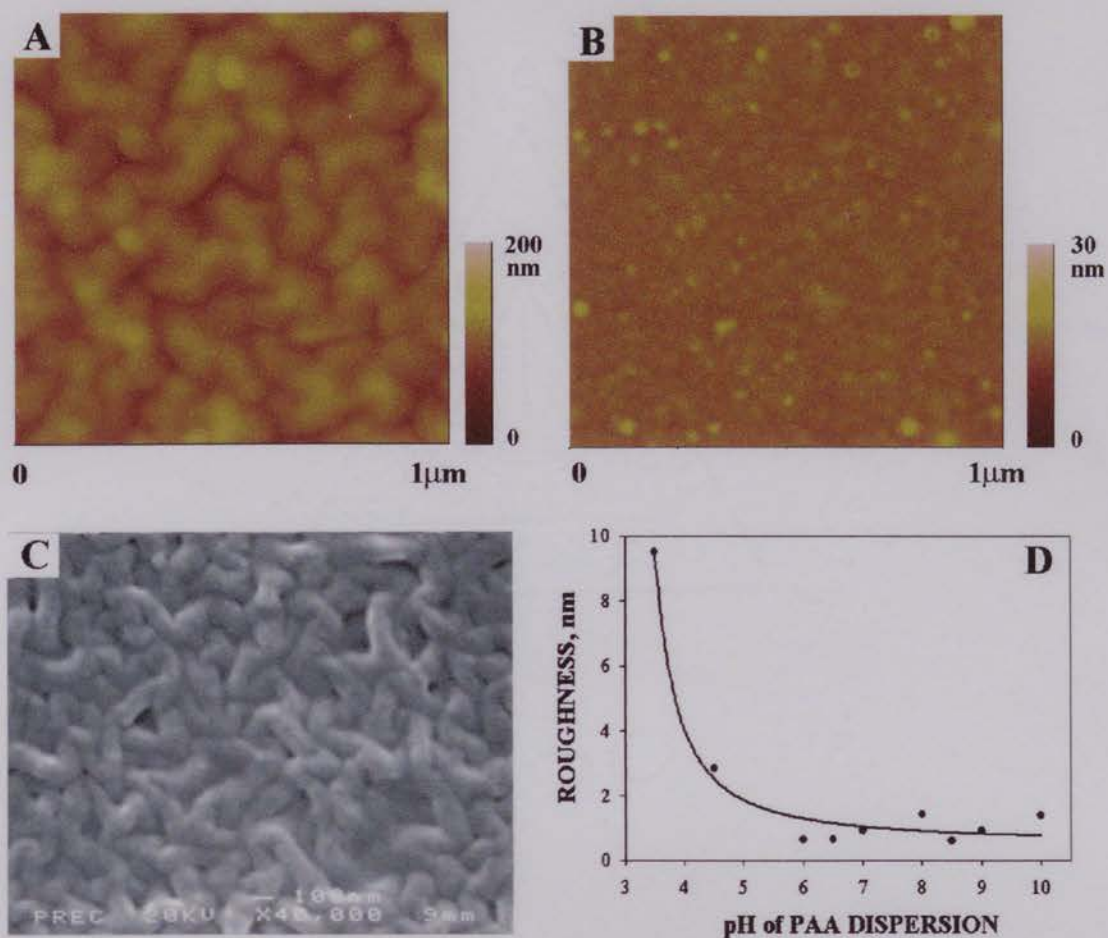
Figure 4. AFM (A, B) and SEM (C) images of (PDDA/PAA)₅ multilayer stacks assembled with pH of PDDA solution equal 6.5 in all samples and pH of PAA equal 3.5 (A, C) and 7.0 (B). (D) Dependence of roughness of (PDDA/PAA)₅ multilayer stacks on pH of the PAA dispersion.

with pH value 6.0 and PAA dispersion with pH values 3.5 (Figure 4 A and C) and 7.0 (Figure 4 B). Note that thin uniform layers are obtained when the pH value of the weak polyelectrolyte PAA adjusted to the range where it is ionized (Figure 4 D). Similar images of the surface structure of a PAA film have been observed by Schlenoff and coworkers [78,79]. The surface properties of PE/PE multilayers have been shown to be determined by the outermost controlled layer. For example, ellipsometry data for PAH/PAA LBL films the advancing shows that the contact angle alternates between 10° and 40° when the outermost layer alternates between PAA and PAH respectively [80].

Even when polyelectrolytes are assembled sequentially onto a surface during an LBL deposition, it has been reported that the structure of the assembled multilayers can be highly interpenetrated [81-85]. PAH/PSS multilayers deposited from salt-containing solutions displayed an interpenetration between the polymer layers on the same order as the individual layer thicknesses [81,82]. These multilayers formed from one pair of PE have been described as "fussy' [47]. However, in multilayers consisting of different pairs of polyelectrolytes, separate layers have a stratified structure [85]. This stratification is consistent with the evidence of interpenetration on the order of an individual layer thickness but not more.

Interactions other than electrostatic between oppositely charged molecules could be used in LBL assembly. The successful growth of films, made of polyaniline (PAn) alternated with nonionic water-soluble polymers, has been demonstrated [86]. The authors presumed that the LBL growth of the films occurred because of hydrogen bonding between PAn and a non-ionic polymer such as poly(vinyl pyrrolidone) (PVP), poly(vinyl alcohol) (PVA), poly(acryl amide) (PAAm), and poly(ethylene oxide) (PEO),

13

which were used in that study. Films have also been prepared with PVP and PAA [87,88]. The formation of hydrogen bonding interactions was identified using infrared (IR) spectroscopy. It is also possible to utilize polymers having respectively electron-donating and electron-accepting perdant groups for layer-by-layer assembly [89].

One more interesting example of multilayered LBL films, formed by interactions other than electrostatic, is in protein multicomponent films. Interactions between the biological molecules or between the biomolecules and the polyelectrolytes are employed in formation of these multilayers. It has been reported that immunoglobulin G can be assembled with anionic PSS at pH values above and below its isoelectric point. This fact reflects the non-electrostatic nature of the LBL process [90]. In addition, the LBL deposition of avidin and biotin-labeled polyamines creates a multilayered structure through avidin-biotin complexation [48,91-93] even in the presence of electrostatic repulsion arising from the net positive charges of the avidin (isoelectric point at pH 9.0-10.0) and polyamines [91,92].

Polyelectrolyte/inorganic multilayers: synthesis within PE/PE film

Utilization of the LBL method gives the opportunity to produce a large variety of PE/PE films with fine control over their structure by modulating the adsorption conditions and by choosing polyelectrolytes with desired properties. The availability of non-ionized groups of PE inside of the prepared assemblies as well as the possibility of swelling in the resulting films gives an opportunity to use them as nanoreactors for the *in situ* synthesis of inorganic nanoparticles.

14

The synthesis of cobalt hydroxide ($Co(OH)_2$), iron oxyhydroxide (β- and γ-FeOOH) and lead sulfide (PbS) nanoparticles has been accomplished by Stroeve and coworkers utilizing strong PDDA/PSS multilayers [94,95]. When an LBL stack was immersed in a solution of precursor nitrate or chloride salts, the metal cations bound to the sulfonate groups. Upon oxidation or sulfidation of films saturated with precursor salts, the formation of nanoparticles was observed. Repetition of the binding and reaction steps resulted in enlargement of the nanoparticles. However, even though the possibility of forming various inorganic materials has been shown, use of multilayers formed by strong PE is limited by the relative lack of free binding groups. By utilizing weak polyelectrolytes such as PAH or PAA for multilayer preparation, it becomes possible to form non-ionized groups inside of the stack. This is achieved by assembling a weak polycation from a basic solution with a weak polyanion from an acidic solution [8].

Polyelectrolyte/inorganic multilayers:

LBL assembly of PE/inorganic multilayers

The *in situ* synthesis of inorganic nanomaterials provides a simple way of preparing composite organic/inorganic materials. However, utilization of this method does not provide total control over the structure of the resulting material. When a film in which the inorganic content changes from one side to another is desired another technique should be considered.

The LBL assembly method has been extended to the preparation of hybrid organic/inorganic films. Exfoliated clay materials, metal oxide, semiconductor and metallic nanoparticles have been utilized for this task [15,55,63,76,96-103]. The common

15

requirement for a successful assembly of these materials is the presence of charge bearing groups on the inorganic surface. If the surface is uncharged, additional surface treatment is required.

The first investigations of the assembly of negatively charged exfoliated minerals, such as hectorite, α-zirconium phosphate or montmorillonite, have shown that they can be assembled using positively charged polyelectrolytes, such as PDDA or poly(allylamine hydrochloride) [76,96-99]. It is also important that the sheets were found to adsorb parallel to the surface covering large areas of the previously adsorbed layer.

The LBL growth of the film built from metal oxide nanoparticles, proceeds in a linear fashion. The thickness of the adsorbed layer increases with a higher ionic strength of the solution. Nanoparticles with negatively charged surfaces, like silica or titania at high pH, could be assembled with a positively charged polyelectrolyte, such as PDDA and PEI. It was also demonstrated in the same work that the surface charge of pure silica colloids can controlled by wrapping them in PDDA before the LBL assembly process [104]. Positively charged metal oxide nanoparticles such as ceria and titania can be assembled with negatively charged polyelectrolytes, like PAA and PSS in acidic media [55,65,105].

Contrary to metal oxide nanoparticles, which generally have surface charge, metallic and semiconductor NP synthesized in solution, are not charged. In such a case, the choice of the stabilizing agent is important for the formation of charged nanostructures. Several reports on the LBL assembly of acid-stabilized metallic and semiconductor nanoparticles have been published [55,106]. Furthermore, alternating

PE/NP bilayers with PE/PE spacers allows for the preparation of distinctly layered composite structures.

As in case of PE/PE multilayers, the growth of the inorganic nanomaterial containing films can be obtained through non-electrostatic interactions [107]. Hydrogen-bonding, protein-antibody interactions *etc.* are possible, when the surface of the inorganic component is modified with a corresponding stabilizing or coordinating agent.

Substrates for layer-by-layer assembly

A layer-by-layer assembly process can be performed on a wide variety of substrates. Most LBL multilayers have been build on glass, silicon, quartz , and indium-tin-oxide (ITO), since these substrates are particularly well suited for a number of experimental techniques. Another advantage of their use is that their surface physico-chemistry has been well studied, and convenient procedures for cleaning and charging the surface can be found in the literature. When hydroxyl groups are present, the correct choice of pH is needed to generate a surface charge. Another way to increase surface charge, which is often referred to in this current work, is to adsorb a pair of polyelectrolytes to form a precursor bilayer for further multilayer assembly [60].

Obviously, LBL assembly is not limited to the substrates mentioned above. A number of other substrates have been used for multilayer films preparation. Among the metals, gold has been widely used. Successful growth of LBL films on bare gold surfaces as well as surfaces charged with chemisorption of alkanethiols have been reported [90,108]. Examples of other metals that have been successfully used are platinum [109], silver [110], and aluminum [76]. For the latter, the surface must be assumed to consist of

aluminum oxide. Multilayers have been successfully assembled on polymer substrates [111-113]. Successful assembly on this type of substrate is obtained either by chemical modification of the polymer surface or by functionalization of the substrate. Two of these substrates, namely poly(ethyleneterephthalate) (PET) and cellulose acetate (CA) have been used in the work, presented here.

The LBL process is not limited to flat substrates. For almost a decade this method have been successfully applied to the preparation of core-shell colloidal particles, in which the surface of the colloidal particle is modified by the adsorption of uniform single- and multilayers of PE, or PE/NP [114-124]. Furthermore, the core particle can be removed by controlled destruction which yields a hollow capsule [118,122,123,125-131]. Such capsules have a multitude of possible applications ranging from drug delivery to advanced catalytic materials [123,129,132-134].

Purpose and thesis outline

The previous discussion provided a brief account of state-of-the-art of LBL deposition method. The possibility of control of the growing film at each adsorption step has been emphasized. Large variety of organic and inorganic nanomaterials opens the doors for the preparation of films with wide spectra of possible applications ranging from advanced catalytic materials to artificial biological membranes. Although LBL deposition method has been declared to be a simple and versatile, there are no universal conditions for film preparation. Each of the colloidal dispersions used in this process requires individual approach when high quality films are needed. There is a continual interest and

need in tuning the properties and structure of the LBL multilayers as well as in understanding of actual interactions and arrangements of the separate interlayers.

This work focuses on the preparation and characterization of thin films from nanocolloids utilizing layer-by-layer assembly method. The goals of this work are (1) to understand the growth conditions for multilayers of various nanocolloids; (2) to prepare complex films and estimate the influence of their internal structure on their properties; and (3) to develop a methods of free-standing film preparation Successful fulfillment of these goals demonstrates the capabilities of the LBL assembly method in thin film preparation and realizes its advantages for the preparation of the complex structures based on inorganic nanomaterials and organic polyelectrolytes.

The research, presented in this work is subdivided into the following parts: Chapter II describes the LBL growth mechanism of magnetic Fe_3O_4 (magnetite) and yttrium iron garnet (YIG) nanoparticles. Magnetic measurements of the obtained multilayers of magnetite are also presented in this Chapter. Chapter III explores the features in the preparation of graded films of semiconductor thiol stabilized CdTe nanoparticles. The conditions for the successful growth of single wall carbon nanotube multilayers and the alignment of SWNT inside of the monolayer are discussed in Chapter IV. Preparation of free-standing films from materials by LBL assembly method and the study of the mechanical properties of obtained films are presented in Chapter V. The final Chapter concludes this work and suggests some future research directions.

References

1. Himpsel, F. J.; Ortega, J. E.; Mankey, G. J.; Willis, R. F. *Advances in Physics* **1998,** *47*(4), 511-597.

2. New, R. M. H.; Pease, R. F. W.; White, R. L. *Journal of Vacuum Science & Technology, B: Microelectronics and Nanometer Structures* **1994,** *12*(6), 3196-3201.

3. Lederman, M.; Schultz, S.; Ozaki, M. *Phys.Rev.Lett.* **1994,** *73*(14), 1986-1989.

4. New, R. M. H.; Pease, R. F. W.; White, R. L. *Journal of Vacuum Science & Technology, B: Microelectronics and Nanometer Structures* **1995,** *13*(3), 1089-1094.

5. Hehn, M.; Ounadjela, K.; Bucher, J. P.; Rousseaux, F.; Decanini, D.; Bartenlian, B.; Chappert, C. *Science* **1996,** *272*(5269), 1782-1785.

6. Sattler, K. *The energy gap of clusters, nanoparticles, and quantum dots;* 2002.

7. Kumbhojkar, N.; Kshirsagar, A. *Optical properties of II-VI semi-conducting quantum dots;* **2001.**

8. Wang, T. Polyelectrolyte multilayers as nanostructured templates for inorganic synthesis. *PhD thesis.* **2002,** Massachusetts Institute of Technology.

9. Talapin, D. V.; Rogach, A. L.; Mekis, I.; Haubold, S.; Kornowski, A.; Haase, M.; Weller, H. *Colloids and Surfaces, A: Physicochemical and Engineering Aspects* **2002,** *202*(2-3), 145-154.

10. Talapin, D. V.; Haubold, S.; Rogach, A. L.; Kornowski, A.; Haase, M.; Weller, H. *Journal of Physical Chemistry B* **2001,** *105*(12), 2260-2263.

11. Ingert, D.; Motte, L.; Pileni, M. P. *Surfactant Science Series* **2000,** *92*(Fine Particles), 217-234.

12. Gaponik, N. P.; Talapin, D. V.; Rogach, A. L.; Eychmuller, A. *Journal of Materials Chemistry* **2000,** *10*(9), 2163-2166.

13. Gao, M.; Kirstein, S.; Rogach, A. L.; Weller, H.; Mohwald, H. *Advances in Science and Technology (Faenza, Italy)* **1999,** *27*(Innovative Light Emitting Materials), 347-358.

14. Aliev, F.; Correa-Duarte, M.; Mamedov, A.; Ostrander, J. W.; Giersig, M.; Liz-Marzan, L.; Kotov, N. *Adv.Mater.* **1999,** *11*(12), 1006-1010.

15. Pastoriza-Santos, I.; Koktysh, D. S.; Mamedov, A. A.; Giersig, M.; Kotov, N. A.; Liz-Marzan, L. M. *Langmuir* **2000,** *16*(6), 2731-2735.

16. Mayya, K. S.; Gittins, D. I.; Caruso, F. *Chem. Mater.* **2001,** *13*(11), 3833-3836.

17. Pastoriza-Santos, I.; Scholer, B.; Caruso, F. *Adv. Funct. Mater.* **2001,** *11*(2), 122-128.

18. Kotov, N. A.; Liz-Marzan, L. M. WO 0044507, **2000,** pp. 24.

19. Kotov, N. A. *Nanostructured Materials* **1999,** *12* 789-796.

20. Iijima, S. *Nature* **1991,** *354* 56-58.

21. Smalley, R. E. *Buckytubes! - new materials and new devices from carbon;* 1998.

22. Collins, P. G.; Zettl, A.; Bando, H.; Thess, A.; Smalley, R. E. *Science* **1997,** *278*(5335), 100-103.

23. Kaiser, A. B. *Reports on Progress in Physics* **2001,** *64*(1), 1-49.

24. Ajayan, P. M. *Progress in Crystal Growth and Characterization of Materials* **1997,** *34*(1-4), 37-51.

25. Ajayan, P. M.; Ebbesen, T. W. *Reports on Progress in Physics* **1997,** *60*(10), 1025-1062.

26. Amelinckx, S.; Lucas, A.; Lambin, P. *Reports on Progress in Physics* **1999,** *62*(11), 1471-1524.

27. Rols, S.; Anglaret, E.; Sauvajol, J. L.; Coddens, G.; Dianoux, A. J. *Applied Physics A: Materials Science & Processing* **1999,** *69*(6), 591-596.

28. Gennett, T.; Dillon, A. C.; Alleman, J. L.; Jones, K. M.; Hasoon, F. S.; Heben, M. J. *Chemistry of Materials* **2000,** *12*(3), 599-601.

29. Huang, H.; Kajiura, H.; Tsutsui, S.; Hirano, Y.; Miyakoshi, M.; Yamada, A.; Ata, M. *Chemical Physics Letters* **2001,** *343*(1,2), 7-14.

30. Zhu, H.; Jiang, B.; Xu, C.; Wu, D. *Chemical Communications* **2002,**(17), 1858-1859.

31. Dekker, C. *Physics Today* **1999,** *52*(5), 22-28.

32. Tans, S. J.; Verschueren, A. R. M.; Dekker, C. *Nature* **1998,** *393*(6680), 49-52.

33. Tans, S. J.; Dekker, C. *Nature* **2000,** *404*(6780), 834-835.

34. Tagmatarchis, N.; Georgakilas, V.; Prato, M.; Shinohara, H. *Chemical Communications* **2002,**(18), 2010-2011.

35. Georgakilas, V.; Kordatos, K.; Prato, M.; Guldi, D. M.; Holzinger, M.; Hirsch, A. *Journal of the American Chemical Society* **2002,** *124*(5), 760-761.

36. Tans, S. J.; Devoret, M. H.; Groeneveld, R. J. A.; Dekker, C. *Nature* **1998,** *394*(6695), 761-764.

37. Yao, Z.; Postma, H. W. C.; Balents, L.; Dekker, C. *Nature* **1999,** *402*(6759), 273-274.

38. Postma, H. W. C.; Teepen, T.; Yao, Z.; Grifoni, M.; Dekker, C. *Science* **2001**, *293*(5527), 76-79.

39. Smalley, R. E.; Colbert, D. T.; Smith, K. A.; O'Connell, M. WO 0216257, **2001**, pp. 39.

40. Iler, I. J. *J.Colloid Interface Sci.* **1966**, *21* 569.

41. Golander, C. G.; Arwin, H.; Eriksson, J. C.; Lundstrom, I.; Larsson, R. *Colloids Surf.* **1982**, *5*(1), 1-16.

42. Tredgold, R. H.; Winter, C. S.; El Badawy, Z. I. *Electron.Lett.* **1985**, *21*(13), 554-555.

43. Decher, G.; Hong, J. D. *Macromol.Chem., Macromol.Symp.* **1991**, *46* 321.

44. Decher, G.; Hong, J. D. *Ber.Bunsen-Ges.Phys.Chem.* **1991**, *95* (11), 1430-1434.

45. Lvov, Y.; Decher, G.; Moehwald, H. *Langmuir* **1993**, *9*(2), 481-486.

46. Lvov, Y.; Haas, H.; Decher, G.; Moehwald, H.; Kalachev, A. *J. Phys. Chem.* **1993**, *97*(49), 12835-12841.

47. Decher, G. *Science* **1997**, *277* 1232-1237.

48. Hong, J. D.; Lowack, K.; Schmitt, J.; Decher, G. *Prog.Colloid Polym.Sci.* **1993**, *93*(TRENDS IN COLLOID AN), 98-102.

49. Lvov, Y.; Decher, G.; Sukhorukov, G. *Macromolecules* **1993**, *26*(20), 5396-5399.

50. Advincula, R. C.; Baba, A.; Kaneko, F. *Polym.Mater.Sci.Eng.* **1999**, *81* 95-96.

51. Dai, Z., Sr.; Donath, E.; Moewald, H. *Layer-by-layer self-assembly of polyelectrolytes and dyes*; 2001.

52. Koetse, M.; Laschewsky, A.; Verbiest, T. *Mater.Sci.Eng., C* **1999**, *C10*(1-2), 107-113.

53. Laschewsky, A.; Wischerhoff, E.; Kauranen, M.; Persoons, A. *Macromolecules* **1997,** *30*(26), 8304-8309.

54. Fendler, J. H.; Meldrum, F. C. *Adv. Mater..* **1995,** *7* 607-632.

55. Kotov, N. A.; Dekany, I.; Fendler, J. H. *J. Phys. Chem.* **1995,** *99* 13065-13069.

56. Fendler, J. H. *Chem. Mater.* **1996,** *8* 1616-1624.

57. Fendler, J. H.; Kotov, N. A.; Dekany, I. *NATO ASI Ser., Ser.3* **1996,** *12*(Fine Particles Science and Technology), 557-577.

58. Kotov, N. A.; Dekany, I.; Fendler, J. H. *Adv. Mater.* **1996,** *8*(8), 637-641.

59. Fendler, J. H. *Curr .Opin. Solid State Mat. Sci.* **1997,** *2* 365-369.

60. Fendler, J. J. *Studies in Surface Science and Catalysis* **1997,** *103*(Semiconductor Nanoclusters: Physical, Chemical, and Catalytic Aspects), 261-276.

61. Li, M.; Schnablegger, H.; Mann, S. *Nature* **1999,** *402*(6760), 393-395.

62. Susha, A. S.; Caruso, F.; Rogach, A. L.; Sukhorukov, G. B.; Kornowski, A.; Mohwald, H.; Giersig, M.; Eychmuller, A.; Weller, H. *Colloids Surf., A* **2000,** *163*(1), 39-44.

63. Liang, X.; Kotov, N. A. *Layer-by-Layer Assembly of Indium Sulfide-Based Nanoparticles*; 2002.

64. Liu, Y. J.; Wang, A. B.; Claus, R. *J. Phys. Chem. B* **1997,** *101* 1385-1388.

65. Liu, Y. J.; Wang, A. B.; Claus, R. O. *Appl. Phys. Lett.* **1997,** *71* 2265-2267.

66. Lenahan, K. M.; Wang, Y. X.; Liu, Y.; Claus, R. O.; Heflin, J. R.; Marciu, D.; Figura, C. *Adv. Mater.* **1998,** *10*(11), 853-855.

67. Jiang, X.; Hammond, P. T. *Langmuir* **2000,** *16*(22), 8501-8509.

68. Clark, S. L.; Hammond, P. T. *Adv. Mater.* **1998,** *10*(18), 1515-1519.

69. Clark, S. L.; Handy, E. S.; Rubner, M. F.; Hammond, P. T. *Polym. Prepr. (Am. Chem. Soc., Div. Polym. Chem.)* **1998,** *39*(2), 1079-1080.

70. Clark, S. L.; Montague, M. M.; Hammond, P. T. *Polym. Mater. Sci. Eng.* **1997,** *77* 400-401.

71. Rubner, M. *Tuning Optical Properties at the Molecular and Supramolecular Level*; **2002.**

72. Berg, M. C.; Mendelsohn, J. D.; Yang, S. Y.; Hammond, P. T.; Rubner, M. F. *Controlling cell adhesion on polyelectrolyte multilayers through micropatterning*; 2002.

73. Kim, H.; Hammond, P. T.; Cohen, R. E.; Rubner, M. F. *Multiscale patterned polymer thin film surfaces for directed cell growth*; 2002.

74. Decher, G.; Maclennan, J.; Reibel, J.; Sohling, U. *Adv. Mater.* **1991,** *3*(12), 617-619.

75. Decher, G.; Lvov, Y.; Schmitt, J. *Thin Solid Films* **1994,** *244*(1-2), 772-777.

76. Keller, S. W.; Kim, H. N.; Mallouk, T. E. *J. Am. Chem. Soc.* **1994,** *116*(19), 8817-8818.

77. Loesche, M.; Schmitt, J.; Decher, G.; Bouwman, W. G.; Kjaer, K. *Macromolecules* **1998,** *31*(25), 8893-8906.

78. Dubas, S. T.; Schlenoff, J. B. *Macromolecules* **1999,** *32*(24), 8153-8160.

79. Dubas, S. T.; Schlenoff, J. B. *Langmuir* **2001,** *17*(25), 7725-7727.

80. Shiratori, S. S.; Rubner, M. F. *Macromolecules* **2000,** *33*(11), 4213-4219.

81. Schmitt, J.; Grünewald, T.; Decher, G.; Pershan, P. S.; Kjaer, K.; Lösche, M. *Macromolecules* **1993,** *26*(25), 7058-7063.

82. Loesche, M.; Schmitt, J.; Bouwman, W. G.; Kjaer, K.; Decher, G. *Internal structure of molecularly layered polyelectrolyte interface films*; 1996.

83. Kellogg, G. J.; Mayes, A. M.; Stockton, W. B.; Ferreira, M.; Rubner, M. F.; Satija, S. K. *Langmuir* **1996,** *12* 5109-5113.

84. Rodriguez, L. N. J.; De Paul, S. M.; Barrett, C. J.; Reven, L.; Spiess, H. W. *Adv. Mater.* **2000,** *12*(24), 1934-1938.

85. Baur, J. W.; Rubner, M. F.; Reynolds, J. R.; Kim, S. *Langmuir* **1999,** *15*(19), 6460-6469.

86. Stockton, W. B.; Rubner, M. F. *Macromolecules* **1997,** *30* 2717-2725.

87. Wang, L.; Fu, Y.; Wang, Z.; Fan, Y.; Zhang, X. *Langmuir* **1999,** *15* 1360.

88. Wang, L.; Wang, Z.; Zhang, X.; Shen, J.; hi, L.; uchs, H. *Macromol. Rapid Commun.* **1997,** *18*(509).

89. Shimazaki, Y.; Mitsuishi, M.; Ito, S.; Yamamoto, M. *Langmuir* **1998,** *14* 2768-2773.

90. Caruso, F.; Niikura, K.; Furlong, D. N.; Okahata, Y. *Langmuir* **1997,** *13*(13), 3427-3433.

91. Anzai, J. i.; Nishimura, M. *Journal of the Chemical Society, Perkin Transactions 2: Physical Organic Chemistry* **1997,**(10), 1887-1889.

92. Anzai, J. i.; Kobayashi, Y.; Nakamura, N.; Nishimura, M.; Hoshi, T. *Langmuir* **1999,** *15*(1), 221-226.

93. Cassier, T.; Lowack, K.; Decher, G. *Supramolecular Science* **1998,** *5*(3-4), 309-315.

94. Dante, S.; Hou, Z.; Risbud, S.; Stroeve, P. *Langmuir* **1999,** *15*(6), 2176-2182.

95. Dutta, A. K.; Jarero, G.; Zhang, L.; Stroeve, P. *Chem. Mater.* **2000,** *12*(1), 176-181.

96. Kleinfeld, E. R.; Ferguson, G. S. *Science* **1994,** *265* 370-373.

97. Ferguson, G.; Kleinfeld, E. *Chem. Mater.* **1996,** *8*(8), 1575-1578.

98. Lvov, Y.; Ariga, K.; Ichinose, I.; Kunitake, T. *Langmuir* **1996,** *12* 3038-3044.

99. Kotov, N. A.; Haraszti, T.; Turi, L.; Zavala, G.; Geer, R. E.; Dekany, I.; Fendler, J. H. *J. Amer. Chem. Soc.* **1997,** *119* 6821-6832.

100. Cassagneau, T.; Fendler, J. H. *J. Phys. Chem. B* **1999,** *103*(11), 1789-1793.

101. Yonezawa, T.; Shimokawa, H.; Sutoh, M.; Onoue, S. y.; Kunitake, T. *Stud. Surf. Sci. Catal.* **2001,** *132* (Proceedings of the International Conference on Colloid and Surface Science, 2000), 619-622.

102. Mukherjee, P.; Kumar, A.; Mandale, A. B.; Kumar, R.; Sastry, M. *Abstr. Pap.- Am. Chem. Soc.* **2001,** *221st* CATL-071.

103. McKenzie, K. J.; Marken, F.; Hyde, M.; Compton, R. G. *New Journal of Chemistry* **2002,** *26*(5), 625-629.

104. Lvov, Y.; Ariga, K.; Onda, M.; Ichinose, I.; Kunitake, T. *Langmuir* **1997,** *13*(23), 6195-6203.

105. Liu, Y.; Wang, A.; Claus, R. O. *Appl. Phys. Lett.* **1997,** *71*(16), 2265-2267.

106. Schmitt, J.; Decher, G.; Dressick, W. J.; Brandow, S. L.; Geer, R. E.; Shashidhar, R.; Calvert, J. M. *Adv. Mater.* **1997,** *9*(1), 61-65.

107. Hao, E.; Lian, T. *Materials Research Society Symposium Proceedings* **2001,** *648*(Growth, Evolution and Properties of Surfaces, Thin Films and Self-Organized Structures), 6.

108. Nuzzo, R. G.; Allara, D. L. *J. Am. Chem. Soc.* **1983**, *105*(13), 4481-4483.

109. Meldrum, F. C.; Kotov, N. A.; Fendler, J. H. *Chem. Mater.* **1995**, *7*(6), 1112-1116.

110. Lvov, Y.; Ariga, K.; Kunitake, T. *Chem. Lett.* **1994**,(12), 2323-2326.

111. Laschewsky, A.; Wischerhoff, E.; Denzinger, S.; Ringsdorf, H.; Delcorte, A.; Bertrand, P. *Chem.--Eur.J.* **1997**, *3*(1), 34-38.

112. Delcorte, A.; Bertrand, P.; Wischerhoff, E.; Laschewsky, A. *Langmuir* **1997**, *13*(19), 5125-5136.

113. Kim, H.; Urban, M. W. *Langmuir* **1998**, *14*(25), 7235-7244.

114. Caruso, F.; Donath, E.; Moehwald, H. *J. Phys. Chem. B* **1998**, *102*(11), 2011-2016.

115. Sukhorukov, G. B.; Donath, E.; Lichtenfeld, H.; Knippel, E.; Knippel, M.; Budde, A.; Mohwald, H. *Colloid Surface A* **1998**, *137* 253-266.

116. Sukhorukov, G. B.; Donath, E.; Davis, S.; Lichtenfeld, H.; Caruso, F.; Popov, V. I.; Mohwald, H. *Polym. Advan. Technol.* **1998**, *9* 759-767.

117. Caruso, F.; Lichtenfeld, H.; Donath, E.; Moehwald, H. *Macromolecules* **1999**, *32*(7), 2317-2328.

118. Caruso, F.; Schueler, C.; Kurth, D. G. *Chem. Mater.* **1999**, *11*(11), 3394-3399.

119. Caruso, F.; Susha, A. S.; Giersig, M.; Mohwald, H. *Adv. Mater.* **1999**, *11*(11), 950-953.

120. Caruso, F. *Adv. Mater.* **2001**, *13*(1), 11-22.

121. Caruso, F.; Shi, X.; Caruso, R. A.; Susha, A. *Adv. Mater.* **2001**, *13*(10), 740-744.

122. Caruso, R. A.; Susha, A.; Caruso, F. *Chem. Mater.* **2001**, *13* (2), 400-409.

123. Sukhorukov, G. B.; Antipov, A. A.; Voigt, A.; Donath, E.; Mohwald, H. *Macromol. Rapid Commun.* **2001,** *22*(1), 44-46.

124. Sukhorukov, G. B. *Studies in Interface Science* **2001,** *11*(Novel Methods to Study Interfacial Layers), 383-414.

125. Caruso, F.; Caruso, R. A.; Mohnwald, H. *Science* **1998,** *282*(5391), 1111-1114.

126. Caruso, F.; Caruso, R. A.; Moehwald, H. *Chem. Mater.* **1999,** *11*(11), 3309-3314.

127. Donath, E.; Sukhorukov, G. B.; Lerche, K. H.; Voigt, A.; Baeumler, H.; Caruso, F.; Moehwald, H. WO 9947252, **1999,** pp. 72.

128. Gittins, D. I.; Caruso, F. *Adv. Mater.* **2000,** *12*(24), 1947-1949.

129. Voigt, A.; Buske, N.; Sukhorukov, G. B.; Antipov, A. A.; Leporatti, S.; Lichtenfeld, H.; Baumler, H.; Donath, E.; Mohwald, H. *J. Magn. Magn. Mater.* **2001,** *225*(1-2), 59-66.

130. Yang, W.; Trau, D.; Renneberg, R.; Yu, N. T.; Caruso, F. *J. Colloid Interface Sci.* **2001,** *234*(2), 356-362.

131. Sukhorukov, G. B. *Microspheres, Microcapsules & Liposomes* **2002,** *5* (Dendrimers, Assemblies, Nanocomposites), 111-147.

132. Antipov, A. A.; Sukhorukov, G. B.; Donath, E.; Moehwald, H. *J. Phys. Chem. B* **2001,** *105*(12), 2281-2284.

133. Qiu, X.; Leporatti, S.; Donath, E.; Moehwald, H. *Langmuir* **2001,** *17*(17), 5375-5380.

134. Sukhorukov, G.; Dahne, L.; Hartmann, J.; Donath, E.; Mohwald, H. *Adv. Mater.* **2000,** *12*(2), 112-115.

CHAPTER II

LAYER-BY-LAYER ASSEMBLED FILMS OF MAGNETIC NANOPARTICLES[i]

Introduction

Nanocomposite materials, prepared from inorganic nanoparticles embedded within a polymer matrix, have attracted much interest over the past decade for their broad range of potential applications as catalysts, optical devices, sensors, and drug delivery systems. As it was discussed in Chapter 1, nanometer-sized inorganic particles have unique properties due to the quantum size effect and their large surface area to volume ratio. Utilization of layer-by-layer (LBL) assembly for the preparation of hybrid organic/inorganic thin films has been demonstrated to be a simple, but versatile method [1-8].

The study described in this chapter devoted to the preparation and characterization of polyelectrolyte (PE)/magnetic nanoparticles (NP) hybrid materials. Inorganic magnetic components NP of magnetite (Fe_3O_4) and yttrium iron garnet ($Y_3Fe_5O_{12}$, YIG) have been employed. The positively charged poly(dimethyldiallylammonium chloride) (PDDA) and negatively charged

---

poly(styrenesulfonate) sodium salt (PSS) or poly(acrylic acid) (PAA) were utilized as the organic components of the composites.

Magnetic nanoparticles are used for the assembly of thin films because the preparation of homogeneous functional magnetic materials would yield a high possibility of the discovery of novel magnetic, magnetooptical, and magnetoresistive phenomena in these systems. Besides, LBL method, unlike other methods, can be used to control magnetic interactions in the films.

The LBL approach allows for the design and simple realization of complex structures of hybrid PE/NP myltilayers. However, in the case of the NP assemblies, the possibility is compromised by the high roughness of the films caused by the NP aggregation on polyelectrolyte chains. This problem can be minimized by introducing into the system a second inorganic component, such as natural alumosilicate montmorillonite. This layered clay material in aqueous dispersions can be exfoliated into separate sheets with an approximate diameter of 100-200 nm and a thickness of $1.0 - 2.0$ nm [9-15]. These sheets, when introduced into LBL assembly process, can cover large areas of the surface and "heal" some of the defects of the underlying surface. In combination with layers of magnetic NP, the introduction of the interlayers of montmorillonite can vary the strength of magnetic interactions between magnetic layers as a nonmagnetic spacer and insulator.

According to the basic LBL growth mechanism, each adsorption step results in the formation of a continuous monolayer of material. The continuous repetition of deposition cycles yields a film with thickness proportional to number of deposited layers. However, when non-modified or "naked" YIG nanoparticles were assembled, a different

31

growth mechanism was observed. The buildup of YIG films can proceed as the enlargement of isolated 2D particle domains expand laterally and vertically. The surface modification of YIG particles enables the normal LBL growth mechanism to occur.

Experimental Procedures

Materials

PDDA (Mw = 200,000 – 350,000; 20 % wt. in water), PAA (Mw = 450,000), and PSS (Mw = 70,000), used as organic components of LBL assembly, as well as ammonium hydroxide (NH_4OH) and tetramethylammonium hydroxide ($(CH_3)_4N^+OH^-$) were bought from Aldrich (Milwaukee, WI). Crystallic ferrous sulfate ($FeSO_4 \cdot 7H_2O$) was purchased from Fisher (Fair Lawn, NJ). Ferric chloride ($FeCl_3$) and sulfuric acid (H_2SO_4) were obtained from EM Science (Gibbstown, NJ). Hydrochloric acid (HCl) was obtained from VWR Scientific Products (West Chester, PA). Powdered yttrium iron garnet (YIG) was purchased from the Nanomaterials Research Corporation (Logmont, CO). The surface of YIG nanoparticles was modified with (3-aminopropyl)trimethoxysilane ($H_2N(CH_2)_3Si(OCH_3)_3$), which was bought from Fluka Chemie, AG. (Buchs, Germany). Sodium montmorillonite (alumosilicate clay material – clay, C), utilized in the LBL assembly process, was received from the Source Clay Minerals Repository, at the University of Missouri-Columbia, Columbia, MO. Poly(ethyleneterephthalate) (PET) film was obtained from Dupont. LR-white embedding resin, used for TEM sample embedding, was obtained from London Resin Company *Ltd.* (Berkshire, England). All chemicals were used without further purification. De-ionized water (> 18.0 MΩ-cm,

Barnstead, E-pure system), with an unadjusted pH of approximately 5.5, was used exclusively in all solutions and rinsing procedures.

Synthesis of magnetite nanoparticles

Magnetite (Fe_3O_4) nanoparticles were prepared according to the procedure, described elsewhere [16]. Briefly, an aqueous mixture of ferric sulfate (40 mL, 1 M) and ferrous chloride (10 mL, 2 M, in 2 M HCl) was added to an ammonia solution (500 mL, 0.7 M) under rapid stirring. The mixture was aged for 30 minutes. After magnetic decantation over magnetic stirrer, a gelatinous precipitate was obtained and isolated from the solution without washing with water. The precipitate was redispersed in 100 mL of deionized (DI) water and peptized with aqueous 1 M tetramethylammonium hydroxide under rapid stirring. To finish the process, water was added to make a total solution volume of 500 mL. The magnetic ferrofluid obtained was stable in alkaline medium (pH > 9). The particles produced ranged in size between 8-10 nm in diameter with a size distribution of approximately 15% and a cubic lattice structure, as determined by transmission electron microscopy [17] (Figure 5).

Layer-by-layer assembly of magnetite nanoparticles

Rigid silicon wafers and glass slides, as well as flexible 25 μm thick PET film have been used as substrates for layer-by-layer assembly of magnetic nanoparticles. Silicon and glass surfaces were cleaned with a solution of hot Nochromix followed by thorough rinsing with DI water. To improve the uniformity of the coating, the surface of the PET film was partially hydrolyzed by treatment with 0.1 M NaOH according to the
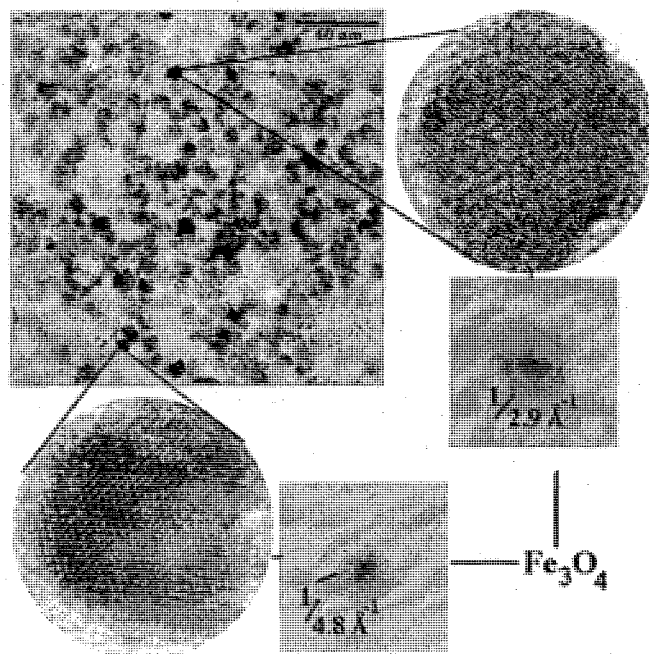
Figure 5. Transmission electron micrographs of uncoated Fe_3O_4 nanoparticles. The lattice planes observed on the TEM images correspond to cubic magnetite, i.e., 4.8 Å for (111) and 2.9 Å for (220) planes, respectively. (Adopted from ref. [17])

procedure described in [18]. This provided additional charges and roughness to the PET surface enhancing adsorption. After washing with DI water and drying, PET pieces were left in 0.5% of PDDA overnight, followed by rinsing with DI water and depositing of magnetite nanoparticles. The deposition cycle for magnetite nanoparticles consisted of the following steps: (1) adsorption of PDDA from a 0.5% solution for 2 minutes, (2) three one minute rinses with DI water, (3) adsorption of nanoparticles for 6 min, and, finally, (4) two one minute rinses with DI water. The time period for adsorption of the nanoparticles was chosen on the basis of previous observations of the formation of monolayers of Fe_3O_4 reported elsewhere [17]. The rate of adsorption varies depending on the material to be deposited. For efficient LBL assembly, the exposure times corresponding to adsorption saturation are suggested. The repetition of this cycle for N times results in the deposition of N PDDA/NP bilayers. LBL multilayers composed solely of magnetite nanoparticles and polyelectrolyte are denoted as $[PDDA/M]_N$, where N is the number of repeating units.

The composite layers combining both clay and magnetite were assembled following several different patterns with one or more PDDA/clay (C), layers inserted between the layers of magnetite nanoparticles. The adsorption time for clay layers was 10 minutes. As with M stacks, they are denoted as $[PDDA/C/PDDA/M]_N$, $[(PDDA/C)_2PDDA/M]_N$, etc.

The assembly of Fe_3O_4 nanoparticles was found to be highly sensitive to pH of the solution, containing the magnetite dispersion. Unlike montmorillonite, the window for a successful LBL procedure is narrow: at pH < 9 the dispersion irreversibly coagulates, while a pH greater than 11.5 results in a very low particle density due to their

35

high surface charge [17,19] and a darkening of PDDA. The assembly of magnetite was carried out with freshly prepared solutions after adjusting the pH to 11.2 using a 0.03 M solution of HCl.

Preparation of the yttrium iron garnet colloid solution

According to the specifications of Nanomaterials Research Corporation, the average diameter of purchased YIG particles was 50 nm. Approximately 0.5 grams of the nanopowder was suspended in 250 mL of DI water with the pH adjusted to 11.23 using NH_4OH. The dispersion was ultrasonically agitated in a Whatman Sonicor SC-50T ultrasound bath for not less than 2 hours. After sedimentation of the heaviest particles by centrifugation at 3800 rpm for 10 minutes, the supernatant containing dispersed YIG particles was decanted and stored for subsequent use in the LBL deposition. The average size of suspended YIG particles was 30 nm in diameter as determined by Transmission Electron Microscopy (TEM).

Modification of YIG colloid

The surface of YIG nanoparticles has been modified according the following procedure. About 2 grams of YIG powder was thoroughly dried in a vacuum decicator for 24 hours to remove any traces of water. Then, the sample was transferred into a 50 mL solution of 0.5% (3-aminopropyl)trimethoxysilane in hexane and the mixture was stirred in an airtight flask for 24 hours. After modification, the solution was decanted and the solid precipitate was washed with a large amount of dry hexane, followed by acetone, and finally ethanol. The modified NP were dispersed in water at an acidic pH < 4 in an

analogous way to the non-modified or "naked" NP, as described previously. Dispersions of equal optical density, which corresponds to close concentrations of nanoparticles, were used in the layer-by-layer assembly procedure in each case.

Layer-by-layer assembly of YIG nanoparticles

The glass slides and silicon wafers used as film substrates were cleaned according procedure, described earlier in this Chapter. An appropriate substrate was immersed in a 1% aqueous solution of high molecular weight PDDA for 10 minutes at pH 3.5 and rinsed 3 times with DI water for 1 minute each. After rinsing the slide was immersed into a beaker containing the YIG suspension for 1 hour. Upon completion of the nanoparticle adsorption, the substrate was removed, rinsed twice with of fresh DI water for 1 minute, and then dried with stream of compressed air. To form multilayers, the entire cycle of PDDA and YIG adsorption was repeated as many times as necessary to obtain a film of the desired thickness. The LBL assembly of YIG nanoparticles was also performed after the deposition of several PE/PE LBL layers as precursor layers. The first layer of PDDA was prepared as described above at pH 3.5. Next, a layer of PAA or PSS was deposited by immersion of the substrate in a 1% aqueous solution of the polyelectrolyte at pH 3.5 for 10 minutes. The substrates were then rinsed three times for 1 minute in three separate beakers. To achieve a better adsorption rate on the precursor layers, five (PDDA/PAA) bilayers topped with a layer of PDDA were made. After that, the substrate was exposed to the YIG dispersion and YIG/PDDA alternations continued as previously described.

UV-visible spectroscopy

The progress of the nanoparticle assembly onto the glass substrates was monitored by UV-visible spectroscopy of the growing film using a HP8453A Hewlett-Packard spectrophotometer. The UV-vis readings were taken after each (PDDA/M) bilayer was added. The dependence of the adsorption increment on the number of layers was observed at 350 nm. The 450 nm wavelength was used to check this dependence when adsorption density of growing film was too high for measuring with spectrophotometer.

Atomic force microscopy

Atomic Force Microscopy (AFM) images were taken using a Nanoscope IIIa Multimode instrument operating in the tapping regime with TESP tips. The surface was scanned at 2 Hz with 256 lines per image resolution and a 1.2-4.0 V setpoint. No filter technique was applied to the images presented. AFM specimens on PET were attached to steel stubs with a layer of adhesive and positioned on the scanning stage of AFM, as it is customarily done for rigid substrates. Virtually, no effect on scanning parameters and performance of the instrument was observed with imaging films on PET as compared to the traditional AFM supports.

Magnetic measurements

Magnetic measurements were performed by using a QUANTUM Design PPMS 6000 magnetometer. The magnetic field H was created by a superconducting solenoid in the persistent mode parallel to the film's surface. For the magnetic hysteresis loops, the

correct demagnetization values corresponding to the sample signals were obtained by subtracting the diamagnetic signal of the substrate from the total registered signal. The linear magnetic response of PET substrates was intrapolated to the -10 kOe $< H <$ 10 kOe region from the high field wings of magnetization curves. The total magnetization signal from each specimen was scaled to the mass of the sample and UV absorption intensity at 350 nm. The saturation magnetization (Ms) of different batches of magnetite dispersions was observed to vary within a 20% interval, which was attributed to the different structure of the magnetite/solution interface affecting the average magnetic moment of nanoparticles. Multilayer systems were made from an identical magnetite dispersion within a period of a few days. Low field magnetization data have been scaled to Ms. Coercivities (Hc), and were calculated as half-widths of corresponding magnetization loops at $M = 0$.

Transmission and Scanning Electron Microscopy

TEM images were taken on a JEOL-2000 FX instrument operating at 100 kV. Samples for TEM were prepared in a way that a layer of magnetic nanoparticles was deposited only on one side of the carbon-coated TEM grid. A 200 mesh copper grid was carefully brought into contact with the surface of aqueous solutions and was allowed to float at the air-water interface for the period of time equivalent to the duration of adsorption in a regular deposition cycle. Then, the grid was carefully removed from the solution, avoiding the contact of its backside with the subphase, and was transferred onto the surface of the next solution.

Scanning electron microscopy (SEM) images were taken on a JEOL JXM 6400 scanning electron microscope with an Oxford X-ray system and cryostage operating at an accelerating voltage of 15-20 kV and a field depth of 8. The samples were coated with gold in a Denton Vacuum Desk II magnetron sputterer/etcher.

Ellipsometry

Ellipsometric measurements were made with an AutoEL MS ellipsometer from Rudolph Research Corporation. The measurements were performed with use of a 632.8 nm line of He/Ne laser incident upon the sample at 70°. The DafIBM program supplied by Rudolph Technologies was employed to determine the thickness values of the films.

ξ-potential measurements

The ξ-potential measurements were performed by using Malvern Zetasizer 2000 HS operating with an internal 10 mW, 633 nm He-Ne laser in the right angle geometry. The standard 1x1 cm cuvette was used in these measurements. ξ-potentials of PDDA, PAA, and PSS layers were determined by adsorbing the polyelectrolytes onto 200 nm latex particles [20]. The latex dispersion was added to the corresponding polyelectrolyte with a pH adjusted to the required value and allowed to sit for 30 min. After gentle centrifugation and rinsing with water, the particles were redispersed in water with appropriate pH and the ξ-potential of latex particles was measured in the regular fashion.

Results and Discussion

LBL deposition of magnetite nanoparticles

The LBL assembly of PDDA/Fe$_3$O$_4$ multilayers can be performed on variety of substrates. Upon deposition on glass and other transparent substrates, the growth of the film can be monitored by an increase of UV-vis optical density (O.D.) (Figure 6), which in the region > 320 nm originates primarily from the absorption and scattering of light by magnetic particles and their aggregates. It is clearly seen that the assembly rate slowly increases and reaches a maximum after depositing approximately 10-12 PDDA/Fe$_3$O$_4$ bilayers. This can be attributed to the fact that deposition of the initial layer of PE to the surface of the glass slide was not complete. Each additionally adsorbed layer of PDDA increased the area of substrate surface covered with growing film. Once complete coverage of surface is achieved, the increment of optical density remains virtually constant on each deposition cycle, which indicates that the same amount of material is being deposited. The dependence of O.D. on the number of deposited layers was found to be virtually linear for 50 deposition cycles and likely would remain constant. To eliminate the initial period of slow growth, the surface of the substrate can be pretreated with an aim of adding additional hydrophilicity and surface charges. The pretreatment procedure depends on the type of substrate used. For example, the surface of PET film can be partially hydrolyzed with NaOH solution, while the surface of the silicon wafer requires deposition of precursor polymer/polymer bilayers as pretreatment.

41
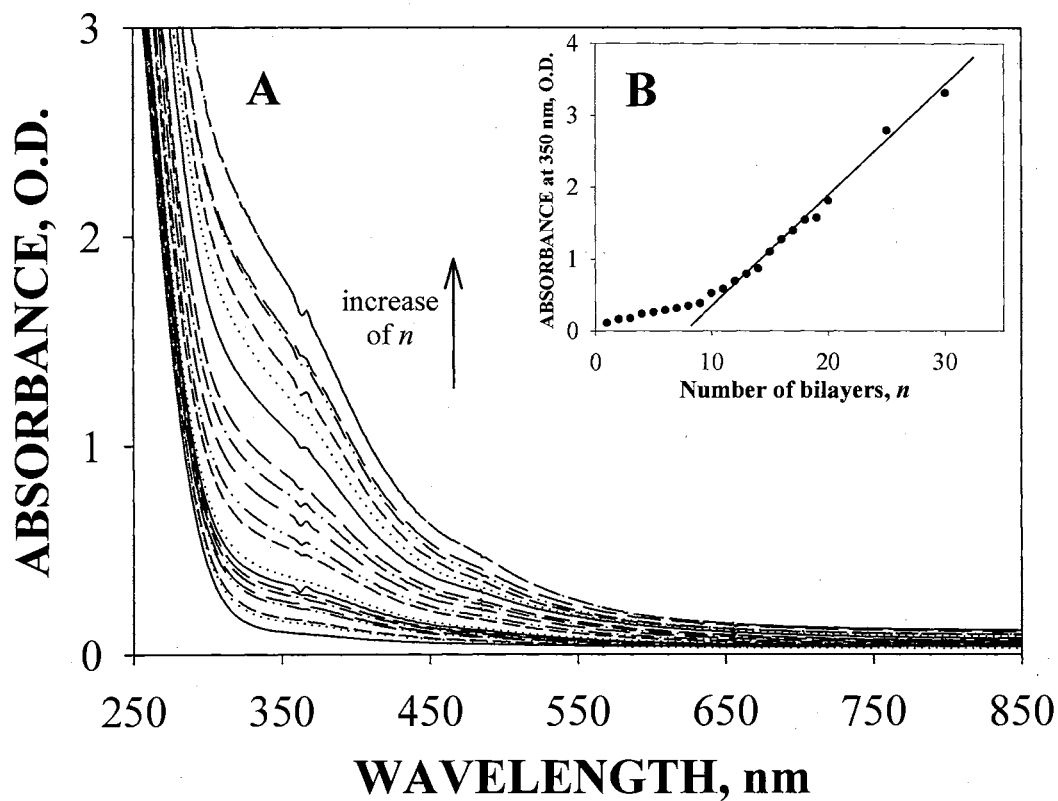
Figure 6. (A) UV-vis absorption spectra of [PDDA/M]$_N$ multilayers with glass as a substrate. (B) Dependence of the optical density of [PDDA/M]$_N$ ($N = 1 - 30$) multilayers at 350 nm.

Optical characterization of magnetite films on PET

Multilayers of magnetite can be assembled on a variety of substrates. The necessity in varying the substrate for preparing films arises from the requirements of different analytical techniques. In addition to glass slides, films have been deposited on silicon wafers and mica sheets for AFM study, carbon coated copper grids for TEM imaging, and thin PET films for magnetic measurements.

A PET film is the least conventional substrate for the assembly of nanoparticles due to its flexibility. On the other hand, its utilization is essential for magnetic measurements since PET is also employed as a base for magnetic recording tapes with a memory layer made from metal oxide particles [21]. The monitoring of the multilayer buildup on a PET support by UV-visible spectroscopy reveals qualitatively similar spectra to ones formed on a glass substrate (Figure 7). As with glass, the linear dependence of optical density on the number of the layers at fixed (350 nm) wavelength was observed (Figure 7 B). The difference in curve slopes for PET (above) and glass (below) reflects the difference in quality of the underlying substrate. Atomic force microscopy study of PET films before and after hydrolysis (Figure 8) shows, that the latter substrates had greater roughness. This provides higher adsorption area for PDDA and for inorganic components subsequently, which yields a greater optical density increment.

The UV-vis absorption spectra for magnetite films assembled on PET revealed unusual oscillations in the near IR-part (Figure 7 A), which have not been seen for LBL assemblies on glass slides (Figure 6 A). The origin of these oscillations stems from the
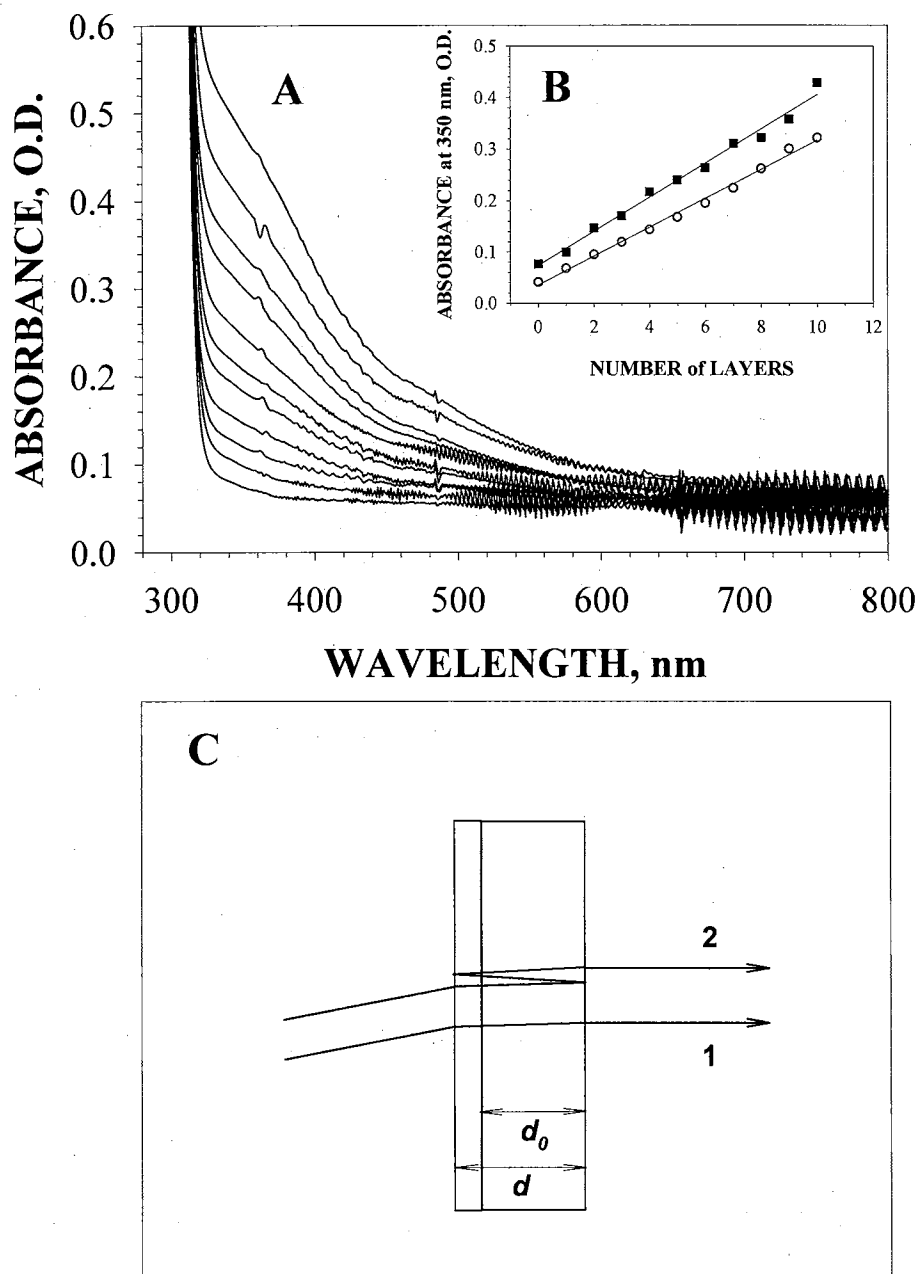
Figure 7. (A) Absorption spectra of [PDDA/M]$_N$ multilayers with N = 1, 2, 3, ... 10 (from bottom to top) with hydrophilic PET as a substrate. (B) The dependence of optical density at 350 nm for magnetite nanoparticle multilayers of different architecture: [PDDA/M]$_{10}$ on glass (o), [PDDA/M]$_{10}$ on PET (■), (C) Optical scheme for the formation of diffraction ripples in absorption spectra in (A). The angle of incidence is altered for clarity.
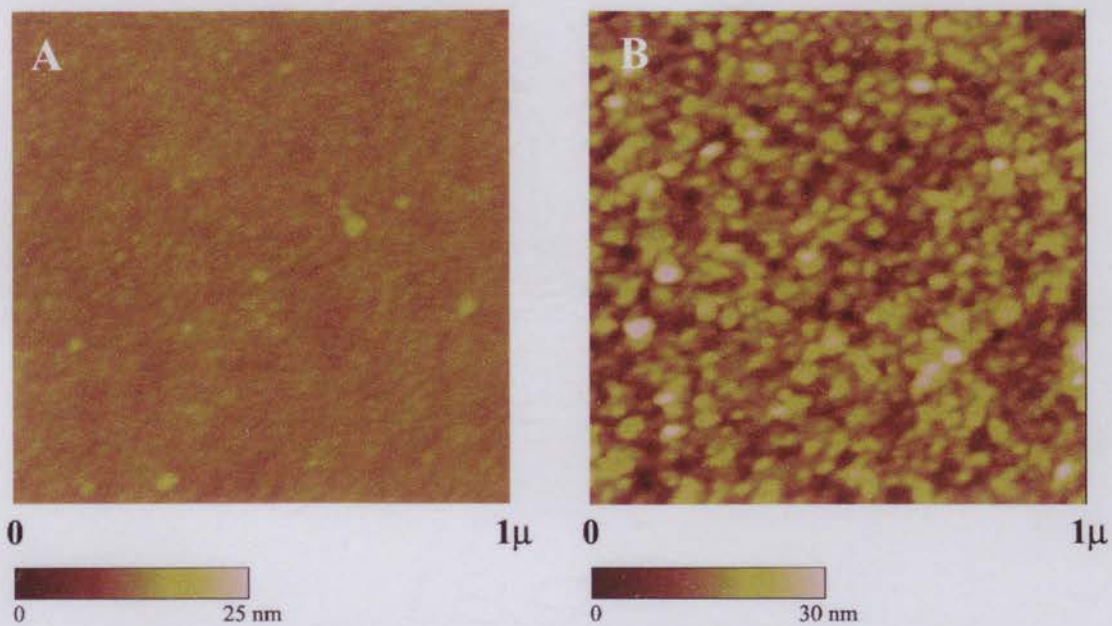
Figure 8. AFM images of PET film (A) before and (B) after surface hydrolysis. PET with the surface topography similar to the one in image B was used as a substrate for the preparation of multilayers of nanoparticles.

interference of transmitted beams 1 and 2 (Figure 7 C) with the path and phase difference caused by the reflection from both surfaces on the thin substrate.

An expression for the period of these oscillations can be written in terms of wave optics. The conditions for the constructive interference of beams 1 and 2 in Figure 7 are shown in equation 1:

$$m\lambda = 2dn \qquad (1)$$

where m is an integer, λ is the average wavelength of the period in the UV-vis spectrum, d is the total thickness of the film, and n is the refractive index of the substrate. The period of oscillations is calculated by finding the difference between two neighboring maxima of constructive interference corresponding to m and $m - 1$ (equations 2 and 3):

$$m_1\lambda_1 = 2dn \qquad (2)$$

$$(m_1 - 1)\lambda_2 = 2dn \qquad (3)$$

Therefore, the period of oscillations, p can be expressed as

$$p = \lambda_2 - \lambda_1 = 2dn/(m_1 - 1) - 2dn/m_1 = 2dn/(m_1 - 1)m_1 \approx 2dn/m_1^2$$

$$m_1 >> 1 \qquad (4)$$

In this equation, the total number m_1 of wavelengths λ_1 fitting the path difference between the two diffracting beams is equal to

$$m_1 = 2dn/\lambda_1 \qquad (5)$$

Since λ_1 and λ_2 are close to each other, the average between λ_1 and λ_2, can be substituted for λ. Then the substitution of equation 5 into equation 4 yields equation 6:

$$p = \lambda^2/2dn \qquad (6)$$

which describes the observed oscillations in the UV-vis spectrum.

The effect of the layer thickness on the position of the oscillation maximum can be described in the same way. When equation 1 is applied to two films with thicknesses of d_1 and d_2, respectively, the difference in construction interference maxima $\Delta\lambda$ corresponding to the same m can be expressed as

$$\Delta\lambda = 2d_1n/m - 2d_2n/m = 2n(d_1 - d_2)/m \qquad (7)$$

A simple rearrangement of this equation gives

$$\Delta d = (d_1 - d_2) = \Delta\lambda d_0/\lambda \qquad (8)$$

where d_0 is the thickness of the PET skin (25 μm) with no films on it.

An application of equation (6) to the bare PET film (Figure 9 A, curve 1) in the 715 – 749 nm range (taking λ = 732 nm d = 25 000 nm, and n = 1.55 [22]) yields p = 6.91 nm. This theoretical period coincides very well to the experimentally observed p = 6.8 nm (Figure 9 B). For glass slides and other thick substrates, such oscillations are not observed because of substantially larger d, which results in very small period p = 0.2 nm for a 1 mm glass plate), and a much lower intensity of the reflected beam.

With the assumption that the mechanism of interference does not change with the assembly of additional layers of magnetite, it is possible to calculate the thickness of deposited films from the shift of the oscillation pattern. However, when magnetite layers with a expected thickness of 10 nm each were deposited, the observed change in oscillation pattern corresponded to a much greater shift than theoretically calculated (4 nm vs. 0.6 nm for [PDDA/M]$_2$ assembly) (Figure 9 B). This indicates that additional interference of the beams takes place at the interface of the PET and magnetite films due to a high refractive index of the magnetite nanoparticles. The increase in the amplitude of

47
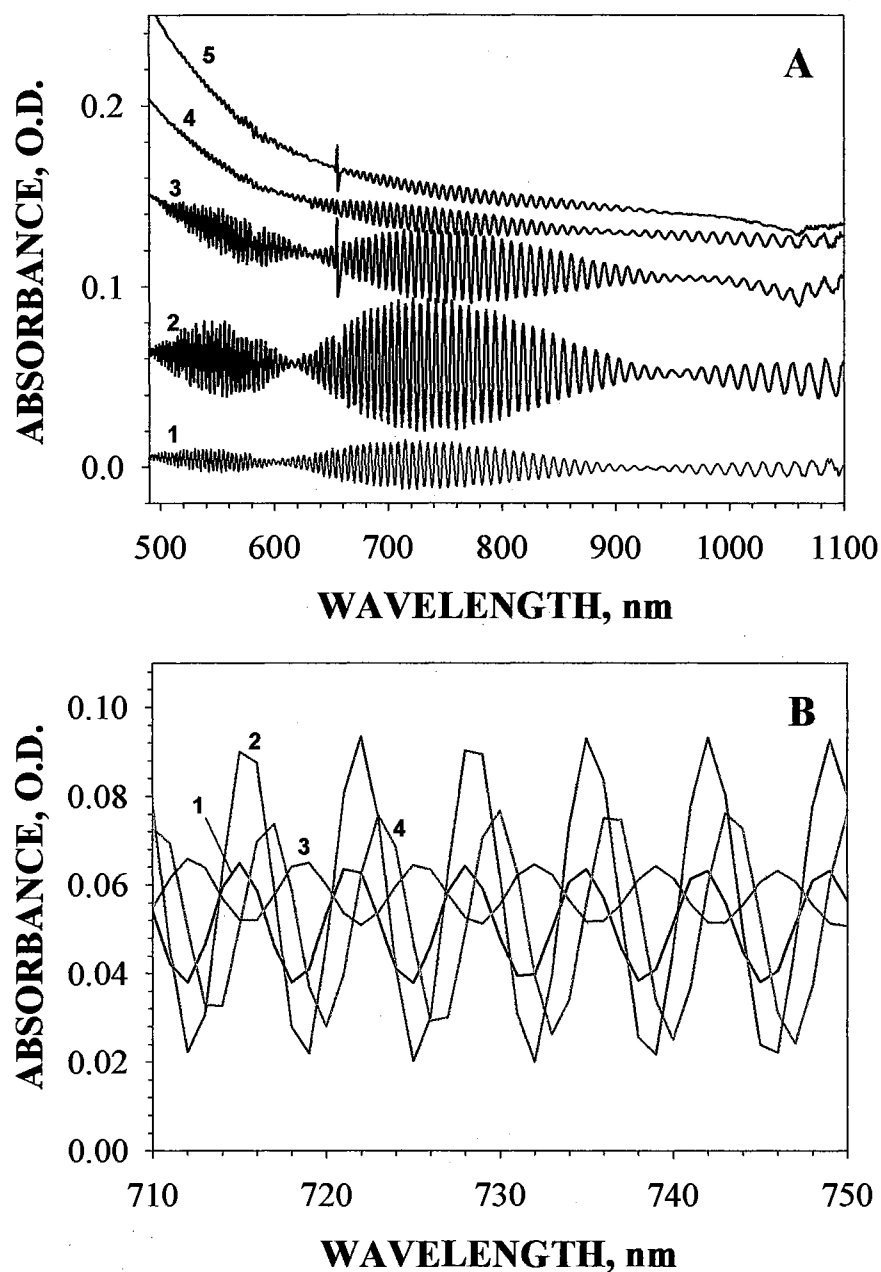
Figure 9. Details of the diffraction ripples. (A) Dependence of the amplitude of oscillations on the thickness of the [PDDA/M]$_N$ magnetite overlayer for N = 0, 1, 3, 7, 10 (plots 1-5 respectively) on the PET substrate. The plots are shifted along the vertical axis for clarity. (B) Details of the diffraction ripples: the horizontal shift of the diffraction wave for a sequence of [PDDA/M]$_N$ films on PET substrate; plots 1, 2, 3, and 4 correspond to N = 0, 1, 2, and 3.

oscillations after absorption of the [PDDA/M]$_1$ layer can also be attributed to interactions at the PET/multilayer interface. The decrease in amplitude after deposition of additional layers of magnetite can be attributed to the adsorption and scattering of the reflected beam by the magnetite coating.

Magnetite/montmorillonite composite layers: LBL assembly

It was previously mentioned that the LBL method allows for the design of structurally complex assemblies. In such complex films, the functional properties of one inorganic material can be complemented by the properties of other inorganic materials. Most importantly, the characteristics of the whole structure can be controlled by the sequence of the layers, which is determined by the dipping procedure.

The magnetite layers in [PDDA/M]$_N$ multilayers can be interlaced with layers of montmorillonite clay (C), which are known to be used in the layer-by-layer assembly process [9-15]. Both montmorillonite and magnetite are negatively charged and, therefore, the preparation of M and C composites can be accomplished by simple adsorption of the corresponding species on a layer of positively charged PDDA. The sequence of M and C layers will be determined by the dipping order in corresponding solutions.

When layers of nanoparticles are interlaced with layers of clay, the absorption-increment plots register the difference in the quality of the substrate (Figure 10). The total number of magnetite clusters deposited in each cycle increases as compared to the simple [PDDA/M]$_N$ sequence. The absorption rate remains virtually constant for [PDDA/C/PDDA/M]$_N$, [(PDDA/C)$_2$PDDA/M]$_N$, and [(PDDA/C)$_3$PDDA/M]$_N$
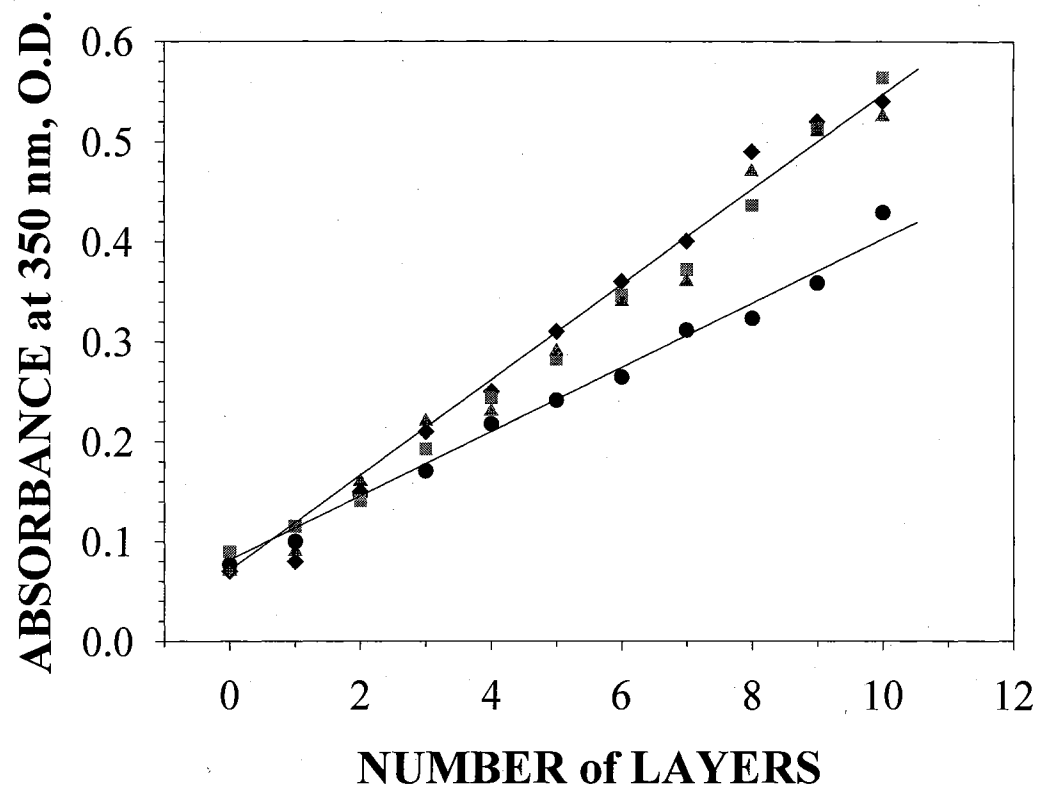
Figure 10. The dependence of optical density at 350 nm for magnetite nanoparticle multilayers of different architecture on PET substrate: [PDDA/M]$_{10}$ (●), [PDDA/C/PDDA/M]$_{10}$ on PET (■), [(PDDA/C)$_2$PDDA/M]$_{10}$ on PET (◆), [(PDDA/C)$_3$PDDA/M]$_{10}$ on PET (▲).

architectures. The increase of the rate with respect to $[PDDA/M]_N$ is attributed to the high negative charge of the montmorillonite surface that promotes adsorption of the positively charged polyelectrolyte. Consequently, thicker PDDA layers retain a greater number of Fe_3O_4 nanoparticles.

The different structure organization for multilayers with variations in deposition sequence can be observed with TEM imaging of magnetite layers. Since the formvar/carbon coating of TEM grids provides a hydrophobic surface for adsorption of the highly charged PDDA molecules, a non-uniform distribution of magnetite nanoparticles, which is seen on TEM micrograph (Figure 11), may not represent the actual particle distribution inside of the films assembled on hydrophilic glass or PET surfaces. The increase in nanoparticle density is clearly visible when a layer of clay is introduced between the TEM grid and magnetite (Figure 11 B). Additionally, the clay underlayer makes the distribution of nanoparticles more uniform. The difference in particle density can be attributed to differences in the density of the polyelectrolyte chains adsorbed in the preceding cycle. Large clay platelets bridging the gaps in the polyelectrolyte layer reduce the inhomogeneity of charge distribution, providing a more uniform surface for the second polyelectrolyte layer. A better packed polyelectrolyte layer results in a more efficient adsorption of nanoparticles, which leads to the formation of multilayers.

For the magnetic measurements of the obtained films, a reduction in the diamagnetic contribution from the solid support was essential because of very small mass of the deposited nanoparticles. For this reason a thin PET film was preferred for these types of measurements over silicon, glass, or other types of "thick" substrates. Due to the
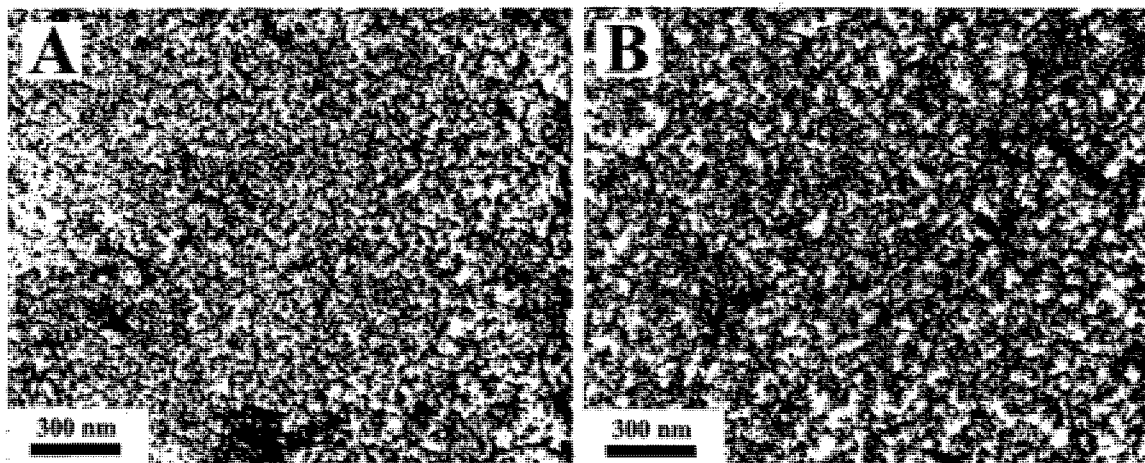
Figure 11. Transmission electron microscopy images of magnetic nanoparticles on a standard TEM copper grid bearing (A) an [PDDA/M]$_1$ film and (B) a [PDDA/C/PDDA/M]$_1$ film. Dark fields represent areas covered by nanoparticles. The average particle density on the TEM grids is expected to be lower than that on silicon wafers or PET because of hydrophobic formvar/graphite foundation coating. Contrast of the images was increased intentionally to visualize nanoparticle areas.

intrinsic roughness of the hydrolyzed PET, the topography features of the nanoparticle and clay layers are masked on the topography scans (Figure 12). All the images closely resemble that of PET in Figure 8 B. However, it can be noted that the fine grain texture characteristic of nanoparticle surfaces is again more pronounced for films with the top magnetite layer (Figure 12 B). A topography independent characterization of the surface can be done by using the phase shift registration mode of the AFM instrument. The phase images are sensitive to the strength of interactions between the tip of AFM probe and the topmost layer in the stack regardless of the relative height of it. The phase scans clearly show the alteration of the surface quality when montmorillonite sheets are deposited on a layer of magnetite nanoparticles (Figure 12, right images). Since the clay platelets formed a continuous closely packed layer, they can, despite the roughness, separate the magnetite layers from each other.

Magnetite/Montmorillonite composite layers: magnetic properties[ii]

Besides the sheet-like morphology, alumosilicate clays have other useful qualities and, for instance, they can be excellent insulators. Mica sheets, which are often used as electrode spacers, are one of the members of the same alumosilicate family. The insulating properties of LBL layers of clay and similar materials can be utilized in many electrical devices such as sensors, light-emitters [14], and on-chip capacitors. Magnetic phenomena in NP in the nanoscale are dependent on the electronic communication between the NP and insulating coating can strongly affect the magnetic behavior of the

---

[ii] This part of work has been done in collaboration with Dr. Farkhad G. Aliev, Departamento de Física de la Materia Condensada Universidad Autonoma de Madrid, Cantonlanco, 28049 Madrid, Spain.
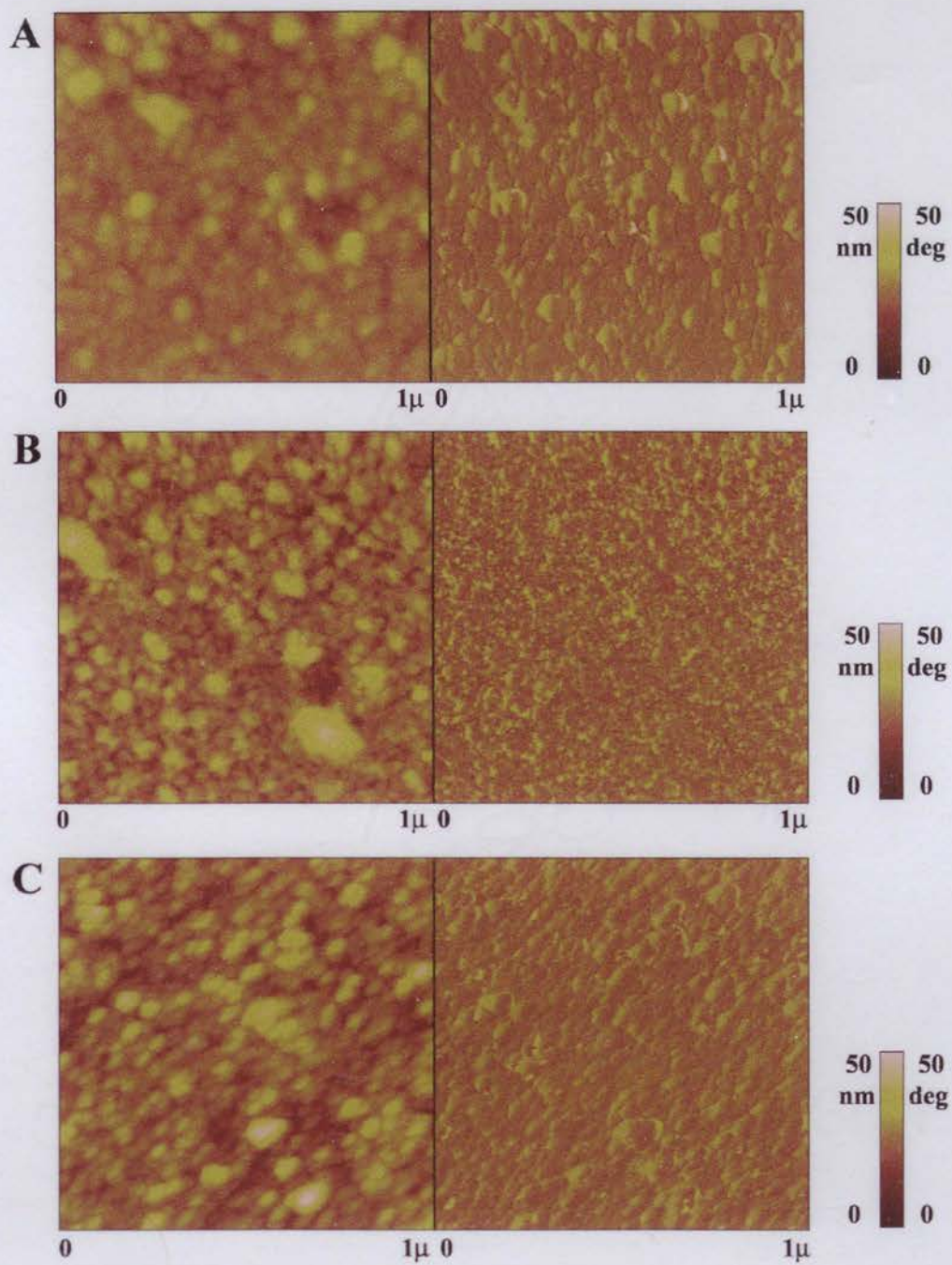
Figure 12. AFM topography (left) and phase (right) images of (A) [PDDA/C]₁, (B) [PDDA/C/PDDA/M]₁, and (C) [PDDA/C/PDDA/M/PDDA/C]₁ films on PET.

NP solids. Therefore, as a part of the investigation of the other effects, it would be interesting to see how magnetic properties of the LBL films respond to the changing the stack architecture, which can provide the information about nature of magnetic interactions of NP.

Magnetization curves of the films with a $[PDDA/M]_{10}$, $[PDDA/C/PDDA/M]_{10}$, and $[(PDDA/C)_2PDDA/M]_{10}$ structure (Figure 13) display typical superparamagnetic behavior. Normalization of the curves to the surface density of the particles and to the mass of the sample makes the saturation magnetization of the specimen independent of the multilayer structure, which levels the high-field plateaus for all of the assemblies.

The effect of the structure of the film on the magnetic behavior becomes visible when magnetic measurements are performed at low-field amplitudes (Figure 14). For $[PDDA/C/PDDA/M]_{10}$, and $[(PDDA/C)_2PDDA/M]_{10}$ structures, all points on magnetization loops fall on one another within a 5% deviation at temperatures of 10, 100 and 300 °C. However, the magnetization properties of the $[PDDA/M]_{10}$ stack differs from those of other stacks used in this study at 10 and 100 K. At liquid helium temperatures, the thermally-activated magnetization flipping characteristic for the superparamagnetic nanoparticles becomes strained. The magnetization curves acquire the shape of a loop (Figure 14 A) with a distinct separation in the two sweeping directions typically observed for ferromagnets. The $[PDDA/M]_{10}$ assembly displayed a slightly lower hysteresis with $H_c = 140$ G, whereas the clay-containing multilayers displayed $H_c = 190$ G. For $T = 100$ °K, (Figure 14 B) superparamagnetism dominates the magnetic properties of the nanoparticles, nevertheless, the S-shaped magnetization curve for $[M]_{10}$ is different as
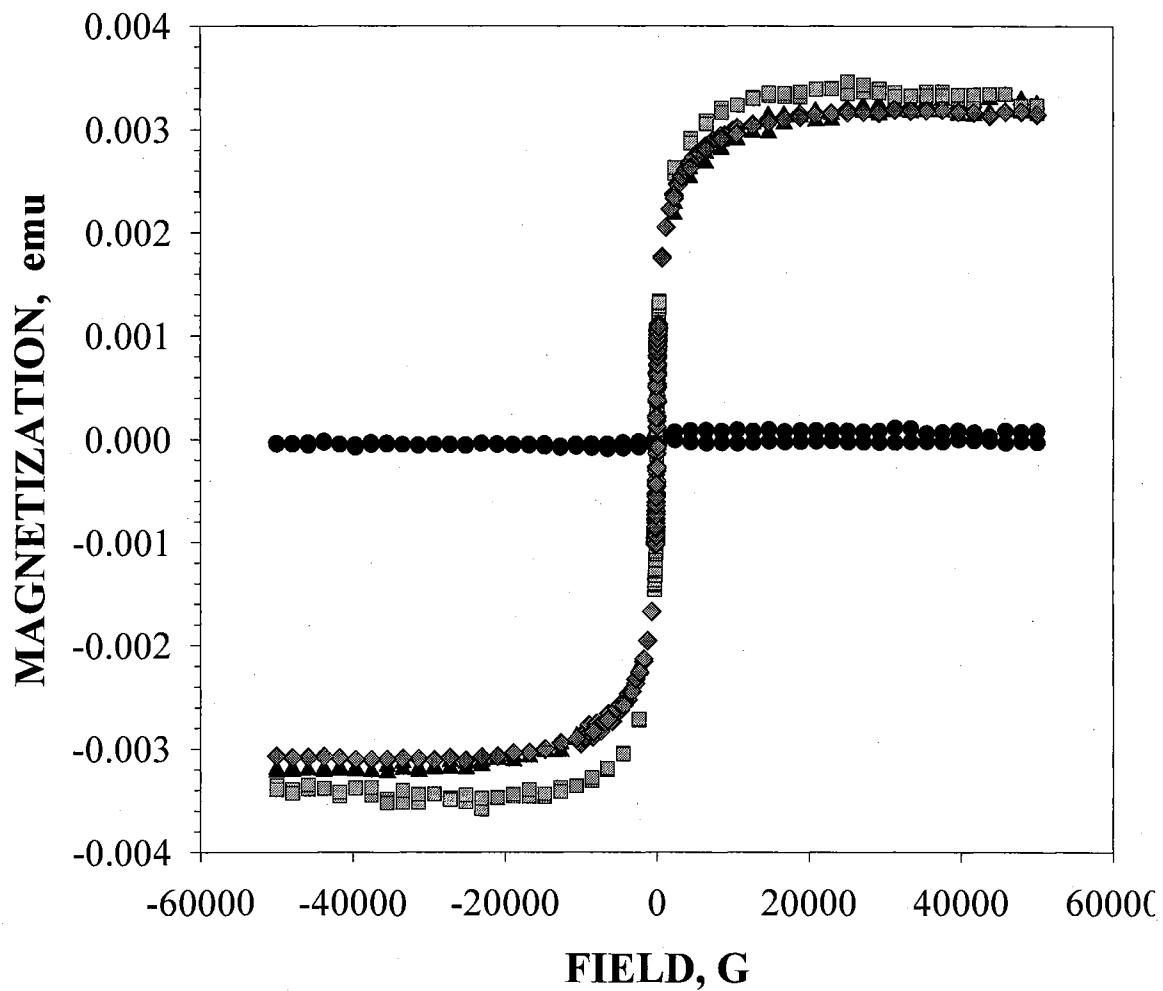
Figure 13. Normalized magnetization loops at T = 300 K for nanoparticulate films of different architecture: [PDDA/C]$_{10}$ (●), [PDDA/M]$_{10}$ (▲), [PDDA/C/PDDA/M]$_{10}$ (■), and [(PDDA/C)$_2$PDDA/M]$_{10}$ (♦).
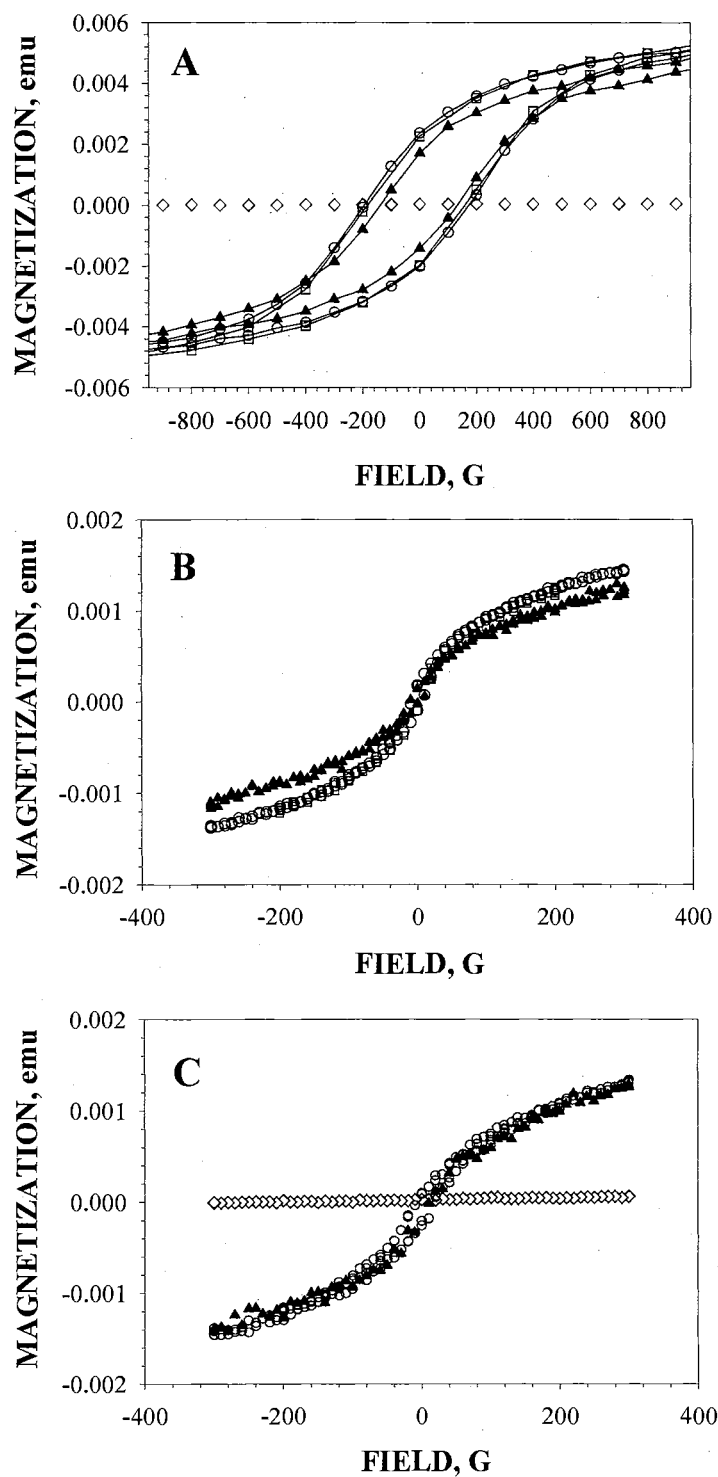
Figure 14. Low-field magnetization loops taken at (A) 10 K, (B) 100 K, and (C) 300 K for nanoparticle films of different architecture: [PDDA/C]$_{10}$ (◊), [PDDA/M]$_{10}$ (▲), [PDDA/C/PDDA/M]$_{10}$ (□), and [(PDDA/C)$_2$PDDA/M]$_{10}$ (○).

compared to the coinciding ones for $[CM]_{10}$ and $[CCM]_{10}$. At $T = 300$ °C (Figure 14 C), the magnetization of $[M]_{10}$ is always the same as for the two other assemblies.

Such a difference in the magnetic behavior can be explained by considering the effect of the magnetite and clay layer sequence on the magnetization switching. The reversal of the magnetization direction occurs mostly as the concerted spin flipping of adjacent magnetic domains, as represented by the Stoner-Wolfarth model [23,24]. According to this model the magnetization reversal can be pictured as the concerted spin flipping of adjacent magnetic domains coupled to each other by exchange and dipole-dipole interactions. Typically, the range of exchange interactions is 2 nm [25,26] and does not exceed 4 nm in the exceptional cases [27,28], while the magnetostatic interaction of magnetic dipoles can span the range of a few tens of nanometers [29]. Therefore, they can be successfully interrupted by isolation with clay layers whose thickness is 2.5-3.0 nm [30]. Since there is little difference in the magnetization curves observed between multilayers of different architecture, the coupling between layers should be mostly attributed to the dipole-dipole interactions with significantly longer characteristic distance.

Preparation of YIG colloid

LBL deposition requires aqueous dispersions of the assembling materials. Therefore, the initial start of the deposition process of YIG particles is the preparation of a stable aqueous colloid of them. To achieve this, the attractive forces between the particles through the high surface potential must be overcome. This is accomplished by varying the pH of the dispersion. The isoelectric point for YIG is located at pH 6-7

58

[31,32]. That means, both basic and acidic media should result in charging of the YIG surface. For "naked" i.e. non-modified particles, the most stable dispersions were obtained at pH 11.2, where YIG particles are negatively charged (ξ-potential is equal -17 mV). Such solutions were stable for months without any sign of precipitation. In comparison with silica or titania particles of similar size, which form stable dispersions in mild basic or acidic solutions, the pH of the YIG dispersions was somewhat higher. This fact can be attributed to additional, relatively weak magnetic forces between YIG particles. TEM study revealed that the dispersions obtained are fairly polydispersed with particles ranging in size from 15 to 50 nm in diameter (Figure 15). The average diameter of the particles was 32 nm.

Layer-by-Layer assembly of "naked" YIG

As in the case of magnetite nanoparticles, the layer-by-layer deposition of YIG NP on glass substrates was monitored by the increase in the UV-vis absorbance (Figure 16 A). A stable linear growth of the LBL assembly was obtained when the deposition time of YIG nanoparticles was increased from a few minutes to 1 hour (Figure 16 B). Elongation of the exposure time for YIG to 12 hours did not significantly affect dependence of O.D. on number of deposited layers.

Ellipsometric measurements of the thickness of the growing film showed that the average film thickness increases linearly with an increasing number of adsorbed layers (Figure 16 C). The average thickness increment, added by a single PDDA/YIG bilayer, is
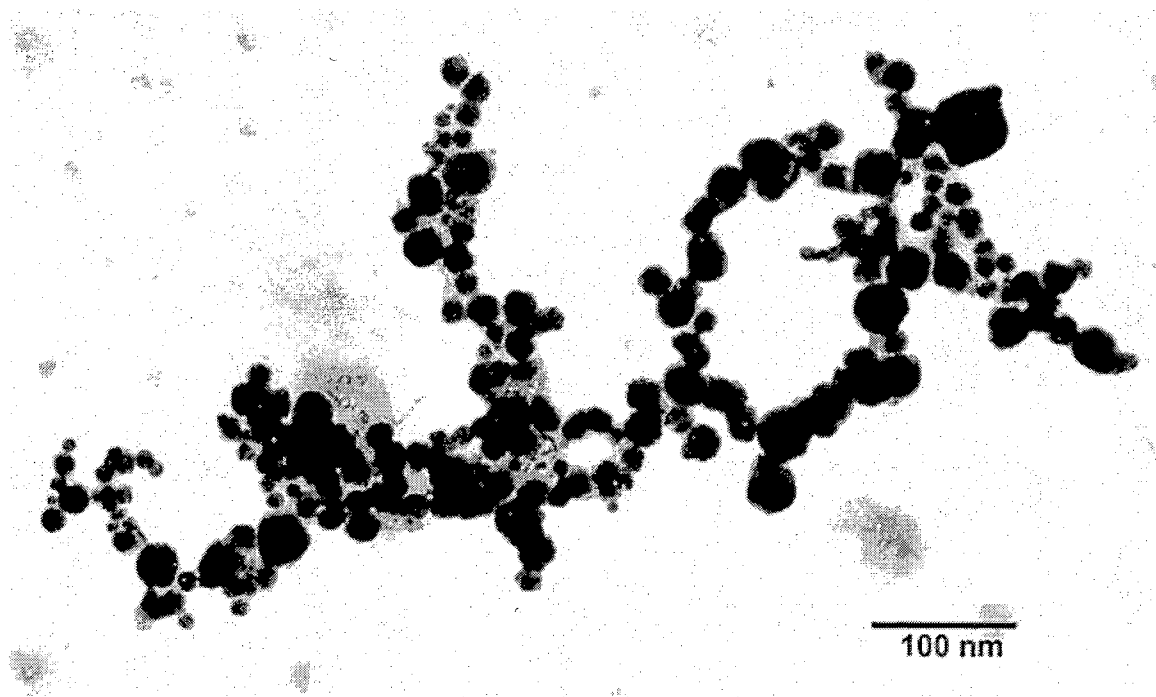
Figure 15. Transmission electron microscopy image of YIG nanoparticles in aqueous dispersion used for LBL assembly.
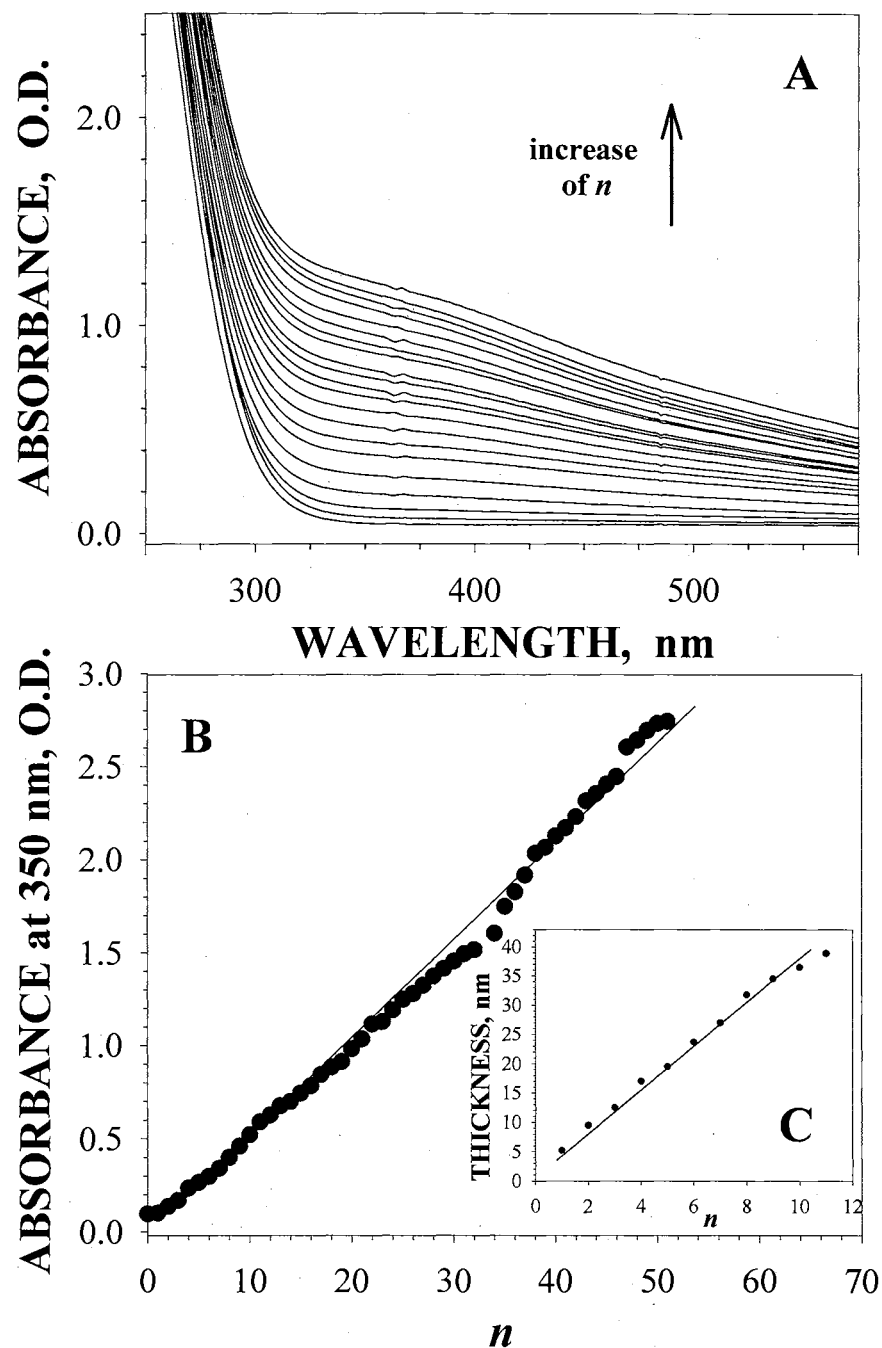
Figure 16. (A) UV-vis absorption spectra of $(PDDA/YIG)_N$, $N = 1\text{-}20$, films sequentially adsorbed on a glass slide. (B) Dependence of the optical density of $(PDDA/YIG)_N$, $N = 1\text{-}50$, films at 350 nm assembled with 1 hour of the YIG adsorption step. (C) Ellipsometric thickness of $(PDDA/YIG)_N$, $N = 1\text{-}11$, sequentially deposited on a glass slide and registered at 632.8 nm.

3.5 nm. Since the average nanoparticle diameter is 32 nm, it is assumed that this corresponds to an average surface density of one YIG nanoparticle per 30 000 nm^2. In view of the requirement of the surface charge switching, which is vital for the successful LBL process, the consistent multilayer growth seen in Figures 16 A and C raises the question about the actual mechanism of the layer-by-layer growth in this case.

The SEM study of the surface topography allowed for resolution of this problem. It is clearly seen from the SEM micrographs (Figure 17) that with an increase in deposition cycles number, the formation and growth of fairly isolated YIG domains was observed. This observation is somewhat contradictory to the classical LBL growth mechanism, where formation of sandwich-like organic/inorganic layers is proposed. The size of the domains increased with adsorption of additional layers of YIG from 0.5 – 1.5 μm in layer 1 to 3-4 μm in layer 3 (Figure 17 A – C). At higher magnification the YIG domains are 3D agglomerates of YIG nanoparticles (Figure 17 D).

The domain expansion growth pattern was initially regarded as the result of poor quality substrate carrying hydrophobic patches. However, for glass slides and silicon wafers, thoroughly cleaned with hot piranha solution for 30 minutes as well as the treatment of the glass slides with a promoter of polyelectrolyte adsorption (3-aminopropylsiloxane), the identical deposition patterns were observed. Furthermore, coating of the glass substrate with a highly hydrophilic precursor film, consisting of (PDDA/PAA)$_5$ assembly, resulted in the same growth pattern (Figure 18).
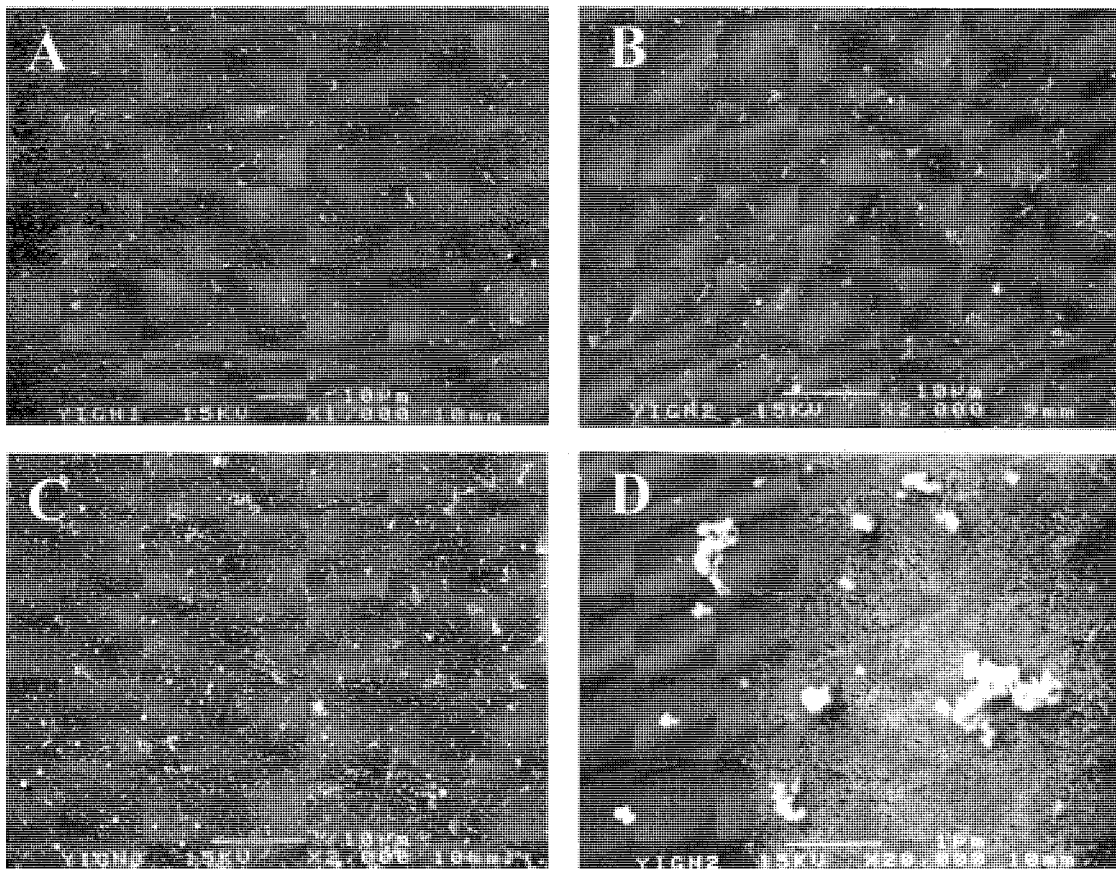
Figure 17. Scanning electron microscopy images of $(PDDA/YIG)_N$ films with (A) $N = 1$, (B and D) 2, and (C) 3.
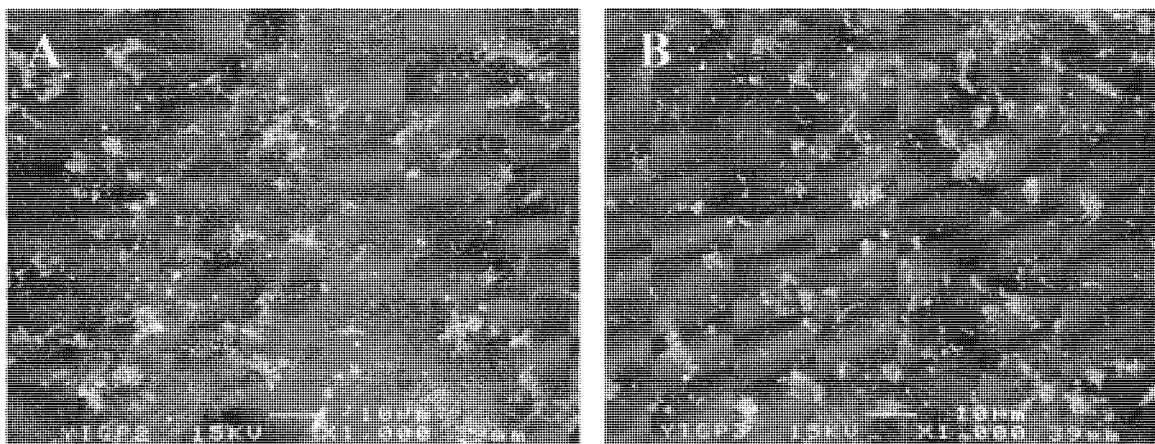
Figure 18. Scanning electron microscopy images of (PDDA/YIG)$_N$ films with (A) $N = 2$, and (B) 3 assembled on precursor layer (PDDA/PAA)$_5$PDDA.

The domain expansion mechanism of growth is not specific to YIG nanoparticles. Similar growth mechanism has been shown for 40 nm barium ferrite nanoparticles and 200 nm polystyrene latex[iii].

Switching the growth modes: modification and
layer-by-layer assembly of YIG

For designing and preparing various thin film materials and devices utilizing the LBL method, it is always better to have conditions that form a complete, densely packed adsorption layer on every deposition step. The domain expansion mode of growth of the film does not give complete control over the structure of the obtained film. Therefore, it is necessary to have some methods to switch the growth mechanism. One of the possible ways to do such a switching is to elevate ionic strength of a solution by adding NaCl to the colloids of adsorbing materials [30,33]. However, even though the addition of NaCl reduces the repulsion between the nanoparticles by shielding their surface charges, it also reduces the attraction between YIG and PDDA. Therefore, the increase in ionic strength results in both positive and negative effects with respect to increasing the surface density of nanoparticles.

Another way to overcome the problem of switching the mode of the growth mechanism is to modify to a surface of "naked" YIG nanoparticles. The surface of unmodified "naked" YIG is very hydrophilic. To retain the stability of the colloid in water and at the same time increase its ability to interact with the polyelectrolyte though hydrogen bonding and hydrophobic interactions, the surface of YIG was modified with a

---

[iii] The LBL assembly of barium ferrite and latex particles has been done in collaboration with John W. Ostrander, Oklahoma State University, Stillwater, OK, USA and reported in Ostrander, J. W.; Mamedov, A. A.; Kotov, N. A. *J.Am.Chem.Soc.* **2001**, *123*(6), 1101-1110.

3-aminopropyl hydrocarbon chain through a siloxane bridge to the surface of the nanoparticles (Figure 19). The hydrocarbon chain resulted in efficient attraction to similar organic groups in the polyelectrolyte, while the surface charge prevented irreversible coagulation of the colloid. This procedure yielded a colloid solution stable in acidic media with a positive surface charge (ξ-potential at pH 3.5 is +12 mV).

Since the surface of the modified YIG nanoparticles is positively charged, the LBL assembly was carried out utilizing negatively-charged polyelectrolytes, such as PSS and PAA. For both polymers, the linear increment of optical density with adsorption of each additional layer was obtained. Furthermore, the δO.D./δN is significantly higher than that for "naked" YIG. In particular, for assembly with 0.5% PAA at pH 3.5 and a deposition time 1 hour, the δO.D./δN increases 5 times in comparison with non-modified YIG (Figure 20). SEM study also reveals improvement in film structure: the nanoparticles are densely packed after only one deposition cycle (Figure 21 A). The size of the aggregates visible in the image is much smaller than that for non-modified YIG and does not exceed 0.5 μm in diameter. As the number of deposition cycles increases, the topography of the film shows little change with the exception of greater density of the particles and their aggregates (Figure 21 B). The AFM image of (PAA/modified YIG) bilayer confirms the SEM data (Figure 22).

The increase in the surface density of the nanoparticles of modified YIG should be attributed to the attractive interactions between hydrocarbon groups of the organic modifier and the polyelectrolyte chains adsorbed to the substrate. Some additional contribution from the formation of hydrogen bonds should be considered. The difference

66
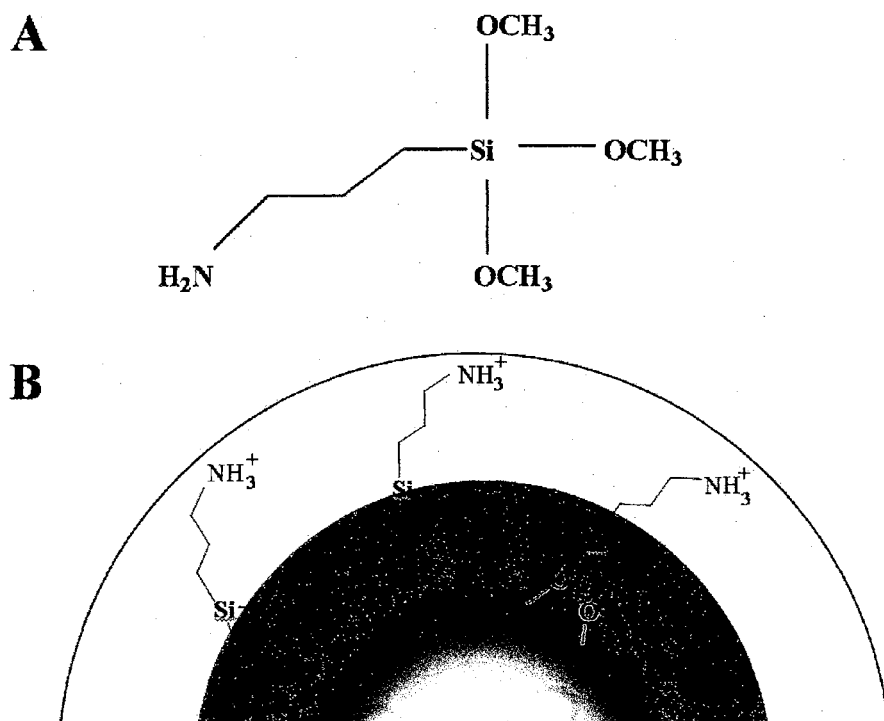
Figure 19. (A) Structural formula of (3-aminopropyl)trimethoxysilane. (B) Formation of the positively charged shell of organic compound on the surface of nanoparticle.
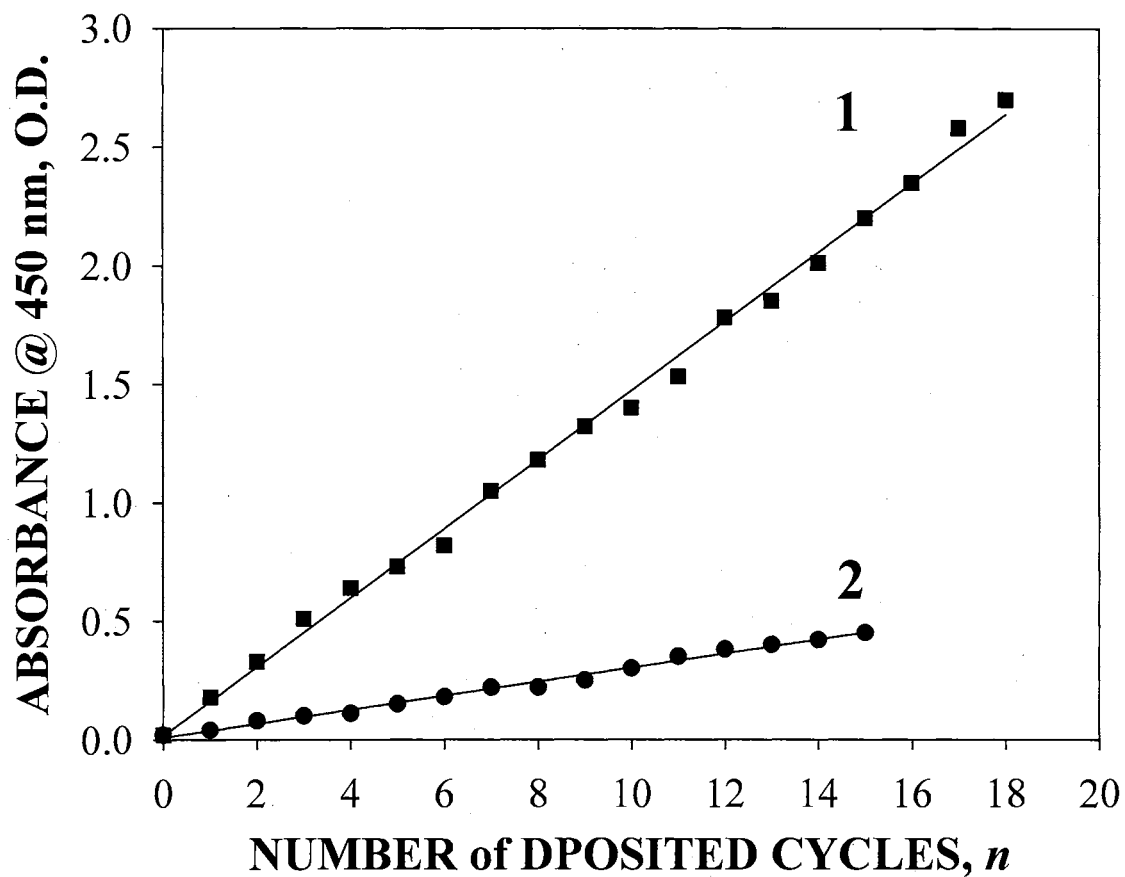
Figure 20. Dependence of optical density at 450 nm for the LBL assembly of the modified YIG (line1) and non-modified YIG (line 2) on the number of deposition cycles. A different wavelength than in Figures 7, 10, and 14 was used to avoid reaching optical densities too high for measuring with a spectrophotometer.

68
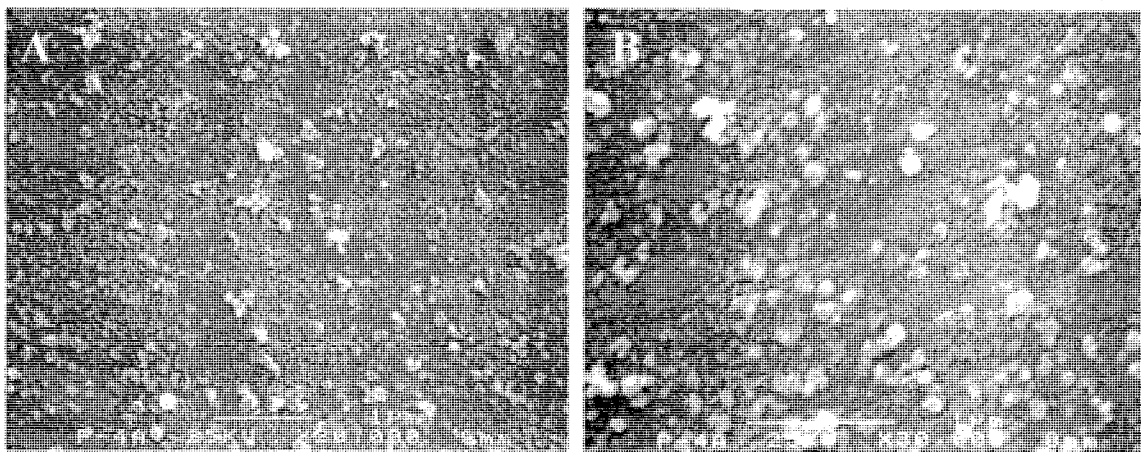
Figure 21. Scanning electron microscopy images of (PSS/modified YIG)*N* films with (A) *N* = 1 and (B) 2 assembled on a PDDA/PAA precursor bilayer.
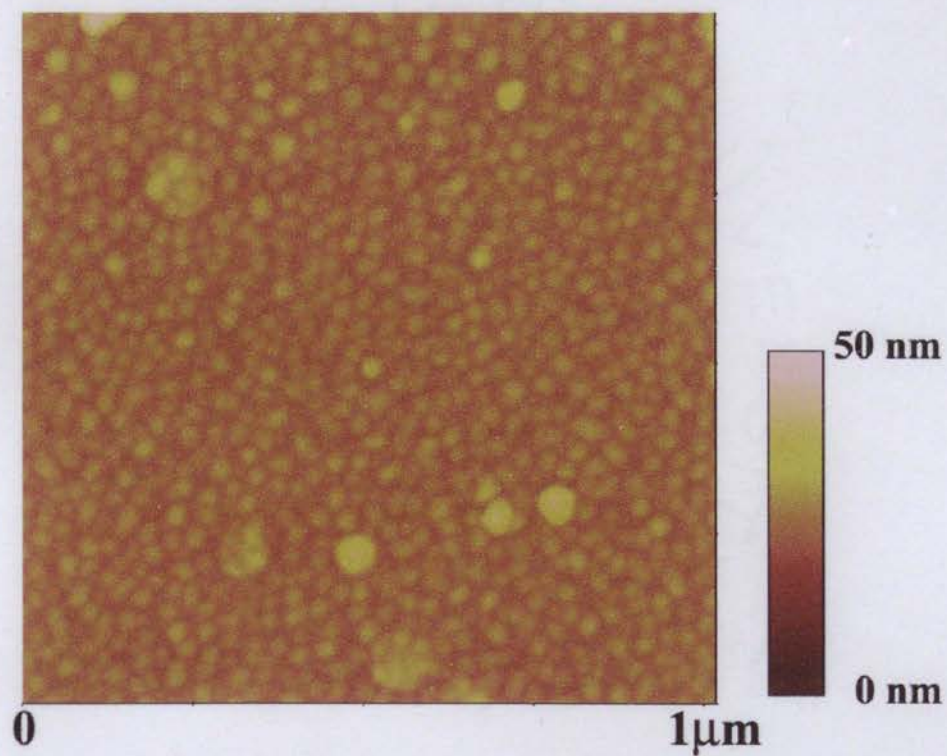
Figure 22. AFM image of (PAA/modified YIG) bilayer, assembled on precursor PDDA/PAA bilayer.

in adsorption behavior of "naked" and modified YIG cannot be attributed to the difference in electrostatic attraction between nanoparticles and matching polyelectrolytes. The ξ-potentials of PSS at pH 3.5 is +15 mV and for PDDA at pH 11 is −12 mV. Considering the fact that at corresponding pH values the ξ-potentials for modified and "naked" YIG are +12 mV and − 17 mV respectively, one can see that the magnitudes of the potentials are virtually the same for both LBL pairs. Therefore, the long-distance Coulomb interaction between the nanoparticles and the polyelectrolyte-coated substrate is nearly the same for both pairs.

Conclusion

Thin films of Fe_3O_4 nanoparticles were produced on a variety of substrates utilizing the LBL assembly technique. A distinctive sandwich-like structure of the film was obtained by introducing layers of montmorillonite clay between the layers of magnetite nanoparticles. The introduction of alumosilicate sheets, which cover large areas of the substrate surface, inhibited interpenetration of the multilayers and facilitates complete separation of the magnetite layers from each other. It has been demonstrated that the magnetic properties of the assemblies are affected by the multilayer architechture. For $[CM]_{10}$ and $[CCM]_{10}$ sequences, the coercivity at 10 K increases as compared to $[M]_{10}$ films due to the interruption of electron exchange coupling between the magnetite layers.

The growth of YIG nanoparticle LBL assemblies takes place through two modes of deposition, which are difficult to distinguish by following the standard optical density vs. number of layers plots. One of the modes allows for the preparation of the multilayer

71

stacks and control of the structure of the obtained films on every deposition step (normal growth mode), while the other one does not (domain expansion mode). Film growth via the domain expansion mode can be switched to the sandwich mode by organic modification of nanoparticles, which supplements the electrostatic interactions between nanoparticles and polymers with hydrophobic interactions.

References

1. Lvov, Y.; Ariga, K.; Kunitake, T. *Chem. Lett.* **1994,** (12), 2323-2326.

2. Decher, G.; Lvov, Y.; Schmitt, J. *Thin.Solid.Films.* **1994,** *244* 772-777.

3. Kotov, N. A.; Dekany, I.; Fendler, J. H. *Adv.Mater.* **1996,** *8*(8), 637-641.

4. Fendler, J. H.; Kotov, N. A.; Dekany, I. *NATO ASI Ser., Ser.3* **1996,** *12*(Fine Particles Science and Technology), 557-577.

5. Kotov, N. A. *Stratification and lateral ordering in layer-by-layer assembled films of nanoparticles*; 2002.

6. Wang, S.; Mamedova, N.; Chen, W.; Kotov, N. A. *Layer-by-layer assembled films from nanoparticle-labeled antibodies and antigens*; 2002.

7. Wang, T. C.; Cohen, R. E.; Rubner, M. F. *Polyelectrolyte multilayer-based photonic bandgap structures*; 2002.

8. Rubner, M. *Tuning Optical Properties at the Molecular and Supramolecular Level*; 2002.

9. Lvov, Y.; Ariga, K.; Ichinose, I.; Kunitake, T. *Thin Solid Films* **1996,** *285* 797-801.

10. Lvov, Y.; Ariga, K.; Ichinose, I.; Kunitake, T. *Langmuir* **1996,** *12* 3038-3044.

11. Fang, M. M.; Kaschak, D. M.; Sutorik, A. C.; Mallouk, T. E. *J. Amer. Chem. Soc.* **1997,** *119* 12184-12191.

12. Lvov, Y. M.; Sukhorukov, G. B. *Biol. Membrany* **1997,** *14* 229-250.

13. Kotov, N. A.; Magonov, S.; Tropsha, E. *Chem. Mater.* **1998,** *10*(3), 886-895.

14. Eckle, M.; Decher, G. *Nano Letters* **2001,** *1*(1), 45-49.

15. Struth, B.; Eckle, M.; Decher, G.; Oeser, R.; Simon, P.; Schubert, D. W.; Schmitt, J. *European Physical Journal E: Soft Matter* **2001,** *6*(5), 351-358.

16. Massart, R. *IEEE Trans.Magn.* **1981,** *MAG-17*(2), 1247-1248.

17. Correa-Duarte, M. A.; Giersig, M.; Kotov, N. A.; Liz-Marzan, L. M. *Langmuir* **1998,** *14*(22), 6430-6435.

18. Chen, W.; McCarthy, T. J. *Macromolecules* **1998,** *31*(11), 3648-3655.

19. Kotov, N. A. *Nanostructured Materials* **1999,** *12* 789-796.

20. Caruso, F.; Donath, E.; Moehwald, H. *J. Phys. Chem. B* **1998,** *102*(11), 2011-2016.

21. Himpsel, F. J.; Ortega, J. E.; Mankey, G. J.; Willis, R. F. *Advances in Physics* **1998,** *47*(4), 511-597.

22. Grigoriev, I. S.; Melichov, E. Z. *Handbook of Physical Quantities,* CRC Press, Boka Raton, FL **1995.**

23. Stoner, E. C.; Wohlfarth, E. P. *Trans.Roy.Soc.(London)* **1948,** *A240* 599-644.

24. Stoner, E. C.; Wohlfarth, E. P. *IEEE Trans.Magn.* **1991,** *27*(4), 3475-3518.

25. Celinski, Z.; Heinrich, B. *J. Magn. Magn. Mater.* **1991,** *99*(1-3), L25-L30.

26. Ness, H.; Gautier, F. *Journal of Physics: Condensed Matter* **1995,** *7*(33), 6641-6661.

27. Van Langenberg, K.; Hockless, D. C. R.; Moubaraki, B.; Murray, K. S. *Synthetic Metals* **2001,** *122*(3), 573-580.

28. Van Langenberg, K.; Batten, S. R.; Berry, K. J.; Hockless, D. C. R.; Moubaraki, B.; Murray, K. S. *Inorganic Chemistry* **1997,** *36*(22), 5006-5015.

29. Nakamura, K.; Hasegawa, H.; Oguchi, T.; Sueoka, K.; Hayakawa, K.; Mukasa, K. *Development of exchange force microscopy;* 2001.

30. Kotov, N. A.; Haraszti, T.; Turi, L.; Zavala, G.; Geer, R. E.; Dekany, I.; Fendler, J. H. *J.Amer. Chem. Soc.* **1997,** *119* 6821-6832.

31. Tombacz, E.; Dobos, A.; Szekeres, M.; Narres, H. D.; Klumpp, E.; Dekany, I.

     Colloid and Polymer Science **2000,** *278*(4), 337-345.

32. Ebner, A. D.; Ritter, J. A.; Ploehn, H. J. *Separation and Purification Technology*

     1997, *11*(3), 199-210.

33. Shiratori, S. S.; Rubner, M. F. *Macromolecules* **2000,** *33*(11), 4213-4219.

CHAPTER III

LAYER-BY-LAYER ASSEMBLED

FILMS OF SEMICONDUCTOR NANOPARTICLES[i]

Introduction

In the previous chapter thin films of magnetic nanoparticles (NP) were used as a model to study the regularities of the layer-by-layer (LBL) assembly method. It was proven that this method is an effective way for preparing thin films from such NP. These regularities of the LBL assembly, such as linear increase of the UV-vis optical density (O.D.) and close packing of NP inside of the layer upon optimized conditions of the LBL deposition and possibility to manipulate the structure of obtaining films by alternating the dipping sequence, remain the same for the LBL assembly of semiconductor NP [1-3].

Nanometer sized particles of II-VI semiconductors and their size-dependent physical and chemical properties are currently an object of interest in various areas of chemistry and physics [4-11]. The high luminescence (quantum yield $15 - 20$ %) of CdTe nanoparticles, stabilized with thioglycolic acid (TGA), along with their size dependent optical properties, make them a promising material for the engineering of nanoelectronic devices. CdTe nanoparticles have already been found to be useful as components of X-ray and γ-detectors [12], photodiodes [13], and solar cells [14-16].

---

[i] Portions of this chapter have been previously reported in Mamedov, A. A.; Belov, A.; Giersig, M.; Mamedova, N. N.; Kotov, N. A. *J.Am.Chem.Soc.* **2001**, *123*(31), 7738-7739.

For any possible use of such particles in thin films, especially for LED devices, it is necessary to obtain a high density of particles to facilitate charge transfer between them [1,3]. In addition, no quenching of fluorescence should occur due to nanoparticle – polymer interactions.

As it was shown in Chapter I, at the optimized conditions of the LBL deposition the packing and thickness of NP is reproduced from layer to layer, and there is little (if any) restructuring of the NP layer during the polyelectrolyte deposition. These conditions should change a little or not change at all when NP of different sizes are used. This makes formation of thin films with an asymmetric internal structure by varying the LBL deposition sequence. The order of the layers can be used as a powerful tool for optimizing the diverse functional properties of the layered nanostructured materials from biological to electronic. However, the interpenetration of layers and relatively small size of most semiconductor NP (2 - 6 nm) may not give the possibility to distinguish separate layers inside of the film. To visualize them, it makes sense to form strata by assembling of several bilayers of the same type of particles before assembling next type of particles.

The preparation of graded semiconductors with the methods commonly used for this task, such as molecular beam epitaxy and plasma-enhanced chemical vapor deposition [17,18], is difficult, expensive, complex, and sometimes hazardous. The simple and universal LBL deposition method makes it possible to build graded semiconducting materials from a stable aqueous dispersion of semiconductor NP.

The work described in this chapter, deals with the applying of the regularities of the successful LBL assembly of magnetic NP to the optimization of the conditions for the LBL deposition of thiol - stabilized CdTe nanoparticles. Because of their size-dependent

luminescence and, supposedly, size-independent assembly conditions, they are one of the best choices for the preparation and characterization of one-dimensionally graded films. Graded films, prepared by consequent assembly of thiol-caped CdTe nanoparticles will also be discussed in this Chapter. Such films demonstrate possible use as photodetectors, bipolar transistors, waveguides, light-emitters, and nonlinear optical, magnetooptical, and high-speed devices [18]. These types of materials also reveal new phenomena in charge injection, charge carrier dynamics, and light-trapping [17].

Experimental Procedures

Materials

Poly(dimethyldiallylammonium chloride) (PDDA, Mw = 200,000 – 350,000; 20 % wt. in water) and poly(acrylic acid) (PAA, Mw = 450,000) used as organic components in the LBL assembly as well as cadmium perchlorate hydrate $(Cd(ClO_4)_2 \cdot 2H_2O)$, sodium hydroxide (NaOH), and thioglycolic acid (TGA), needed for CdTe nanoparticles synthesis, were bought from Aldrich (Milwaukee, WI). Aluminum telluride (Al_2Te_3), used in the same synthesis was purchased from Gerao Inc. (Milwaukee, WI). Sulfuric acid (H_2SO_4) was obtained from EM Science (Gibbstown, NJ). N_2 gas was obtained from Airgas (Stillwater, OK). LR-white embedding resin, used for TEM sample preparation was obtained from London Resin Company *Ltd.* (Berkshire, England). All chemicals were used without further purification. De-ionized water (> 18.0 $M\Omega$-cm, Barnstead, E-pure system), with an unadjusted pH of approximately 5.5, was exclusively used in all solutions and rinsing procedures.

Synthesis of CdTe nanoparticles

Cadmium telluride (CdTe) NP, stabilized with TGA were prepared according to the procedure described elsewhere [7,8]. Briefly, they where prepared by adding a NaHTe solution to a $Cd(ClO_4)_2 \cdot 2H_2O$ aqueous solution in the presence of TGA as the stabilizing agent. The molar ratio of Cd^{2+} : Te^{2-} : TGA was 1:0.47:2.43. The 0.05 M solution of NaHTe was prepared by titration of a 0.05 M NaOH solution with an excess amount of hydrogen telluride (H_2Te) at $0^{\circ}C$ under an inert atmosphere. H_2Te gas, needed for this reaction, was generated by the direct reaction of Al_2Te_3 with a 0.5 M H_2SO_4 solution. After the titration was complete, the excess amount of hydrogen telluride was removed by bubbling the reaction mixture with N_2 gas for 30 minutes. All initial components of the reaction mixture were saturated with N_2 to obtain an oxygen-free media.

After the reaction was complete, the resulting solution was heated at $96^{\circ}C$. Such a treatment allows for the tuning of the size of the obtained CdTe nanoparticles by varying the heating time. For example, heating the reaction mixture for 30 minutes yielded nanocrystals with a luminescent maxima at 485-505 nm with an average particle size of 2.0 - 3.0 nm, while extension of the heating time to several hours produced a 5.0 - 6.0 nm nanoparticles with a luminescent maxima at 605 - 620 nm. CdTe nanocrystals with emission peaks at 485 - 505 nm, 530 - 545 nm, 570 - 585 nm, and 605 - 630 nm display green, yellow, orange, and red luminescence respectively and will be denoted so accordingly.

Layer-by-layer assembly of CdTe nanoparticles

As substrates for CdTe nanoparticles LBL assembly, glass slides, silicon wafers, and cellulose acetate (CA) films were used. Transparent substrates were needed for UV-visible spectroscopy and luminescence measurements. Since glass does not absorb light at wavelengths higher than 320 nm, it was suitable as a substrate for such types of measurements. Silicon wafer substrates were used for the AFM study of the LBL assembled films. Both the silicon wafers and glass slides were cleaned with a hot Nochromix solution in concentrated H_2SO_4 followed by a rinsing with DI water. The surface of a flexible cellulose acetate film, needed for the TEM study of the graded film, was partially hydrolyzed with 0.1 M NaOH for 5 minutes to facilitate the LBL assembly, and then thoroughly rinsed with DI water.

As an organic components of LBL assembly system, positively charged PDDA and negatively charged PAA were used. A typical deposition step consisted of: (1) deposition of the PDDA from its 1% aqueous solution (pH = 9) for 10 minutes; (2) two rinses with DI water for 1 minute each; (3) deposition for 20 minutes of CdTe nanoparticles from as-synthesized dispersion (pH = 9 – 10); and (4) two rinses with DI water for 1 minute each. To enhance the LBL assembly of the CdTe NP, the precursor layer of the PDDA/PAA was deposited on a clean substrate surface in the same fashion that was used for LBL assembly of magnetic NP. This layer formed a uniform surface coating, providing better adsorption for subsequent NP layers. PAA was assembled from its 1% aqueous solution (pH = 3.5)

The graded LBL assembled films were prepared on glass slides and cellulose acetate substrates from "green", "yellow", "orange", and "red" nanoparticles to produce a

model of NP rainbow. Typically 5-10 PDDA/NP bilayers of each of four luminescent colors were deposited. The precursor layer of PDDA/PAA was assembled before carrying out preparation of the graded film. The surface of the cellulose acetate film was partially hydrolyzed with NaOH to add additional charges to it.

Luminescence spectroscopy

The progress of nanoparticle growth in the reaction media as well as the progress of their LBL assembly was monitored with Fluorolog 3 and Fluoromax 2 from JY SPEX by registering the luminescence spectra of the particles. During the nanocrystal growth step, the spectra were taken every 15-20 minutes. To check the growth of the graded CdTe film, fluorospectra were taken after the deposition of PDDA/CdTe bilayers of each color. The right angle registration mode with no intermediate filters was utilized in these measurements.

Transmission electron microscopy

Transmission electron microscopy (TEM) and high resolution transmission electron microscopy (HRTEM) images were taken on a Philips CM 12 instrument, equipped with super twin high resolution lenses and Zeiss digital camera. The instrument was operated at 120 kV. A graded CdTe film was embedded in a LR-white embedding resin according to the specifications recommended by the manufacturer. The embedded film was cross-sectioned utilizing a Reichert Ultracut E ultramicrotome (Leica) with "Diatome" diamond knife. The obtained 25-30 nm sections were placed on a 200 mesh copper grid coated with formvar, and then dried in a decicator for 30 minutes before being placed in the microscope.

Confocal laser scanning microscopy

The graded CdTe film was checked with a confocal laser scanning microscopy. The micrographs were taken with a Leica TCS SP microscope, equipped with 63x Plan APO 1.2 NA water immersion and 100x Plan APO 1.4 NA oil immersion objectives. The CdTe nanoparticles of the film were excited with an Ar − UV laser. The images were processed with Leica TCS NT software.

Results and Discussion

Synthesis of CdTe nanoparticles

The aqueous solutions of nanoparticles obtained according to the procedure described in the experimental part of this chapter, have narrow and symmetric peaks ranging from 495 nm for "green" CdTe to 620 nm for "red" CdTe NP (Figure 23). The set of vessels, shown on Figure 23 A, contain solutions of TGA stabilized CdTe excited with a UV lamp (λ_{ex} = 368 nm). The average particle size gradually increases from 2.0 − 3.0 nm for "green" NP to 5.0 − 6.0 nm for "red" NP as it was determined by HRTEM. The arrows indicate the solutions of which the luminescence spectra (Figure 23 B) were taken. A wider peak for the "yellow" CdTe solution can be attributed to the higher polydispercity of CdTe nanoparticles compared to "green", "orange", and "red" solutions.

LBL deposition of CdTe nanoparticles

The LBL deposition of CdTe nanoparticles was performed on glass slides and silicon wafers. The progress of the assembly was monitored by UV-vis spectroscopy and
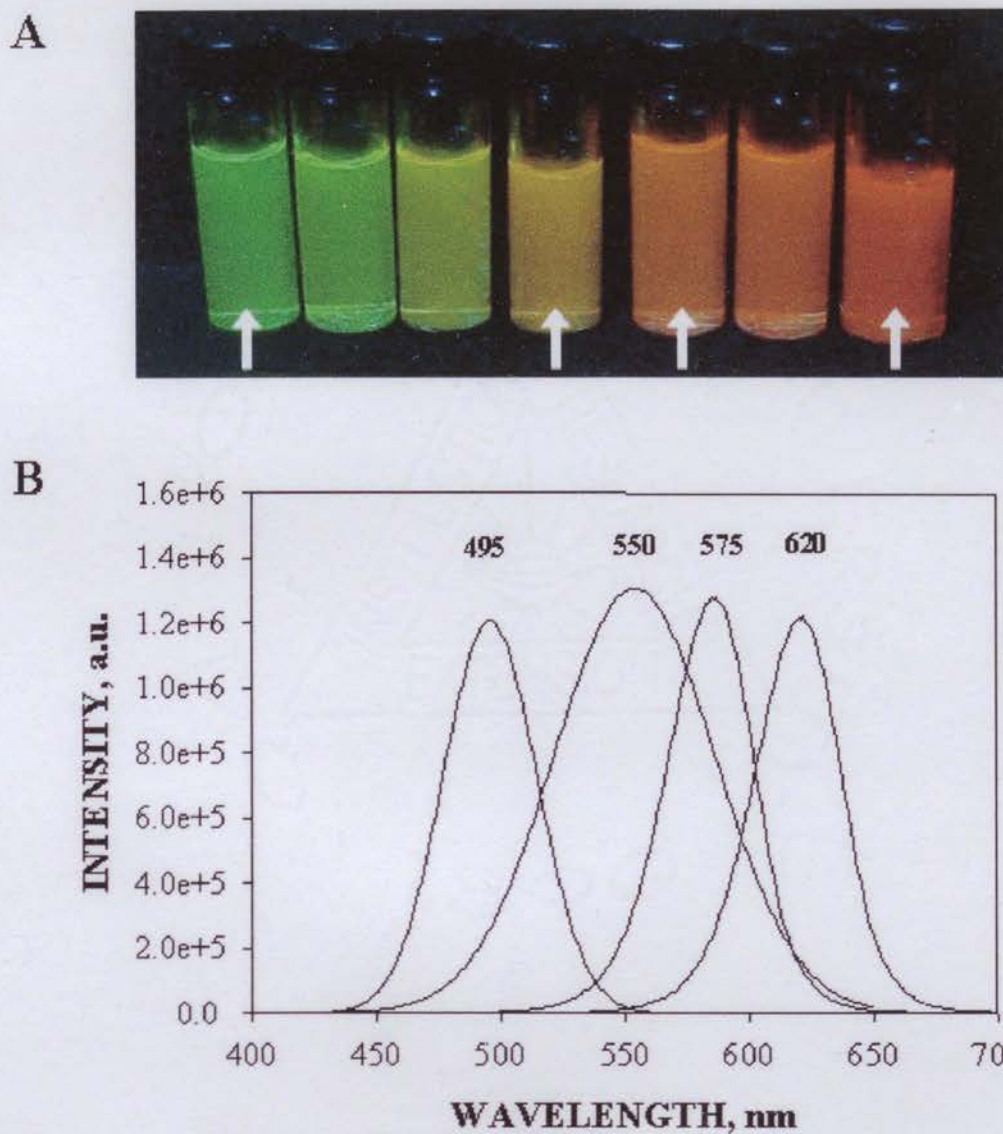
Figure 23. (A) Optical image of vessels, containing aqueous dispersions of CdTe nanoparticles excited with UV lamp. The average particle size changes gradually from 2.0 - 3.0 nm for solution, exhibit green luminescence, to 5.0 – 6.0 nm for solution exhibit red luminescence. Arrows indicate solutions, luminescence spectra of which (B) were taken.

AFM. Figure 24 shows the UV-vis spectra of a growing film of "green" CdTe nanoparticles. The "bumps" on the spectra correlate to the UV-vis adsorption peaks for the CdTe nanoparticles in the film. As in the case of the assembly of the magnetic nanoparticles the linear dependence of the increment of optical density with the number of adsorption cycles was observed (Figure 24 B). The linear dependence correlates with data, published elsewhere for the LBL assembly of the semiconductor NP [2,3,9]. Observation of the growing film with AFM revealed a completely covered surface with a dense packing of CdTe nanoparticles after the deposition of one PDDA/CdTe bilayer, adsorbed on a precursor PDDA/PAA bilayer (Figure 25 A, B). When a layer of PDDA was adsorbed on top of the CdTe NP (Figure 25 C), the roughness of the growing film was reduced. This can be attributed to a greater number of the negative charges in the spaces between the closely packed nanoparticles, which leads to the preferential polymer adsorption (Figure 25 D).

Graded films from CdTe nanoparticles: preparation

The assembly of a graded CdTe film started with a deposition of a precursor PDDA/PAA layer on a substrate. This procedure resulted in a uniform coating which resulted in a successful LBL growth of the film. The assembly of the NP started with an adsorption of 5 bilayers of PDDA/"green" CdTe NP, followed by 5 bilayers of PDDA/"yellow", "orange", and "red" CdTe NP respectively. A sketch of the structure of the obtained film, along with the corresponding band – gap progression of the CdTe NP inside of film, is shown in Figure 26. With the complete addition of new layers of bigger nanoparticles, a luminescence spectrum of the LBL stack was taken (Figure 27). When
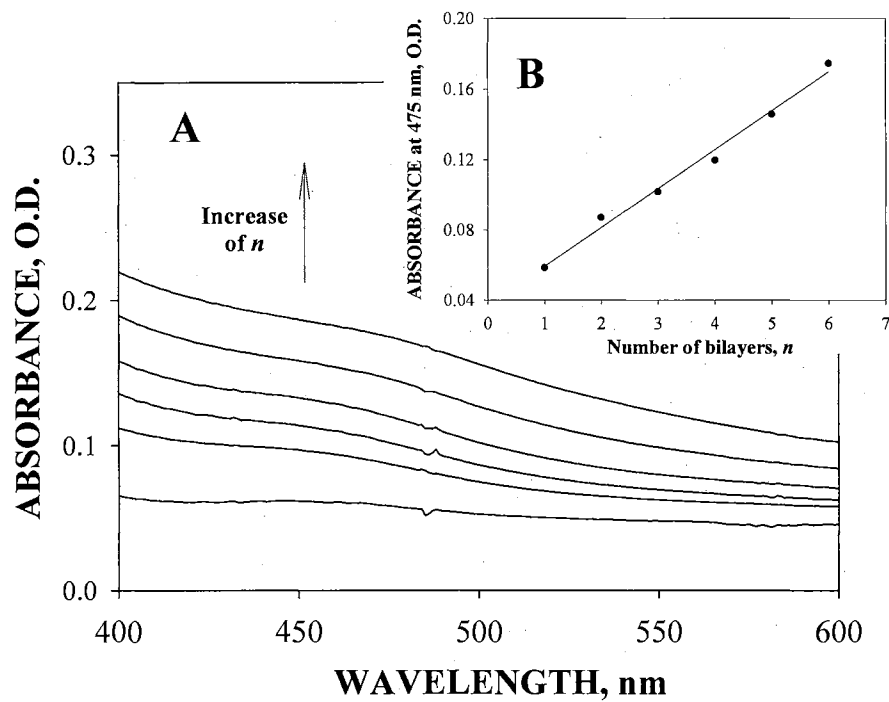
Figure 24 (A) UV-vis adsorption spectra of "green" nanoparticles with glass slide as a substrate. (B) Dependence of O.D. at 475 nm of growing film on the number of absorbed PDDA/CdTe bilayers. Only NP absorb light at this wavelength.
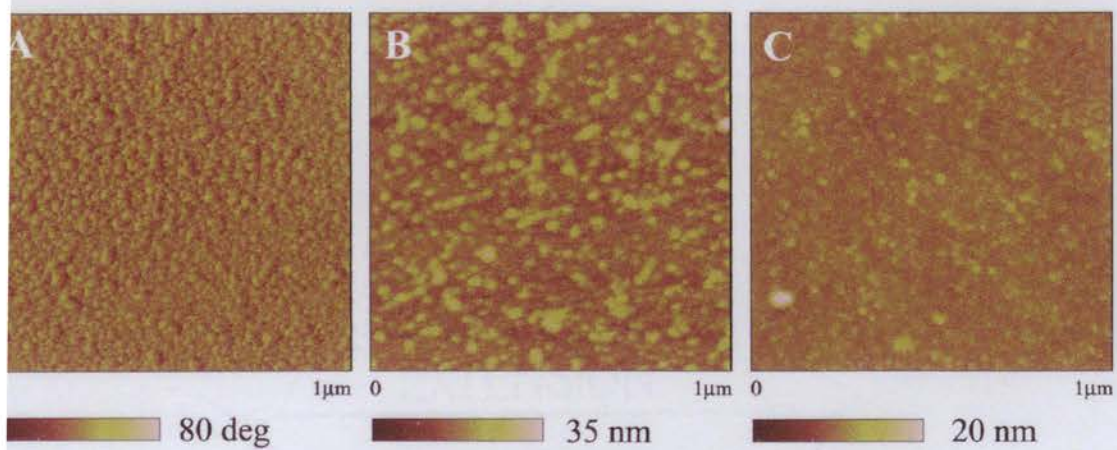
Figure 25. AFM phase (A) and topography (B, C) images of PDDA/CdTe (A, B) and PDDA/CdTe/PDDA (C), adsorbed on precursor PDDA/PAA bilayer.
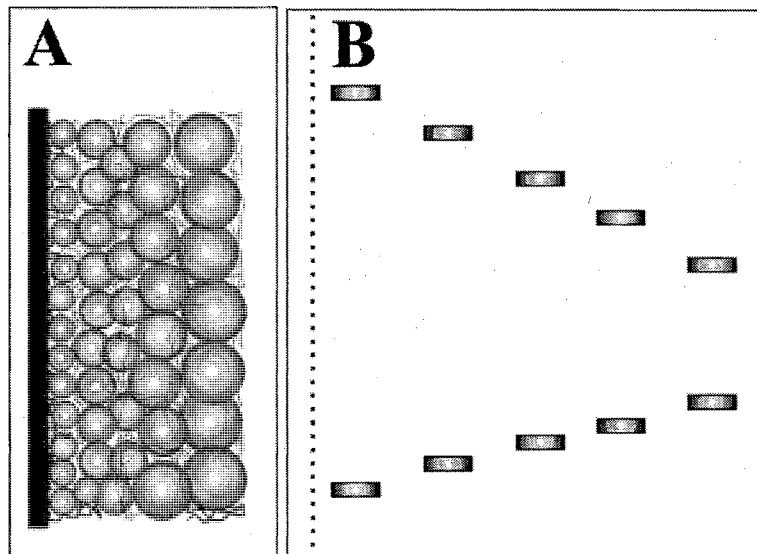
Figure 26. Schematic view of (A) a gradient film and (B) corresponding band-gap progression.
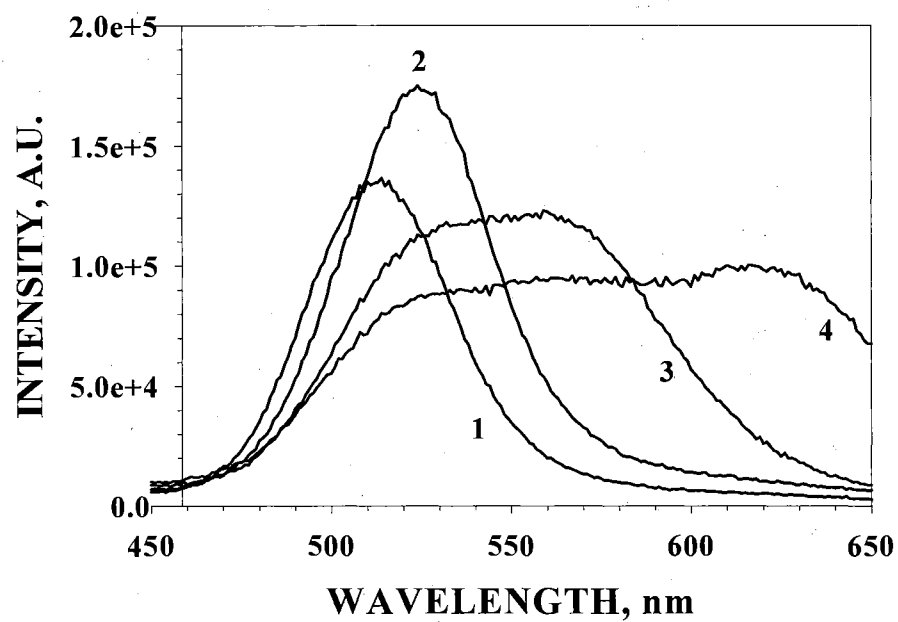
Figure 27. Luminescence spectra of thin films obtained after the sequential deposition of five bilayers of (1) "green", (2) "yellow" (3) "orange", and (4) "red" CdTe nanoparticles.

CdTe nanoparticles of a bigger size were added to the film, the luminescence of the assembly broadened and shifted toward the red part of the electromagnetic spectra. Finally, after the addition of NP of each of four colors, the luminescence spectra of the film had a plateau appearance with an almost equal emission intensity in a wide range of wavelengths. The red shift of the fluorescence in comparison to the original spectra of CdTe nanoparticles (Figure 23) can be attributed to the excitation energy transfer from smaller NP to larger ones [19,20].

Graded films from CdTe nanoparticles:
evaluation of the internal structure

To evaluate the internal structure of a gradient CdTe film, it was assembled on a flexible CA substrate. Then the LBL stack along with substrate was embedded into epoxy resin and then cross-sectioned. The choice of a CA substrate can be rationalized by the fact that it does not require a complicated slicing procedure. This makes a thin and flexible CA film preferable to those of traditional glass or silicon wafers. The surface of the CA was pretreated by partial hydrolysis with 0.1 M NaOH. Such pretreatment resulted in the greater adsorption rate during LBL assembly process [21]. A graded film consisting of 5 bilayers of each "green", "yellow" and "red" CdTe nanoparticles was assembled in the manner described above. Embedding and cross-sectioning of the LBL stack resulted in 25 nm thick slices, which were analyzed with TEM.

The asymmetry of the obtained film is visualized as the difference in image density on the "red" and "green" sides of the LBL stack. The side of the film containing bigger "red" CdTe nanoparticles appears to be darker. This is explained by a greater percentage of heavier elements (Cd and Te) on this side of the assembly, leading

to the stronger electron beam scattering (Figure 28 A). HRTEM images of the "green", "yellow", and "red" parts of the film (Figures 28 B – D) show the presence of CdTe nanoparticles inside of a polyelectrolyte matrix with an average diameter of 2 – 4 nm for the "green" and "yellow" and 5 – 6 nm for the "red" sides of the assembly. This correlates with the emission wavelength of the particles. The low contrast of HRTEM micrographs, as well as the impossibility of distinguishing the differences in sizes of the "green" and "yellow" CdTe nanoparticles inside of the LBL stack, should be attributed to a stacking of at least 3 – 4 "red" and 6 – 10 "green" and "yellow" nanoparticles on top of each other inside of the slice.

The gradient nature of the resulting CdTe film was confirmed using confocal laser scanning microscopy. The sample consisting of 10 bilayers of "green", "yellow", "orange", and "red" nanoparticles, was assembled on a CA film. The stacks of multilayers, made from NP of the same color, were separated from each other by additional interlayers of PDDA/PAA. A series of luminescence images were obtained at different focus depths inside the assembly when the CdTe nanoparticles in the film were excited with a UV laser. The images were processed with standard Leica TCS NT software and a cross-sectional image was obtained without physical sectioning of the film (Figure 29 A). The gradual change of luminescence color from green on one side to red on the other side of the film, as the corresponding size of the NP inside of the film increases, can be clearly seen. The absence of well separated color layers inside of the obtained "nanorainbow" results mainly from the low resolution of technique used. There is a certain degree of interpenetration of the separate nanoparticle layers which may also influence the cross-sectional image.
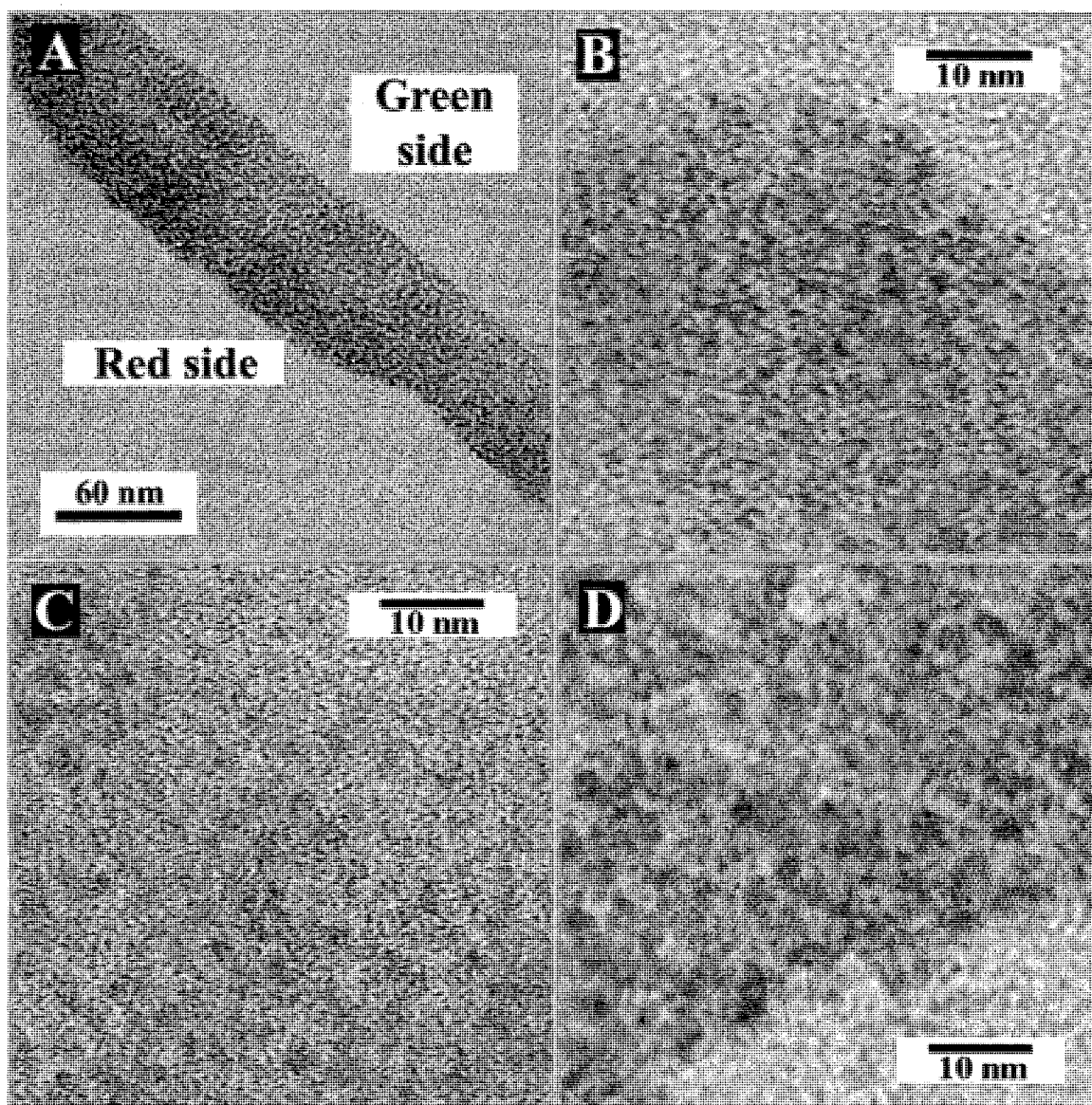
Figure 28. (A) TEM image of cross-sections of a graded CdTe film made from five bilayers of "green", "yellow", and "red" nanoparticles. (B – C) HRTEM images of "green" (B), "yellow" (C), and "red" (D) parts of LBL assembly.
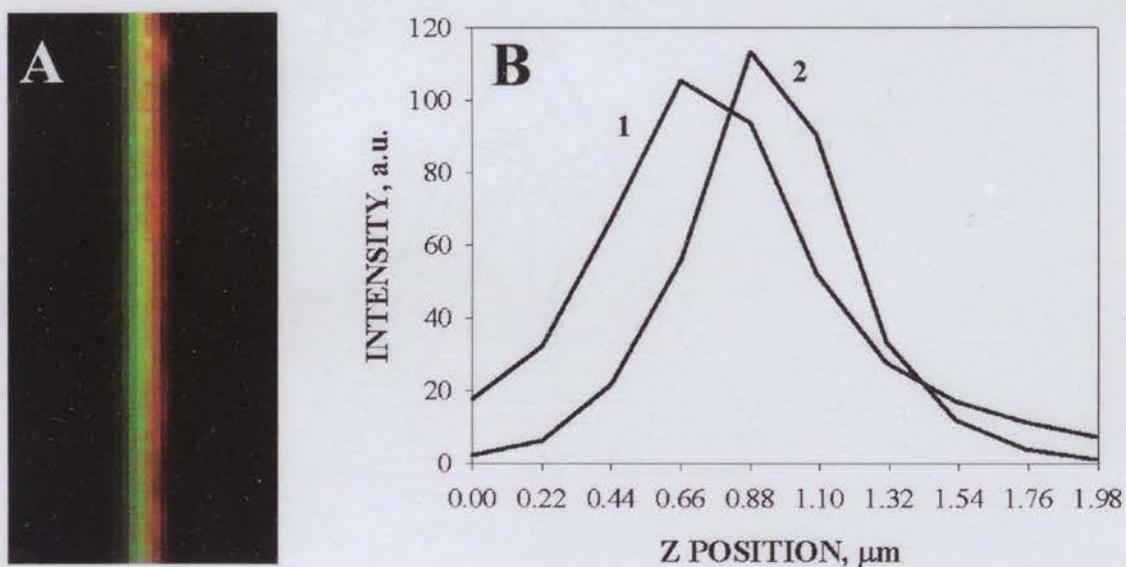
Figure 29. (A) Cross-sectional confocal microscopy image of the graded film, made from 0 bilayers of "green", "yellow", "orange", and "red" CdTe nanoparticles. Additional interlayers of PDDA/PAA separate stacks made of nanoparticles of the same size. (B) dependence of green (1) and red (2) luminescence signals intensity on focus depth during cross-sectional analysis.

By the difference in the positions of the maxima for the red and green channels of intensity vs. the Z-position (focus depth) plot (Figure 29 B) the thickness of the obtained CdTe assembly was estimated to be 220 ± 20 nm. This correlates quite well with the expected thickness of the film. One dipping cycle during an assembly results in the formation of a 3 – 7 nm thick PDDA/CdTe bilayer depending on the size of the particles used. The average thickness of a PDDA/CdTe bilayer can be estimated to be 5 nm. PAA, assembled on top of PDDA, forms a 5 nm thick bilayer as determined by ellipsometry. The thickness of graded film can be estimated by adding up these numbers: 5 x 40 + 3 x 5 = 215 nm, which matches surprisingly well the thickness estimate from the confocal study. It is important to mention, that since the maximum possible magnification of the confocal microscope was 100X with an oil immersion objective, the correct thickness estimation for the CdTe graded film can be done for relatively thick samples.

Conclusion

Layer-by-layer assembled multilayers of luminescent CdTe nanoparticles have been prepared on a number of substrates. UV-vis monitoring of the assembly process shows a linear dependence of the optical density on the number of deposited bilayers. NP completely covered the substrate surface and formed uniform closely packed layers as was demonstrated by AFM. Sequential assembly of the CdTe nanoparticles of different sizes, ranging from 2 – 3 nm to 5 – 6 nm, opens the possibility of preparing films with the gradient structures utilizing the LBL assembly method. The combination of quantum-size effects with the gradient nature of the obtained CdTe films gives the opportunity to study new physical and optical effects, as well the optimization of existing applications using

nanoparticle thin films based on charge transfer. At the same time it should be mentioned that the characteristic distance for CdTe LBL films, at which a change in properties can be programmed, should exceed 100 nm. This number is significantly greater than the average thickness of one bilayer or the diameter of nanoparticles. However, this observation does not prevent the organization of the NP on a much smaller scale. It is possible to tune some parameters, such as polarizability and the refractive index, on the molecular level in such asymmetric assemblies, which may lead to the discovery of unique photonic and electronic devices.

References

1. Lesser, C.; Gao, M.; Kirstein, S. *Materials Science & Engineering, C: Biomimetic and Supramolecular Systems* **1999,** *C8-C9* 159-162.

2. Rogach, A. L.; Koktysh, D. S.; Harrison, M.; Kotov, N. A. *Chemistry of Materials* **2000,** *12*(6), 1526-1528.

3. Sun, J.; Gao, M.; Feldmann, J. *Journal of Nanoscience and Nanotechnology* **2001,** *1*(2), 133-136.

4. Eychmueller, A.; Mews, A.; Weller, H. *Chemical Physics Letters* **1993,** *208*(1-2), 59-62.

5. Mews, A.; Eychmueller, A.; Giersig, M.; Schooss, D.; Weller, H. *Journal of Physical Chemistry* **1994,** *98*(3), 934-941.

6. Rockenberger, J.; Troger, L.; Kornowski, A.; Vossmeyer, T.; Eychmuller, A.; Feldhaus, J.; Weller, H. *Berichte der Bunsen-Gesellschaft* **1997,** *101*(11), 1613-1616.

7. Rogach, A. L.; Katsikas, L.; Kornowski, A.; Su, D.; Eychmueller, A.; Weller, H. *Berichte der Bunsen-Gesellschaft* **1996,** *100*(11), 1772-1778.

8. Rogach, A. L.; Katsikas, L.; Kornowski, A.; Su, D.; Eychmuller, A.; Weller, H. *Berichte der Bunsen-Gesellschaft* **1997,** *101*(11), 1668-1670.

9. Gao, M.; Kirstein, S.; Rogach, A. L.; Weller, H.; Mohwald, H. *Advances in Science and Technology (Faenza, Italy)* **1999,** *27*(Innovative Light Emitting Materials), 347-358.

10. Talapin, D. V.; Haubold, S.; Rogach, A. L.; Kornowski, A.; Haase, M.; Weller, H. *Journal of Physical Chemistry B* **2001,** *105*(12), 2260-2263.

11. Talapin, D. V.; Rogach, A. L.; Mekis, I.; Haubold, S.; Kornowski, A.; Haase, M.; Weller, H. *Colloids and Surfaces, A: Physicochemical and Engineering Aspects* **2002,** *202*(2-3), 145-154.

12. Redus, R.; Squillante, M.; Gordon, J.; Knoll, G.; Wehe, D. *Nucl.Instrum.Methods Phys.Res., Sect.A* **1994,** *353*(1-3), 324-327.

13. Bahir, G.; Ariel, V.; Garber, V.; Rosenfeld, D.; Sher, A. *Applied Physics Letters* **1996,** *68*(17), 2455.

14. Ferekides, C.; Britt, J.; Ma, Y.; Killian, L. *Conference Record of the IEEE Photovoltaic Specialists Conference* **1993,** *23rd* 389-393.

15. Ferekides, C. S.; Dugan, K.; Ceekala, V.; Killian, J.; Oman, D.; Swaminathan, R.; Morel, D. L. *Conference Record of the IEEE Photovoltaic Specialists Conference* **1994,** *24th*(1994 IEEE First World Conference on Photovoltaic Energy Conversion, Vol. 1), 99-102.

16. Ferekides, C.; Britt, J. *Solar Energy Materials and Solar Cells* **1994,** *35*(1-4), 255-262.

17. Vlaev, S.; Velasco, V. R.; Garcia-Moliner, F. *Physical Review B: Condensed Matter* **1995,** *51*(11), 7321-7324.

18. Aigouy, L.; Mathet, V.; Liaci, F.; Gil, B.; Briot, O.; Briot, N.; Cloitre, T.; Averous, M.; Aulombard, R. L. *Physical Review B: Condensed Matter* **1996,** *53*(8), 4708-4721.

19. Kagan, C. R.; Murray, C. B.; Bawendi, M. G. *Physical Review B: Condensed Matter* **1996,** *54*(12), 8633-8643.

20. Kagan, C. R.; Murray, C. B.; Nirmal, M.; Bawendi, M. G. *Physical Review Letters* **1996,** *76*(9), 1517-1520.

21. Mamedov, A. A.; Kotov, N. A. *Langmuir* **2000,** *16*(13), 5530-5533.

CHAPTER IV

LAYER-BY-LAYER ASSEMBLED FILMS OF

SINGLE WALL CARBON NANOTUBES

Introduction

The work described in this chapter was devoted to applying the regularities for successful layer-by-layer (LBL) deposition of nanoparticles (NP) studied in previous chapters to the preparation of multilayered composites based on asymmetric inorganic nanomaterials such as single wall carbon nanotubes (SWNT).

Intensive studies of composite materials based on SWNT have been prompted because of their exceptional mechanical properties in combination with their electrical and thermal conductivity. However, on the background of the spectacular achievements in manufacturing SWNT-based electronic devices [1-4], the mechanical and electrical characteristics of SWNT-doped polymers have shown only modest strength and conductivity improvement with respect to other hybrid materials [5-7]. Although substantial advances have been made [8], the mechanical characteristics of SWNT-doped polymers have been proven to be noticeably less than their highly anticipated potential. SWNT are known for poor solubilization in solvents and polymeric matrixes, which results in the phase segregation of SWNT composites. Severe structural inhomogeneities result in the physical separation of SWNT when mechanical stress is applied, leading to

the premature failure of the material. The connectivity with the uniform distribution of SWNT within the matrix is believed to be the essential requirements for obtaining strong SWNT composites [9].

Recent advances in the chemical modification of SWNT afford new approaches to improving the mechanical properties of SWNT composites and to mitigating the solubility problem. Once a stable colloid solution of the charged SWNT was obtained, it became possible to utilize them in the LBL assembly. Since the SWNT used in this study were up to 2 micrometers long and only 1.5-2 nm thick, it would be intriguing to determine the modes of alignment of nanotubes inside of the layer during deposition. Of course, the alignment step would only possible upon success of LBL deposition of non-aligned SWNT. The influence of the flow rate on arrangement of the SWNT inside of the deposited layer was an object of interest besides LBL deposition and characterization of multilayers of non-aligned nanotubes.

Experimental Procedures

Materials

Branched poly(ethyleneimine) (PEI-b, M_W = 70,000) and poly(acrylic acid) (PAA, Mw = 450,000) used as the organic components for LBL assembly of SWNT, hydrogen peroxide (H_2O_2) for piranha solution preparation, and sodium hydroxide (NaOH) for pH adjustments were purchased from Sigma-Aldrich (Milwaukee, WI). Sulfuric acid (H_2SO_4), used for the preparation of piranha solution, was obtained from EM Science (Gibbstown, NJ). Ar and N_2 gases were obtained from Airgas (Stillwater, OK). All chemicals were used without further purification. De-ionized (DI) water (> 18.0

MΩ-cm, Barnstead, E-pure system), was exclusively used in all solutions and rinsing procedures. Unless stated otherwise, DI water with an unadjusted pH of approximately 5.5 has been used.

Synthesis and modification of single wall carbon nanotubes[i]

Single-wall nanotubes (SWNT) were manufactured by laser vaporization of carbon rods doped with Co, Ni and FeS in an atmosphere of $Ar:H_2$. A suspension of SWNT raw material was refluxed in 65% aqueous HNO_3 and subsequently purified by centrifugation. Supplemented with sonication, this treatment results in the partial oxidation of the caps and side-walls to the extent of approximately 5 % of the total number of carbon atoms [10]. The presence of carboxylic acid groups makes possible the preparation of aqueous dispersions of SWNT. Relatively stable colloidal solutions were obtained after 1 minute sonication of solid SWNT in deionized (DI) water.

Layer-by-layer assembly of SWNT

The negatively charged SWNT were layer-by-layer assembled with a positively charged polyelectrolyte, such as branched PEI-b. Glass slides and silicon wafers were used as substrates for LBL assembly. The surfaces of the substrates were thoroughly cleaned in the following manner: (1) treatment with piranha solution (mixture of 30% H_2O_2 and concentrated H_2SO_4 in 1:3 ratios), (2) DI water rinsing to remove traces of sulfuric acid, (3) sonication for 15 minutes, and (4) final rinse with DI water. To insure successful growth of the SWNT film from first deposition cycle, precursor PEI-b/PAA

[i] This part of work has been done in collaboration with Dr. Dirk M. Guldi, Radiation Laboratory, University of Notre Dame, Notre Dame, IN, USA and Dr. Maurizio Prato, Departaminto di Scienze Farmaceutiche, Universita di Trieste, Trieste, Italy

bilayer was assembled, with deposition times of 20 and 10 minutes respectively. A 1% aqueous dispersion of both polymers has been used. The pH value of the PAA solution used for the fabrication of the precursor layer was not adjusted and remained at approximately 3.0.

The typical deposition cycle for the LBL assembly of the SWNT multilayers consisted of the four following steps: (1) adsorption of PEI-b for 10 minutes from its 1% aqueous solution, (2) rinsing with DI water two times for 1 minute each, (3) adsorption of SWNT for 1 hour, and (4) rinsing with DI water two times for 1 minute each. The pH values of the rinsing water and PEI-b were adjusted to 8.5 using 0.1 M NaOH. The aqueous solution of the SWNT had pH value 6.8 and did not require any further adjustments.

Since the overall negative charge of the SWNT used was fairly small, after every 5th deposition cycle, a layer of SWNT was replaced with a layer of PAA, which improves the deposition process and provides a convenient chemical anchor for subsequent chemical modification. PAA was adsorbed from a 1% aqueous solution with pH = 6.5 for 10 minutes.

The ionic and other conditions of the LBL assembly made repetition of the dipping cycles as many times as needed possible with linear growth of the multilayers, which enables the preparation of films with any desirable thickness and architecture.

Weight load calculations

The weight load calculations were done based on a carbon to nitrogen ratio, calculated from the carbon and nitrogen EDAX peak integrals, obtained on the SEM,

which was equipped with an EDAX system. The molecular formula of PEI-b repeating units (Figure 3 in Chapter 1) shows, that the atomic ratio of N to C atoms is 1:2. EDAX determines the elemental composition of the sample surface with the penetration of the electrons into the sample no more than 10 nm. Assuming that in the surface area of the film N atoms were present only in PEI-b and C atoms were present in both PEI-b and SWNT, the estimate weight of SWNT in measured area (W_{SWNT}) can be calculated as:

$$W_{SWNT} = Mw_{SWNT} (N_C - 2N_N) \qquad (1)$$

where: Mw_{SWNT} is the molecular weight of a SWNT repeating unit and equal atomic weight of carbon (i.e. 12) (the presence of some oxygen atoms on surface of modified nanotubes is neglected, due to their low content), N_C and N_N represent the number of carbon and nitrogen atoms respectively. These numbers were chosen so that N_C / $2N_N$ gives the carbon to nitrogen ratio, measured with the EDAX system.

The weight of PEI-b in the same area (W_{PEI-b}) can be estimated as:

$$W_{PEI-b} = Mw_{PEI-b} (N_N / 3) \qquad (2)$$

where: Mw_{PEI-b} equals the molecular weight of a PEI-b repeating unit and 3 is the number of nitrogen atoms per one PEI-b repeating unit.

Finally, the weight load of SWNT in a film can be estimated as;

$$[W_{SWNT} / (W_{SWNT} + W_{PEI-b})]*100\% \qquad (3)$$

Raman spectroscopy

Raman measurements were performed using an ISA U-1000 micro-macro Raman spectrometer in a backscattering configuration with a 100X objective lens. Unpolarized Raman spectra were taken at a scan rate 0.83 cm^{-1}/s. A 514.5 nm laser beam of 50-mW

power was directed into the sample which was placed on a horizontal adjustable holder with the backscattered light collected at right angles to the incident beam.

Resistivity measurements

The measurements of the influence of humidity on resistivity of the obtained SWNT films was carried out in a sealed box though which nitrogen gas, saturated with water vapor, was passed. The humidity value inside the box was controlled using a HANNA Instruments hydrometer, model HI8064. Before carrying out the measurements, the films were dried in a desiccator overnight. At each measuring point, the sample was allowed to saturate with water for at least 30 minutes before any measurements were taken.

The electrical resistivity (in Ωm) of the obtained SWNT films was calculated according the formula:

$$R = \frac{R_{exp}dw}{l} \tag{4}$$

Where: R_{exp} – experimental reading of resistivity between two points (in Ω)

l – distance between contacts of resistometer

d – thickness of the tested film

w – width of the tested film

Alignment of carbon nanotubes

The parallel alignment of the nanotubes during the layer-by-layer assembly was obtained by using a closed loop laminar flow cell (Figure 30 A) equipped with a mini-pump. The edge of a 1 x 1 cm silicon wafer, which faced the SWNT dispersion flow, was
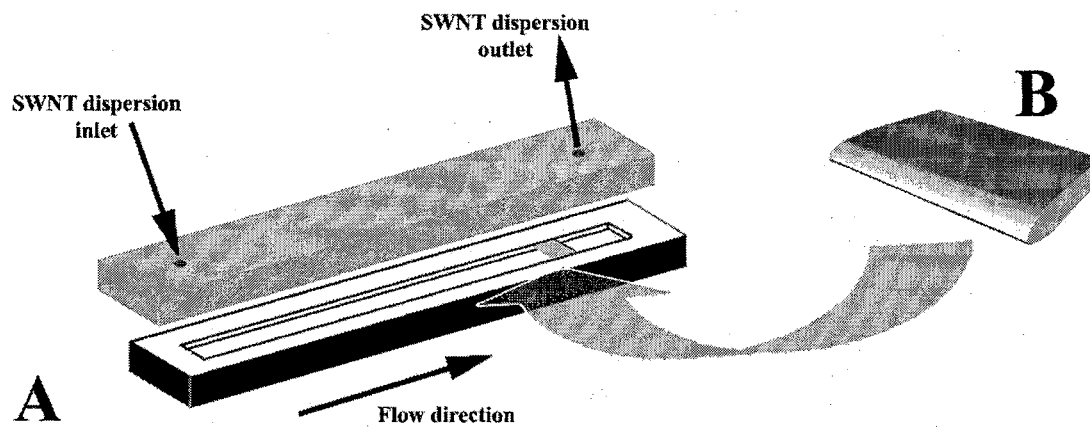
Figure 30. (A) Sketch of laminar flow cell, used for alignment of carbon nanotubes. (B) Schematic view of polished silicon wafer edge, which faced SWNT dispersion flow. Arrow indicates the position of silicon substrate inside of cell.

shaped as shown on Figure 30 B in order to avoid turbulence during the LBL deposition. The cleaning procedure, deposition of both the precursor bilayer and the monolayer of PEI-b were performed according to the procedure described above. Subsequently the substrate was transferred into the flow cell. A stream of SWNT dispersion with 0-11 mL/min variable flow rate regulated by a mini-pump, was directed along the substrate surface for 2 hours. Upon finishing the alignment in a flow procedure, the substrate with nanotube assembly was washed with DI water two times for 1 minute each and air dried.

Results and discussion

Layer-by-layer assembly

PEI-b was utilized as the organic component of the SWNT LBL assembled films. The glass slides and silicon wafers, used as the substrates for LBL deposition, were cleaned according the procedure described in the experimental section.

The layer-by-layer assembly process of SWNT has been monitored by means of Atomic Force Microscopy (AFM) and UV-visible spectroscopy. The AFM study reveals that at each LBL deposition step, a submonolayer of SWNT was deposited, similar to that displayed in other PE/NP systems. In contrast to the LBL deposition of magnetic and semiconductor NP, when monolayer of particles was formed, the final morphology of the (PEI-b/PAA)(PEI-b/SWNT)$_5$ multilayer unit can be described as a dense layer of intricately intertwined individual carbon nanotubes in bundles which are 4-9 nm in diameter (Figure 31 A). It was observed that the nanotubes uniformly cover the entire surface of the substrate without any evidence of phase separation. Also, unlike the previous examples of surface-modified SWNT/polymer composites [8], the presence of
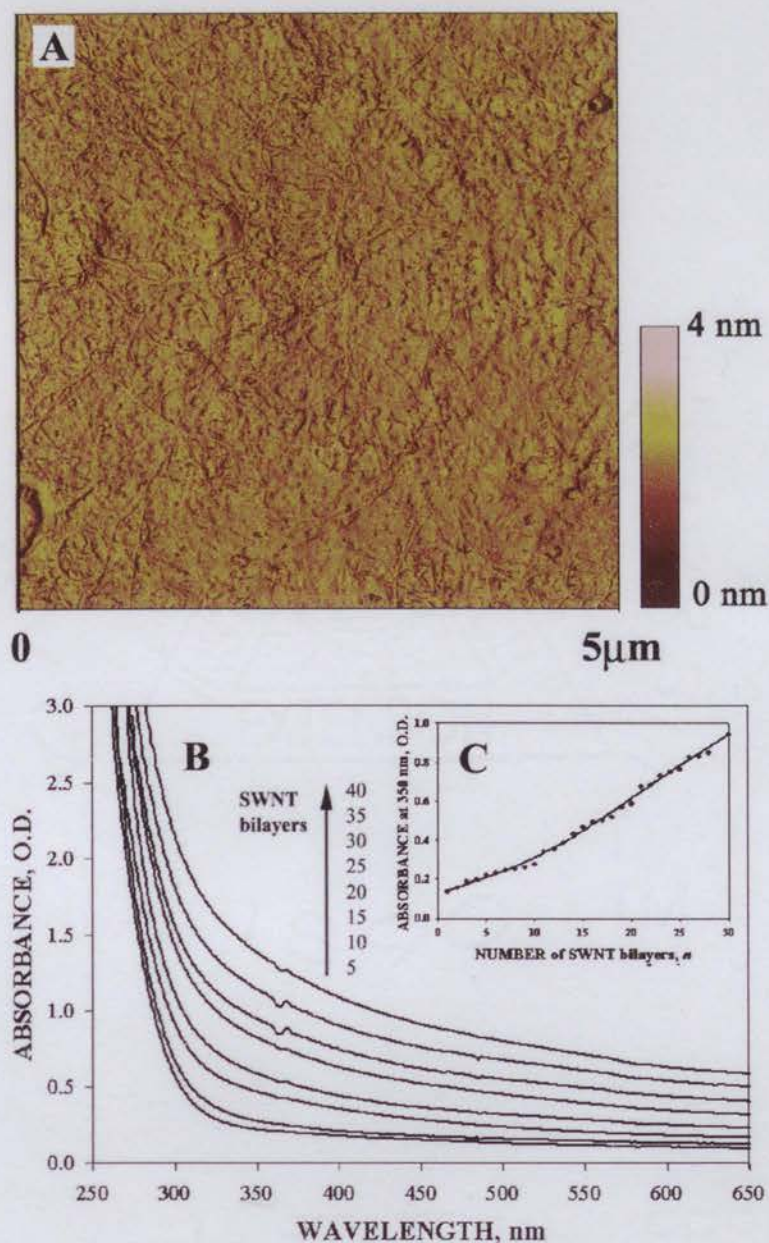
Figure 31. (A) AFM image of a Si wafer, bearing (PEI-b/PAA)(PEI-b/SWNT)₅ unit. (B) sequential UV-vis spectra of a glass substrate in the course of the LBL deposition of WNT. The spectra were taken for a total number of (PEI-b/SWNT) bilayers indicated in the graph. (C) Dependence of O.D. at 350 nm of growing film on number of absorbed WNT bilayers.

oxidized flat graphite sheets and other forms of carbon colloids was very small. Both these factors contributed to the mechanical properties of the final composites. UV-vis spectra (Figure 31 B), as in the case of NP, show that the optimized assembly conditions, used for SWNT, allow for the repeating of the dipping cycles as many times as needed with linear growth of the multilayers. The linear dependence of increment of O.D. with the adsorption of additional SWNT layers was observed at 350 nm (Figure 31 C). Assemblies with a structure of ((PEI-b/PAA)(PEI-b/SWNT)$_5$)$_6$ and ((PEI-b/PAA)(PEI-b/SWNT)$_5$)$_8$,which were used in this study, displayed an SWNT content of 50 +/-5 wt% as calculated from carbon and nitrogen EDAX peak integrals. Previously reported composites made with modified SWNT revealed strong inhomogeneities even with SWNT loadings as low as 6-8% [6].

The quality of the nanotube material can also be confirmed by Raman spectroscopy. The characteristic peaks for SWNT (Figure 32), *e.g.* the radial breathing mode at ~182 cm^{-1} and the tangential C-C stretching modes located at ~1560 cm^{-1} and ~1583 cm^{-1}, are very sharp and narrow indicating a high uniformity in the SWNT and a low level of impurities present in the films. A barely visible peak at ~1340 cm^{-1} reveals the traces of disordered carbon structures. From the correlation between the frequency of the radial breathing mode, ν, and SWNT diameter, d, expressed as $d = 223.75/\nu$ [11], gives an estimate of $d = 1.2$ nm, which agrees well with the SWNT diameter, which was obtained from the AFM images of many individual nanotubes (Figure 33). The length of the nanotubes was measured to be 2-7 micrometers.

In rarified films with reduced intertwining, obtained by short SWNT adsorption times, the geometry of the individual SWNT in the LBL assemblies can be examined.
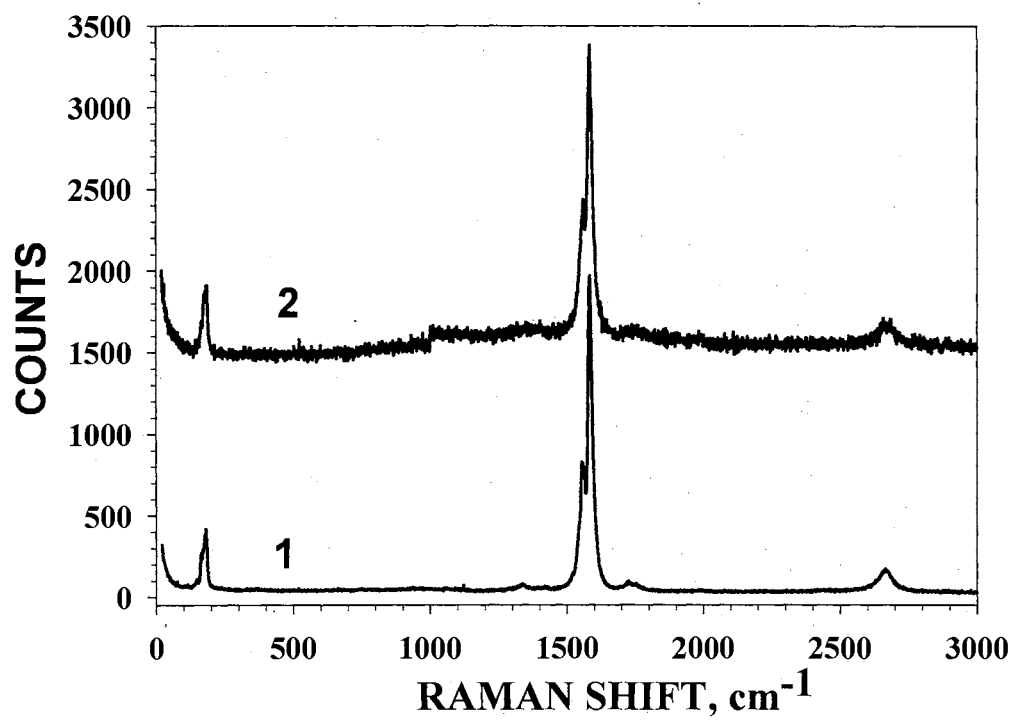
Figure 32. Raman scattering spectra of (1) SWNT dispersion and (2) LBL assembled film on a glass substrate.
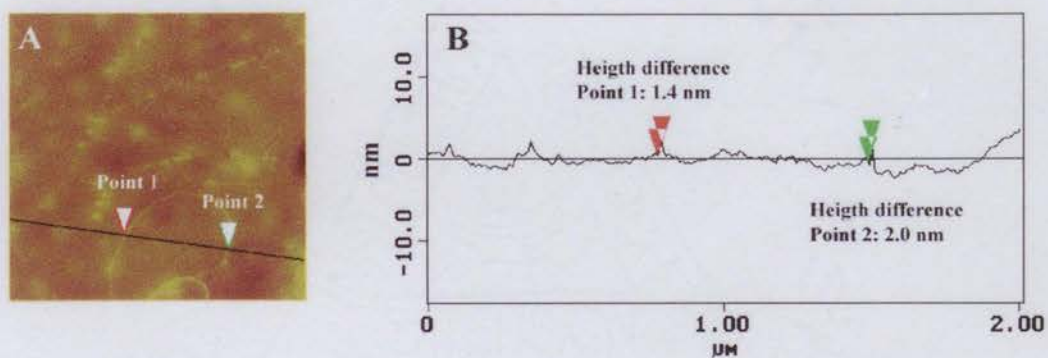
Figure 33. (A) 2 x 2 μm AFM image and (B) topography profile along the marked line with height readings for a nanotube in two points.

The presence of virtually perfect SWNT circles with diameters between 100-500 nm can be seen in the AFM images (Figure 34). Previously, such circles were observed for SWNT with chemical linked ends [12]. In combination with polyelectrolytes, the rings should be attributed to SWNT with PEI-b chains helically wrapped around them, which causes the gradual bending of the nanotube into a circle. The perfect shape of the SWNT circles also indicates the low number of structural defects in the carbon nanotube walls. Extensive wall etching would have introduced some structural disorder which would yield buckling rather than curving of the nanotubes into circles.

Resistivity of SWNT film

The resistively of the obtained SWNT films which have not been cross-linked possess a dependence on the humidity. Preliminary experiments show that at constant humidity the level of the resistivity of the film stabilizes after approximately 12-27 minutes (Figure 35). Considering this factor, samples were allowed to stabilize for 30 minutes before measuring the resistivity value at each humidity point.

The dependence of the resistivity on the humidity displayed strong hysteresis (Figure 36). The reading of the maximum resistivity at 100% humidity decreases during the first five cycles (110 KΩ for first cycle and 43 KΩ for 5th one). After the 5th cycle, the value of the resistivity at 100% humidity no longer changes. Since they are prepared from hydrophilic materials, these films can easily absorb water. Absorption of water from air, along with a loose internal structure, results in a swelling of the SWNT film. Consequently the frequency of electrical contact between the nanotubes is reduced. The
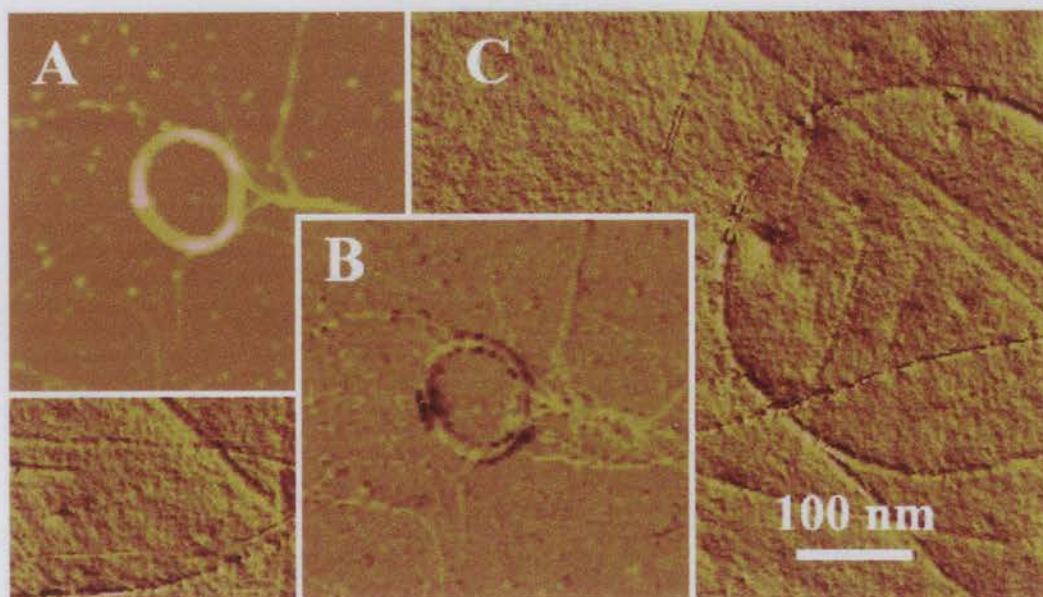
Figure 34. SWNT rings observed on height (A) and phase (B, C) AFM images of PEI-b/SWNT bilayer. Magnification factor is the same for all images.
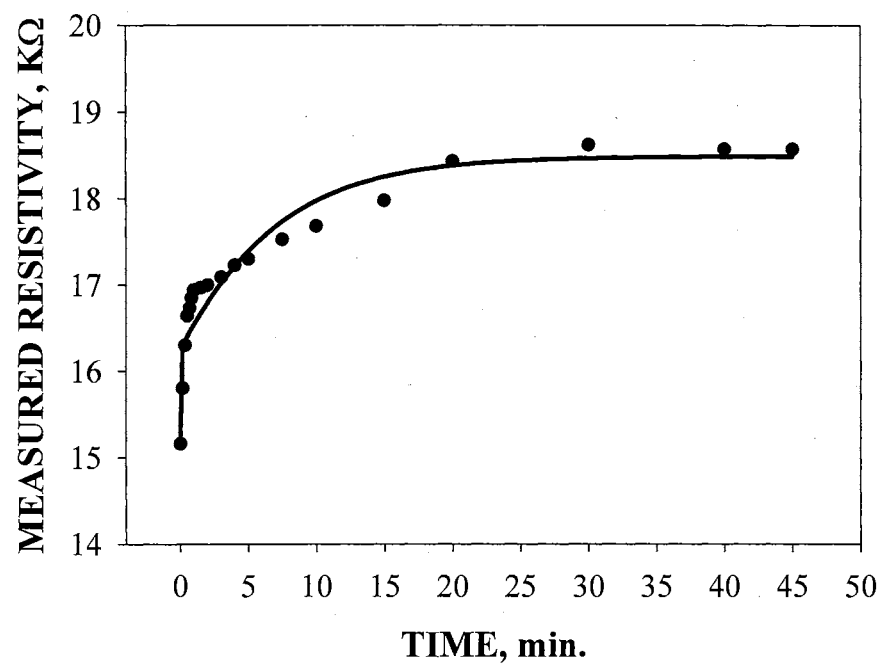
Figure 35. Dependence of resistivity of SWNT film on time. LBL assembly contained totally 30 PEI-b/SWNT bilayers. Film was dried in decicator overnight before taking any measurements.
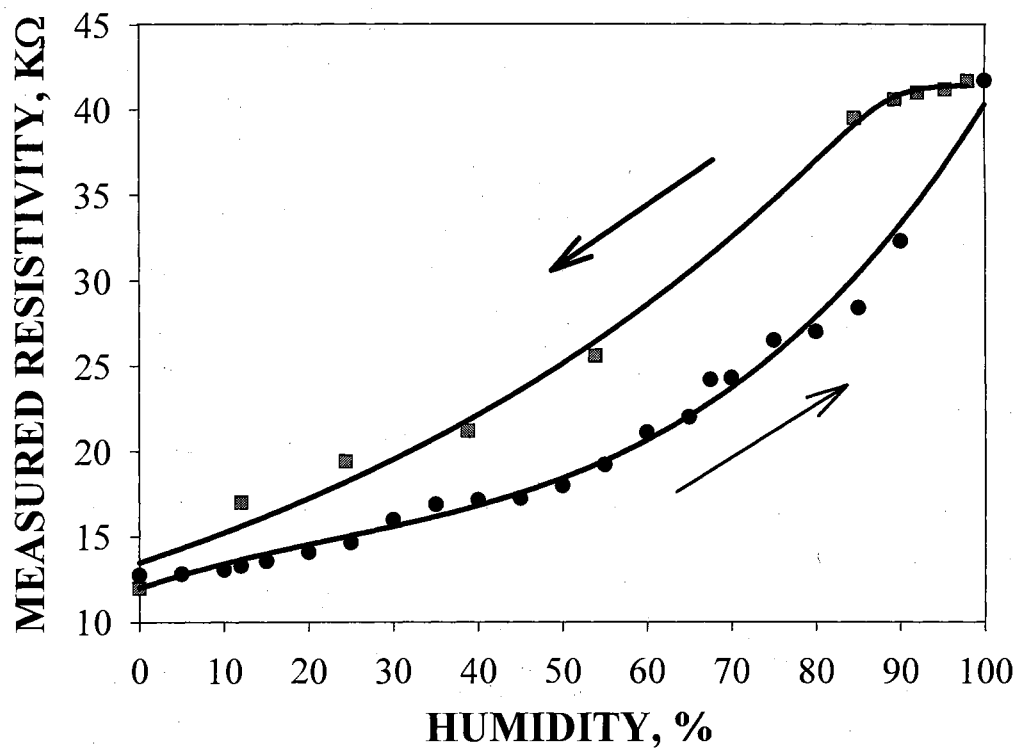
Figure 36. Reversible dependence of resistivity of the SWNT film on humidity. Arrows indicate direction of humidity change. Samples were hold for 30 minutes at each humidity level before taking measurements.

decrease of the maximum resistivity at 100% humidity during the first 5 cycles and hysteresis can be attributed to the reorganization of the SWNT in the film.

The electrical resistivity of the obtained SWNT film was calculated according to formula:

$$R = \frac{R_{exp}dw}{l}$$

It found to be equal to $1.04*10^{-2}$ Ωm at a humidity level equal to 35%. The values of electrical resistivity for selected materials are present in Table 1 [13]. Since the nanotubes inside of the film was not orient during deposition, the resistivity value of the resulting multilayers is somewhere in between resistivity values for diamond and graphite.

Alignment of SWNT during LBL deposition

The effect of the deposition conditions on the final morphology of the films was examined through alignment of the deposited SWNT. The alignment procedure was performed by utilizing a closed loop flow cell equipped with mini-pump, regulating the flow rate of the SWNT solution. The influence of the flow rate on the surface structure of the PEI-b/SWNT bilayer, which was assembled on precursor PEI-b/PAA bilayer, was our primary interest in this part of the study. Figure 37 shows AFM images of SWNT monolayers, prepared with the flow rates of SWNT dispersion equal 0 mL/min, 5 mL/min, and 9 mL/min. SWNT ring formation was not seen in the samples, prepared at conditions where the current of nanotube dispersion was present (Figure 37 B, C). This was attributed to the opening of the rings under sheer force of the liquid. In addition, it

Table 1. Electrical resistivity of selected materials

Material	Electrical resistivity, Ωm
SWNT LBL assembled film	$1.04*10^{-2}$
Carbon:	
Diamond	2.7
Graphite	$13.75*10^{-6}$
Magnetite	$52*10^{-6}$
Poly (methyl metacrylate)	$>10^{12}$
Poly (vinyl chloride)	$10^{12}-10^{14}$
Cellulose acetate sheets	$10^{8}-10^{11}$
Nylon 6	10^{10}
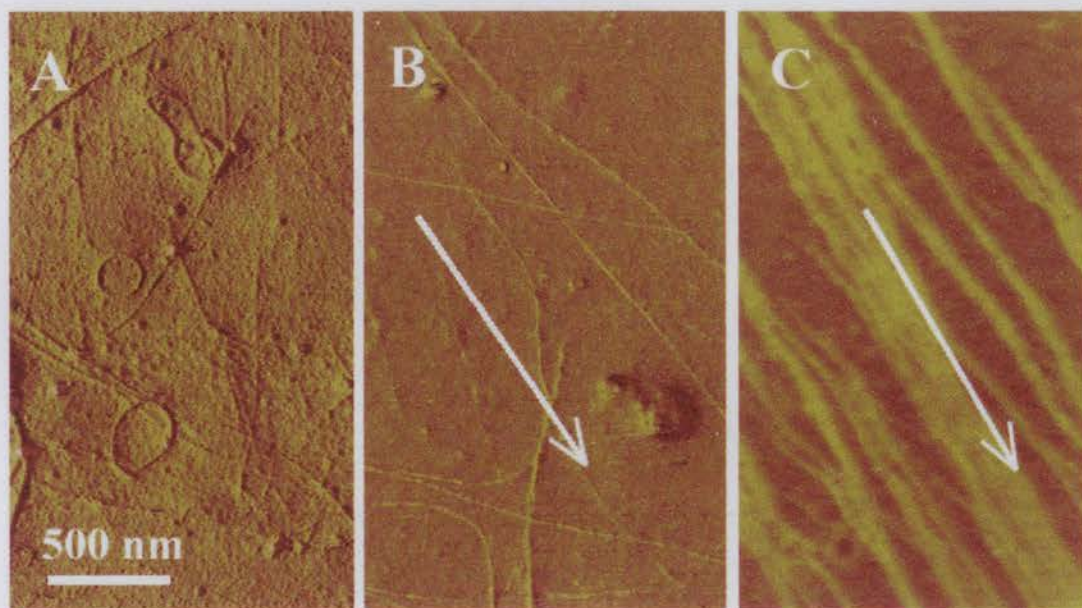
Figure 37. AFM images of SWNT films assembled in a flow cell: flow rate is equal to mL/min (A), 5 mL/min (B), and 9 mL/min (C). Arrows indicate the flow direction. Magnification factor is the same for all images.

was found that the alignment of tubes is also accompanied by their lateral assembly in ribbons (Figure 37 C). Such a morphology maximizes both the attraction to the oppositely charged substrate plane and Van-der-Waals forces between the SWNT and is similar to the macroscopic ribbon self-assembly in the liquid flow observed by Vigolo et al. [8].

Conclusion

Multilayers of SWNT can be prepared utilizing the LBL assembly method. As the organic component, PEI-b can be used. UV-vis monitoring of the process reveals a linear dependence of the optical density of the growing film on the number of deposited bilayers. The final morphology of the multilayers can be described as a dense layer of intricately intertwined individual carbon nanotubes and their bundles approximately 4-9 nm in diameter. LBL assembly minimizes the structural defects originating from phase segregation and opens the possibility for the molecular design of layered hybrid structural materials from different polymers and other nanoscale building blocks.

LBL assembled films of SWNT possess a linear dependence in their resistivity on the humidity level. This was attributed to a certain degree of flexibility inside the film. This makes it possible to utilize them as humidity detectors or some other similar devises, which require sensitivity to the moisture content in the surrounding media.

The parallel alignment of nanotubes inside of the growing film is possible upon utilizing a closed loop flow cell. The surface morphology of the aligned monolayer strongly depends on the flow rate of the SWNT dispersion. Increasing the flow rate

induces formation of nanotube ribbons along with "normal" SWNT assembly. Such morphology maximizes both the attraction to the oppositely charged substrate plane and Van-der-Waals forces between SWNT. Preparation of the multilayer stack of aligned SWNT may result in a new material with mechanical and electrical properties which differ along all 3 dimensions.

References

1. Ouyang, M.; Huang, J. L.; Cheung, C. L.; Lieber, C. M. *Science* **2001**, *292*(5517), 702-705.

2. Bachtold, A.; Hadley, P.; Nakanishi, T.; Dekker, C. *Science* **2001**, *294*(5545), 1317-1320.

3. Derycke, V.; Martel, R.; Appenzeller, J.; Avouris, P. *Nano Letters* **2001**, *1*(9), 453-456.

4. Collins, P. G.; Arnold, M. S.; Avouris, P. *Science* **2001**, *292*(5517), 706-709.

5. Ago, H.; Petritsch, K.; Shaffer, M. S. P.; Windle, A. H.; Friend, R. H. *Advanced Materials* **1999**, *11*(15), 1281-1285.

6. Haggenmueller, R.; Gommans, H. H.; Rinzler, A. G.; Fischer, J. E.; Winey, K. I. *Chemical Physics Letters* **2000**, *330*(3,4), 219-225.

7. Poa, C. H.; Silva, S. R. P.; Watts, P. C. P.; Hsu, W. K.; Kroto, H. W.; Walton, D. R. M. *Applied Physics Letters* **2002**, *80*(17), 3189-3191.

8. Vigolo, B.; Penicaud, A.; Coulon, C.; Sauder, C.; Pailler, R.; Journet, C.; Bernier, P.; Poulin, P. *Science* **2000**, *290*(5495), 1331-1334.

9. Salvetat, J. P.; Briggs, G. A.; Bonard, J. M.; Bacsa, R. R.; Kulik, A. J.; Stockli, T.; Burnham, N. A.; Forro, L. *Physical Review Letters* **1999**, *82*(5), 944-947.

10. Mawhinney, D. B.; Naumenko, V.; Kuznetsova, A.; Yates, J. T.; Liu, J.; Smalley, R. E. *Chemical Physics Letters* **2000**, *324*(1,2,3), 213-216.

11. Rols, S.; Righi, A.; Alvarez, L.; Anglaret, E.; Almairac, R.; Journet, C.; Bernier, P.; Sauvajol, J. L.; Benito, A. M.; Maser, W. K.; Munoz, E.; Martinez, M. T.; De la

Fuente, G. F.; Girard, A.; Ameline, J. C. *European Physical Journal B: Condensed Matter Physics* **2000,** *18*(2), 201-205.

12. Sano, M.; Kamino, A.; Okamura, J.; Shinkai, S. *Science* **2001** *293*(5533), 1299-1301.

13. CRC Materials Science and Engineering Handbook. *CRC*, Boca Raton, FL **(1992)**.

CHAPTER V

FREE-STANDING FILMS OF

LAYER-BY-LAYER ASSEMBLED NANOCOLLOIDS[i]

Introduction

It was shown in the previous chapters, that layer-by-layer (LBL) assembly method can be applied to the variety of inorganic compounds including nanoparticles (NP) and single wall carbon nanotubes (SWNT). After successful deposition of such compounds into multilayers onto the substrate it was logical to make step further and prepare free-standing membranes. Films without a substrate allow for the direct experimental determination of many physical properties of the LBL films such as ion permeation and chain packing, which are being actively discussed in the literature with little or no quantitative data [1-5]. In addition to that, they will open the door for the preparation of a variety of membranes with the possible applications of which range from the advanced catalytic materials to the artificial biological membranes. The large number of materials which can be utilized in LBL method will lead to the rich palette of mechanical, chemical, optical, magnetic *etc.* properties in such membranes. Most important, the layer-

---

[i] Portions of this chapter have been previously reported in: Mamedov, A. A.; Kotov, N. A.; Prato, M.; Guldi, D. M.; Wicksted, J.P.; Hirsch, A. *Nature Materials* **2002**, *1*, 190-194. Mamedov, A. A.; Kotov, N. A. *Langmuir* **2000**, *16*(13), 5530-5533..

by-layer method of formation of these membranes affords the degree of the structural organization, which hard to achieve by traditional methods of membrane preparation.

When one tries to prepare free-standing films, the choice of substrate for the LBL assembly becomes challenging. Even though the LBL assembly process can be carried under the correct conditions almost endlessly, most of the LBL assemblies do not exceed a thickness of 1 micron. Such films can not be removed mechanically from the substrate without physical damage due to a strong linkage between the LBL stack and the substrate. On the other hand, for successful LBL growth strong interactions between substrate and first assembled layer are needed. This problem can be overcome when a way to disrupt the interactions between the substrate and the LBL assembled multilayers is found.

The study described in this chapter presents methods for the preparation of free-standing LBL assembled films. Films of magnetic and semiconductor NP, sodium montmorillonite, and SWNT, the assembly conditions of which were discussed in the previous chapters, were chosen to test these methods. The introduction of alumosilicate clay (C) sheets, which cover large areas of the substrate surface, helps to obtain separation between the separate bilayers of the membrane as it was shown in Chapter II. In addition, C layers reduce the roughness of the film and improve the linearity of the LBL process by covering large areas of the growing surface. These interlayers of C or other materials may serve as a molecular armor, increasing the mechanical strength of the free-standing films. Variation of internal structure was accomplished by introduction of interlayers of C and poly(acrylic acid) (PAA). The effect of this variation on the structure and additional cross-linking of the resulting free-standing films on their mechanical

properties will be demonstrated. The possibility of the utilization of several different substrates and the conditions for their practical use will also be discussed.

Experimental Procedures

Materials

Poly(dimethyldiallylammonium chloride) (PDDA, Mw = 200,000 – 350,000; 20 % wt. in water), PAA (Mw = 450,000) used in LBL assembly, metallic Ga (99.99%), and acetone (99.5+ %) were bought from Aldrich (Milwaukee, WI). Cellulose acetate (CA) sheets (25 μm thick), sulfuric acid (H_2SO_4), and hydrofluoric acid (HF) were obtained from EM Science (Gibbstown, NJ). Sodium montmorillonite (alumosilicate clay material – clay, C), utilized in LBL assembly process, has been received from Source Clay Minerals Repository, University of Missouri-Columbia (Columbia, MO). LR-white embedding resin, used for TEM sample preparation was obtained from the London Resin Company *Ltd*. (Berkshire, England). All chemicals were used without further purification. De-ionized water (> 18.0 MΩ-cm, Barnstead, E-pure system), with an unadjusted pH of approximately 5.5, was used exclusively in all solutions and rinsing procedures.

Preparation of free-standing films

The principle of making free-standing LBL assembled films is shown in Figure 38. Initially, the LBL deposition process is carried out on a solid substrate. When a degree of structural sophistication and/or a desirable thickness is achieved, the prepared
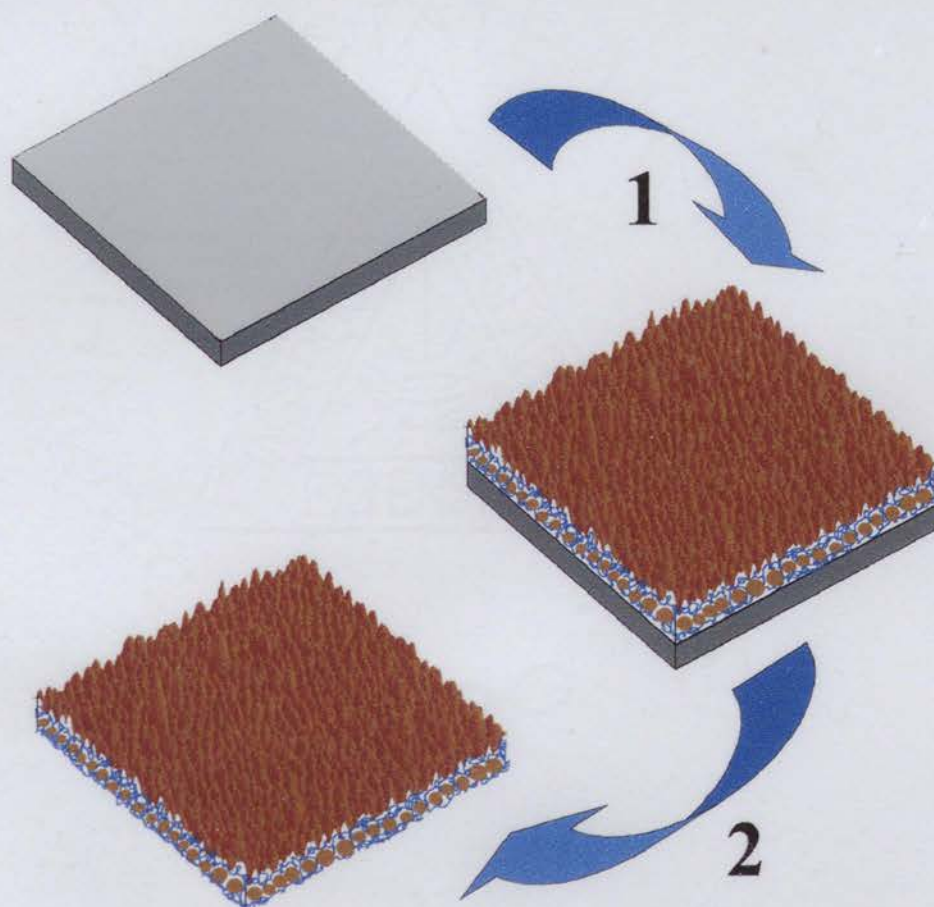
Figure 38. Idea of free-standing films preparation. (1) LBL assembly of film on solid strate. (2) Removal of obtained film of desirable thickness and/or degree of structural anization.

LBL assembly is lifted off by either destroying the substrate by dissolving it a suitable organic solvent or by breaking the bonds between the substrate and the film. To some extent, the idea of the preparation of free-standing films resembles the preparation of polyelectrolyte microcapsules by burning or dissolving the micrometer scale colloids [1,2].

Substrates for free-standing films preparation

The assemble-and-destroy principle imposes two major requirements on the substrate: (1) the organic solvents used in the lift-off step must not damage the film and (2) the substrate must be hydrophilic with a positively or negatively charged surface. The latter will promote an electrostatic attraction between the substrate and the first layer of polyelectrolyte, serving as the film foundation. These requirements are satisfied by cellulose acetate (CA) films, metallic gallium films (Ga-film), and silicon wafers or glass slides. Based on the substrate used for LBL deposition of the films, three methods has been used.

Method 1. Cellulose acetate is insoluble in water, but it can easily be dissolved in acetone at room temperature. The surface of CA is fairly hydrophilic with contact angles of 50-55°. This substrate can be used for the preparation of a wide range of films. However, it also has some limitations. Acetone is not biocompatible with a number of biological materials, which makes the possibility of preparation of free-standing films of proteins problematic. In addition, when a porous film is prepared utilizing this method, dissolved CA penetrates into the pores and it becomes difficult and time consuming to completely wash it out of the film.

Method 2. Gallium is a fairly inert metal, which does not react with inorganic nanomaterials or polymers. It has a melting point of 29.78°C. The roughness and some hydrophobicity of the surface can easily be mediated by adsorbing of 1 – 5 multilayers of PDDA/PAA (precursor layers). A free-standing film can be prepared by heating the substrate bearing the LBL assembled film over 30°C. Such moderate heating conditions allow utilization of this substrate for free-standing films based on biological materials.

Method 3. Silicon wafers and glass slides are the most common substrates used for the LBL process. They have some negative surface charge in aqueous solutions which comes about from the ionization of the Si-OH surface groups. The assembly of the first polymer monolayer can be enhanced by the deposition of it from a solution with a basic pH. The LBL multilayers of desired thickness and structural organization can be removed by a short treatment with a 0.5% aqueous solution of HF. This dissolves the thin oxide film of silica between the LBL assembly and the substrate, releasing a freely floating self-supporting membrane.

Preparation of free-standing magnetite and CdTe films

The layer-by-layer deposition of magnetite (M) or CdTe nanoparticles was carried out on a cellulose acetate substrate according to the procedures described in Chapters II and III. To facilitate the lift-off of the LBL assembly and the realization of the dipping cycle, the CA was supported by a glass slide. After depositing an appropriate number of PE/NP bilayers followed by thorough drying, the thin CA-coating with the LBL film was peeled off of the glass support and immersed in acetone for 24 hours. The CA substrate was dissolved away leaving brown colored films freely suspended in the solution, which

were transferred into a new portion of acetone to completely wash away any remaining CA.

In addition to "plain" PE/NP films, samples with every other nanoparticle layer replaced by a layer of clay platelets have been prepared. Figure 39 represents a model of the structures of the obtained "plain" and clay substituted films. The repeating unit of each film is denoted as (PE/NP) and (PE/C/PE/NP) respectively. N is the number of repeating units deposited before the desired thickness and structural organization of the films were obtained.

Preparation of free-standing clay films

Sodium montmorillonite (clay) platelets were LBL assembled with PDDA on glass slides, silicon wafers and metallic Ga substrates. The glass slides and silicon wafers were cleaned with a piranha solution (a mixture of 30% H_2O_2 and concentrated H_2SO_4 in a 1:3 ratio), followed by a rinsing with DI water, then sonicated for 15 minutes and finally rinsed again with DI water. Ga substrates were prepared by solidifying the melted metal in the shape of a 2 cm X 2 cm square with 0.5 cm thickness. A saturated clay solution was prepared by the sonication of a C dispersion in DI water for 30 minutes followed by centrifugation for 10 minutes. The supernatant, containing exfoliated clay platelets was used for the LBL assembly. A precursor PDDA/PAA bilayer was deposited before the assembling of the C multilayers. An 1% aqueous solutions of both polymers were used. The pH of the PDDA solution was adjusted to 9.0 using 0.1 M NaOH. A solution of PAA was used as received with a pH approximately 3.1. The deposition times for the PDDA and PAA monolayers were 15 and 10 minutes respectively.
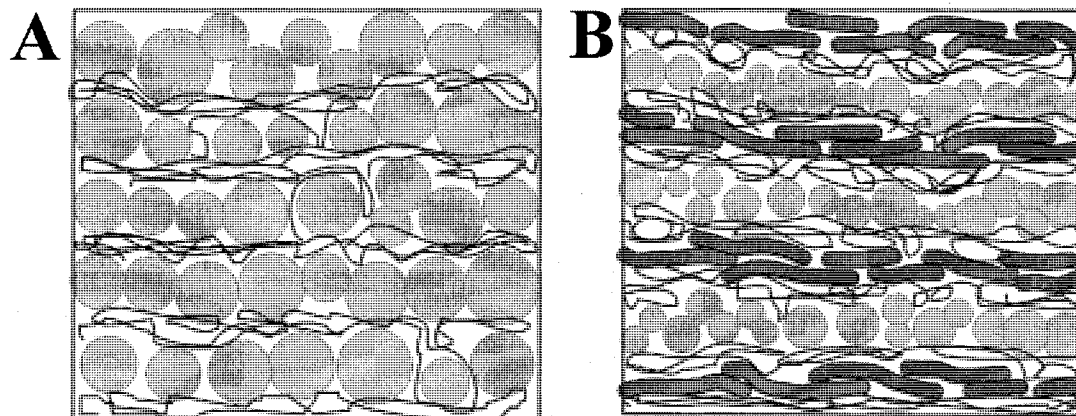
Figure 39. Model structures of (A) "plain" (PE/NP)$_N$ and (B) clay substituted (PE/C/PE/NP)$_N$ multilayers. N is the number of repeating units deposited before desirable thickness and structural organization of films was obtained. Drawn not to scale.

A typical deposition cycle for a multilayer stack consisted of the following steps: (1) adsorption of PDDA from a 1% aqueous solution for 10 minutes, (2) 3 rinses with DI water, (3) adsorption of a C layer from a saturated solution for 10 minutes, and (4) 3 rinses with DI water. Upon finishing the LBL assembly process, the obtained clay multilayers were air dried.

To remove the PDDA/C film from the glass or silicon substrate, it was immersed into a 0.5% aqueous solution of HF for 30 seconds. The LBL assembly was immediately removed from the substrate and rinsed with DI water followed by air-drying.

The film assembled on a Ga-substrate was removed by placing it into beaker containing DI water and heated in a water bath up to 35°C. After the melting of the substrate, a free-standing film was obtained and transferred into fresh warm DI water to remove any remaining Ga. Upon finishing the washing procedure, the film was air-dried.

Preparation of free-standing SWNT films

LBL deposition of SWNT film was carried out on a glass slide according to the technique described in Chapter IV. PEI-b chains, used as an organic component in the LBL assembly process, can be cross-linked (1) with each other and (2) with carboxyl groups on SWNT and PAA. Both types of cross-linking have been used for the preparation of SWNT free-standing films.

The covalent SWNT-PEI-PAA cross-linking was easily achieved by heating the films to 100°C after the deposition of each layer. This resulted in amidation of the amino groups of PEI-b by carboxyls of SWNT [6]. After the preparation of a complete multilayer stack, the film was cross-linked with gluteraldehyde (GA) [7] forming

covalent bonds with the amino groups of PEI-b. This was carried out in a 0.5% aqueous solution (pH 7.4) of GA for 1 hour at room temperature. To remove any unreacted GA, the film was rinsed with DI water 3 times for 10 minutes each.

Upon the finishing cross-linking procedure, a glass substrate with a LBL assembled SWNT film was immersed into a 0.5% aqueous HF solution for 3 minutes. The obtained free-standing film was rinsed with DI water and then air-dried.

X-ray photoelectron spectroscopy

X-ray photoelectron spectra (XPS) were recorded at a takeoff angle of 0° using a system EscaLab 220-IXL. The Kr X-ray line of Al at the spectrometer pass energy of 1486.92eVand step resolution of 0.1 eV was used as the source.

Tensile stress measurements

The mechanical properties of the free-standing SWNT films were tested on a custom-made thin film tensile strength tester (McAllister Inc.) which recorded at the displacement and applied force by using pieces cut from $((PEI-b/PAA)(PEI-b/SWNT)_5)_6$ and $((PEI-b/PAA)(PEI-b/SWNT)_5)_8$ films. The tester was calibrated on similar pieces made from cellulose acetate membranes and Nylon threads. The average thickness of the $((PEI-b/PAA)(PEI/SWNT)_5)_6$ and $((PEI-b/PAA)(PEI-b/SWNT)_5)_8$ samples was determined by TEM and was estimated to be 0.75 and 1.0 microns respectively.

Results and Discussion

Free-standing magnetite films

Cellulose acetate was chosen as the substrate for magnetite free-standing films preparation. One dipping sequence in LBL assembly resulted in the addition of a PDDA/M bilayer with an average thickness of 8 ± 0.5 nm as it was determined by ellipsometry. AFM investigation of one (PDDA/M) bilayer revealed that such a film was made of densely packed nanoparticles (Figure 40 A). When an appropriate number of PDDA/magnetite (M) bilayers were deposited, the CA substrate was dissolved and all traces of it were washed out according to the procedure described in the experimental section. This procedure yielded a dark colored film freely suspended in the solution (Figure 41). As expected, the obtained thin film retained the magnetic properties of nanoparticles: it moved through the solution toward a permanent magnet placed near the side of the beaker. From the suspended state, the films could be transferred onto any solid or porous substrate. However, they were quite fragile, which was not surprising considering that the thickness of the films, such as (PDDA/M)$_{15}$ and (PDDA/M)$_{30}$, was in the range of a few hundred nanometers. The magnetization curve of the obtained magnetite film (Figure 42) had a characteristic sigmoidal shape with a very small hysteresis loop in the low field region.

It was demonstrated in previous chapters that LBL assembly allows for manipulation in the order of the deposited layers. To strengthen the magnetite films every other layer of magnetite was replaced with a layer of exfoliated clay platelets, producing an assembly with a (PDDA/C/PDDA/M)$_n$ sequence (Figure 39 B). C platelets have a
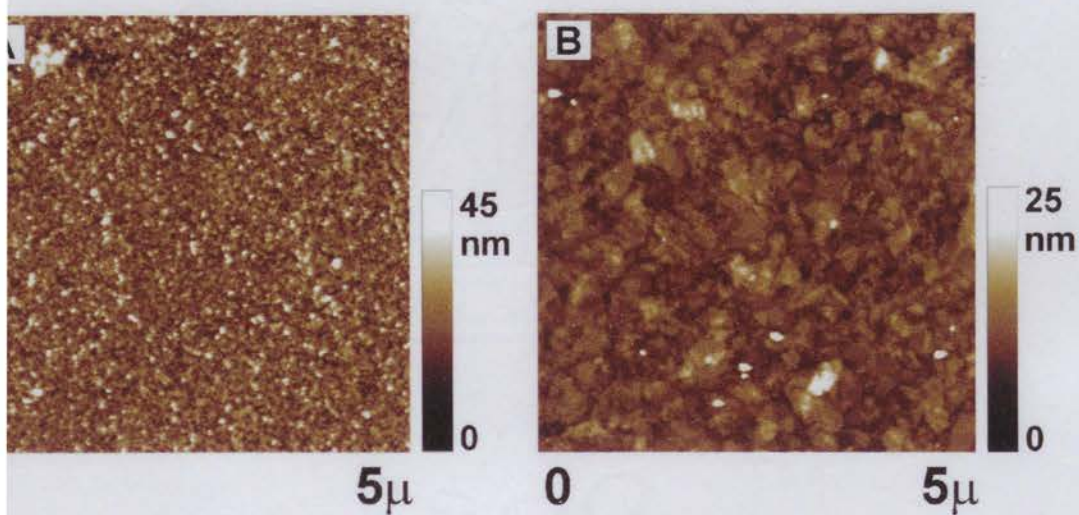
re 40. AFM images of one bilayer of magnetite (A) and clay (B) on silicon wafers. -grain texture of the left image is characteristic for the magnetite film. Each light dot sents a 2D cluster of 8-10 nm Fe_3O_4 nanoparticles. The montmorillonite adsorption in image B was shortened from 1 minute, which was typically used for making the , to 25 s to better reveal the shape and size of the platelets.

Figure 41. Optical image of (PDDA/M)$_{30}$ free-standing film, freely floating in DI water.
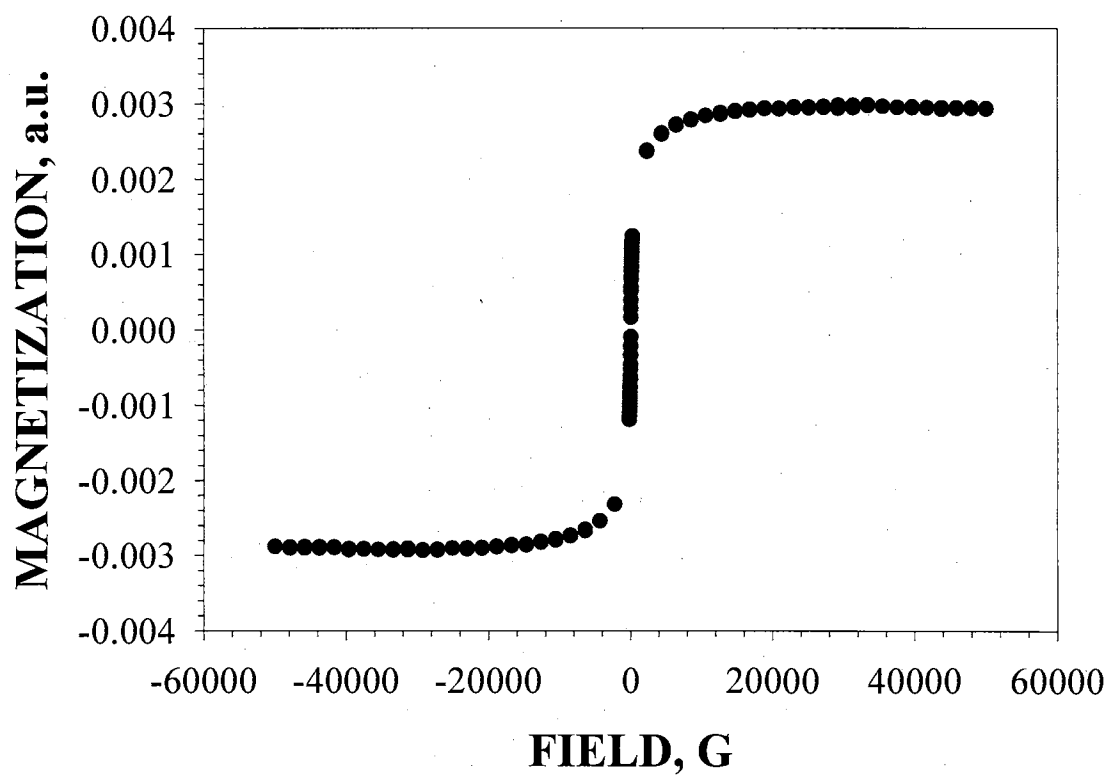
Figure 42. Magnetization curve obtained for 0.5 ± 0.5 cm piece of $(PDDA/M)_{30}$ film taken at $T = 298$ K.

thickness of about 1.0 nm, while extending 150-300 nm in the other dimensions. On polyelectrolytes, they formed a layer of overlapping alumosilicate sheets (Figure 40 B) with an average thickness of 3.8 ± 0.3 nm [5,8]. Being adsorbed virtually parallel to the surface of the substrate, their large size allows them to cover approximately 400 nanoparticles at once, which adds additional strength to the assembly. A free-standing film, consisting of 30 (PDDA/C/PDDA/M) units could easily be picked up with tweezers, transferred, cut, moved around the solid surface, and handled in any other way. Taking an advantage of this architecture, it was possible to make a free-standing film with as few as eight repeating (PDDA/C/PDDA/M) units, which could not be possible without an alumosilicate framework.

In characterization of the free-standing films it was important to establish the identity of both surfaces of the film and to ensure complete CA removal, which may have contributed to strength of LBL free-standing stack. The SEM and XPS data taken on the sides that were facing the solution (top) and CA (bottom) during the deposition revealed complete identity of their surfaces (Figure 43). In particular, observation of the Fe 2p1 and Fe 3p3 peaks (at 1211 and 1198 eV, respectively) would have been impossible on the CA part of the film if a CA film of even a few nanometers in thickness was present. The identical ratio of the intensity of the iron peaks to the intensity of carbon 1s peak clearly indicates the completeness of CA removal, which proves that a self-supporting nature of the film was obtained.

To estimate the thickness of the prepared free-standing films, they were embedded and cross sectioned according the procedure, described in Chapter III. The resulting 50-200 nm thick cross-sections were investigated by optical and transmission

Figure 43. (A and B) XPS spectra of top (A) and bottom (B) surfaces of (PDDA/C/PDDA/M)$_{30}$ film. In the inserts, the 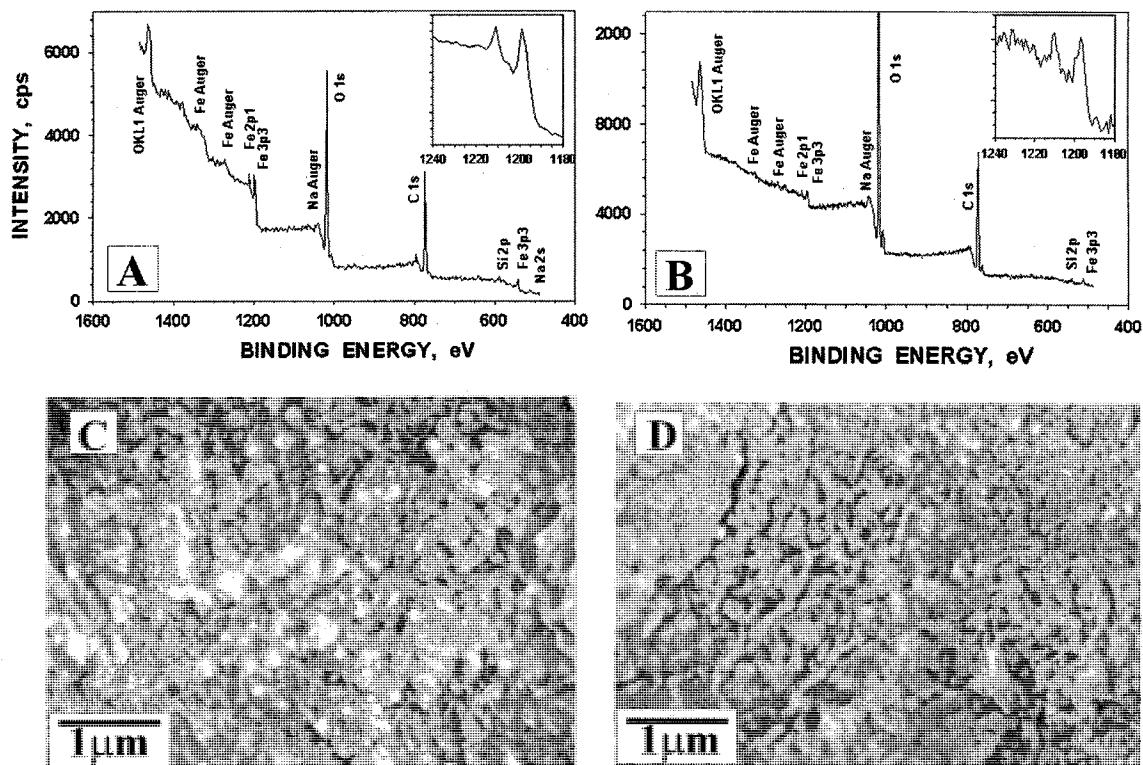enlarged portions of the spectrum with 2p1 and 3p3 peaks of surface Fe atoms are given. (C and D) SEM images of top (C) and bottom (D) surfaces of the same film.

electron microscopy. Two continuous black bands of uniform thickness of the (PDDA/C/PDDA/M)$_{30}$ film can clearly be seen in the optical microscope image (Figure 44 A). Due to folding of magnetite free-standing film in horse-shoe shape, two cross-sections of the same film present in one section. Because of light aberrations on the objects comparable to the wavelength of light, the actual thickness was determined from an electron microscopy image (Figure 44 B, C) and was found to be 350 ± 30 nm. This parameter was also estimated by adding up the thicknesses of the PDDA/M and PDDA/C bilayers. For the (PDDA/C/PDDA/M)$_{30}$ film, this gives (3.8 + 8.0) x 30 = 354 nm, which coincides well with the TEM measurements.

The analyzed films were very homogeneous with no apparent phase boundaries between the components. Their particulate nature can be seen especially in the 25 nm thick cross sections, shown in Figure 44 C. In addition, formation of longitudinal cracks, originating from the cross sectioning procedure, was observed (Figures 44 B). TEM study of the cross-sections of the "plain" (PDDA/M)$_{30}$ film did not reveal any anisotropy in their physical damage caused by the diamond knife (Figure 45). Such anisotropy for clay containing free-standing films can be attributed to the existence of montmorillonite stacks with sheets oriented in a parallel fashion to each other.

Free-standing CdTe films

To confirm the universality of the cellulose acetate method, CdTe free-standing films were prepared. CdTe nanoparticles, stabilized with thioglycolic acid, show a strong size-dependent exitonic luminescence (up to 20% quantum efficiency at room temperature). Additionally, the luminescence of CdTe can be damaged by acidic media
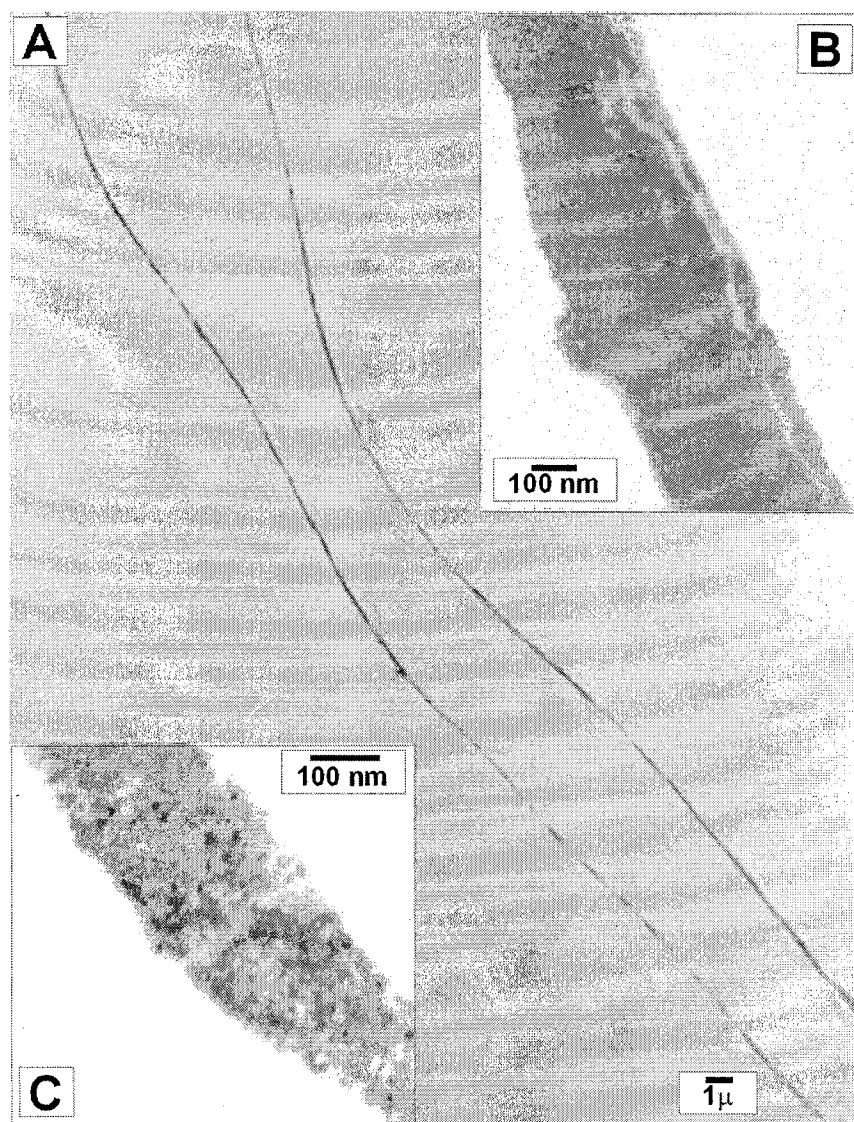
Figure 44. (A) Optical micrograph of the (PDDA/C/PDDA/M)$_{30}$ cross section. Two strands of the film can be seen; because some parts of the film were folded during imbedding in epoxy resin. (B and C) TEM micrographs, respectively) of (PDDA/C/PDDA/M)$_{30}$ cross sections.
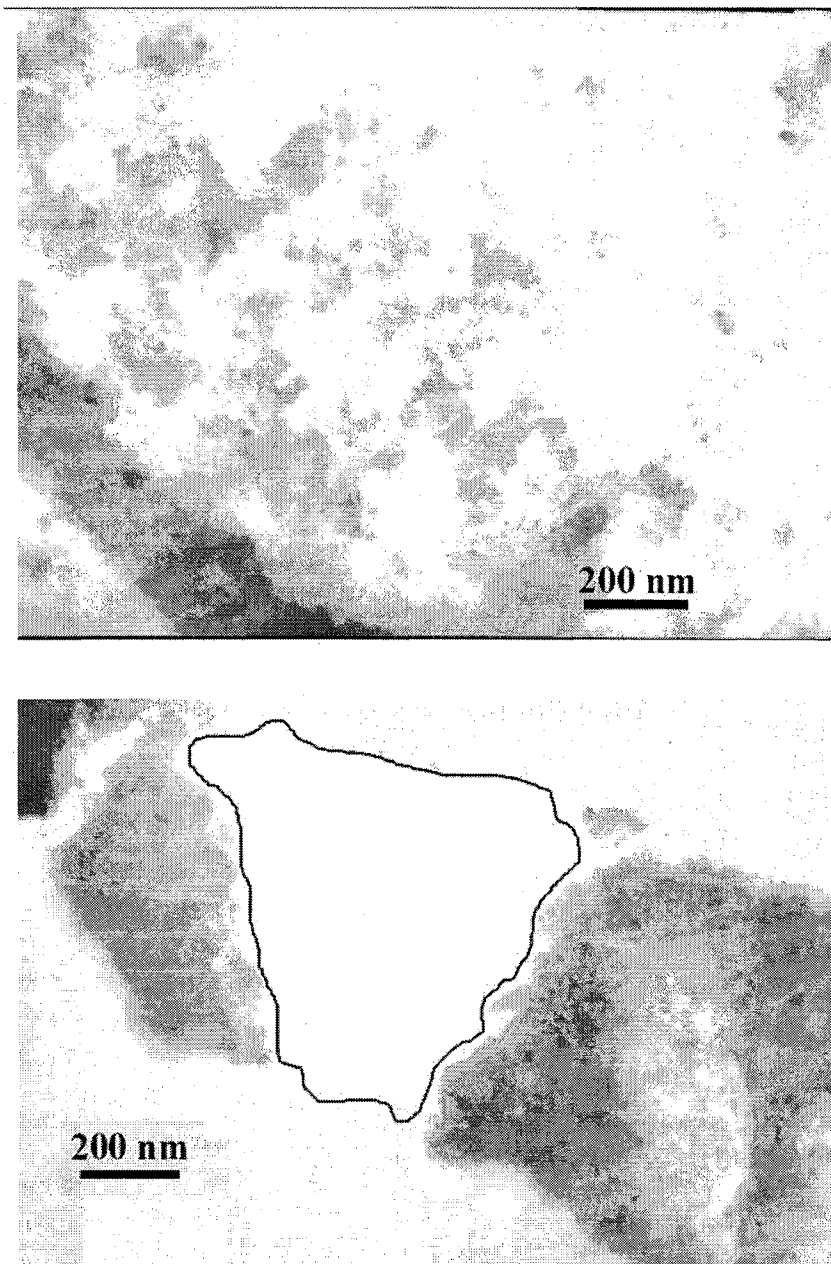
Figure 45. TEM micrographs of $(PDDA/M)_{30}$ cross sections. No anisotropy in physical damage, caused by diamond knife during cross-sectioning can bee seen. Marked area shows hole from fallen piece of magnetite film.

139

when HF used for this purpose (see Method 3). Multilayers of "green" (2-3 nm in diameter) and "red" (5-6 nm diameter) CdTe have been assembled on a cellulose acetate substrate. After removal of the substrate and thorough washing, free-standing films of CdTe nanoparticles have been prepared (Figure 46 A, B). Both films appeared to be yellow in color under daylight. However, upon illumination with a mercury UV lamp, they emitted green or red light depending on the size of the NP. This points out that, as in case of magnetic nanoparticles, the CdTe free-standing films retained the properties of the NP used for LBL assembly. Complete removal of CA substrate was confirmed by the identity of the intensity of the cadmium peaks referenced to the intensity of the carbon 1s peak (Figure 46 C, D).

The internal structure of "plain" $(PDDA/CdTe)_N$ vas varied by adsorption of PDDA/C interlayers after each PDDA/CdTe bilayer. In addition to that, it was also varied by absorption of a PDDA/PAA interlayer after depositing each $(PDDA/CdTe)_5$ unit during the LBL growth. Samples assembled on a precursor layer of PDDA/PAA with an internal structure of $(PDDA/PAA)(PDDA/CdTe)_{20}$ and $[(PDDA/PAA)(PDDA/CdTe)_5]_4$, contained 20 PDDA/CdTe bilayers each, and $(PDDA/PAA)(PDDA/C/PDDA/CdTe)_{10}$, contained 10 PDDA/CdTe bilayers, have been embedded into an epoxy resin and cross-sectioned. TEM study (Figure 47) of ~25 nm cross-sections revealed the alternating structure of the film containing extra interlayers of PDDA/PAA (Figure 47 B). It can be noted that 4 additional bilayers PDDA/PAA increase the thickness of the film by a factor of $1.5 - 2$. This is probably due to the fact that the assembly of PAA was performed from
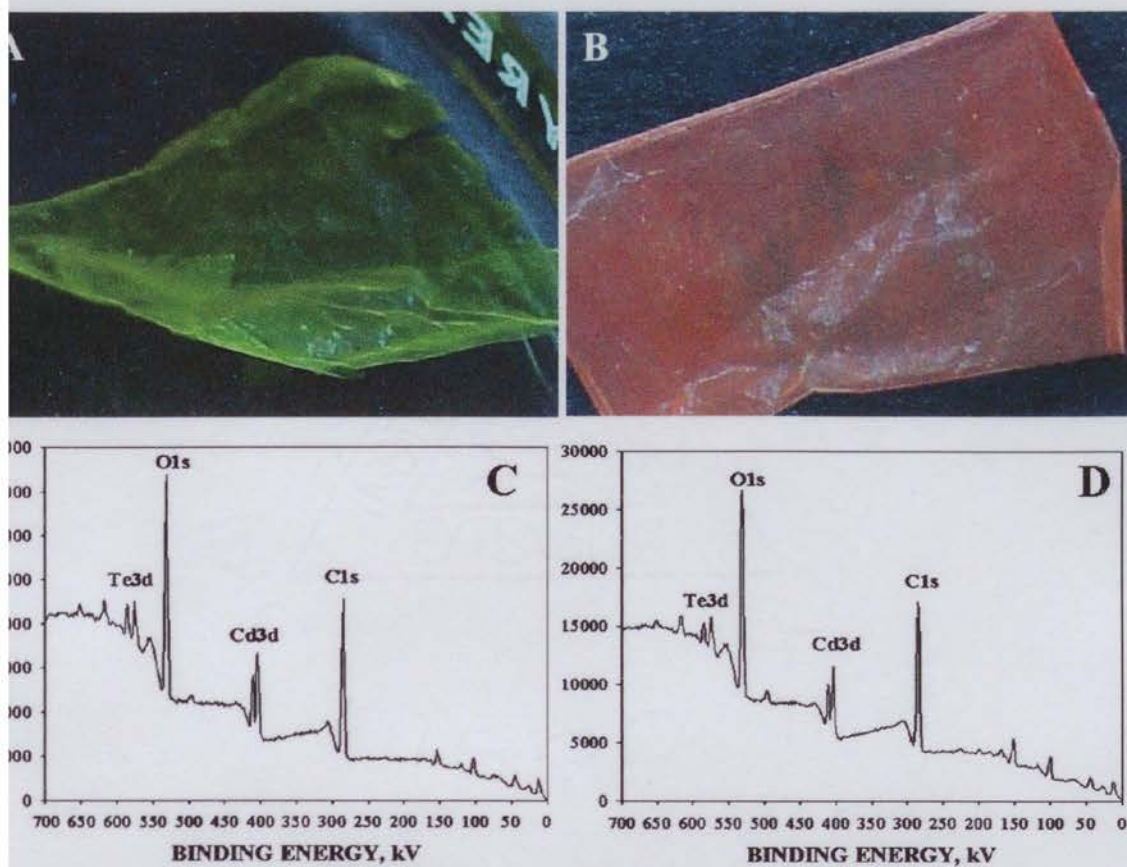
Figure 46. (A, B) Free-standing films made with "green" (A) and "red" CdTe nanoparticles. (C, D) XPS spectra of top (C) and bottom (D) surfaces of CdTe free-standing film, made from "red" CdTe nanoparticles.
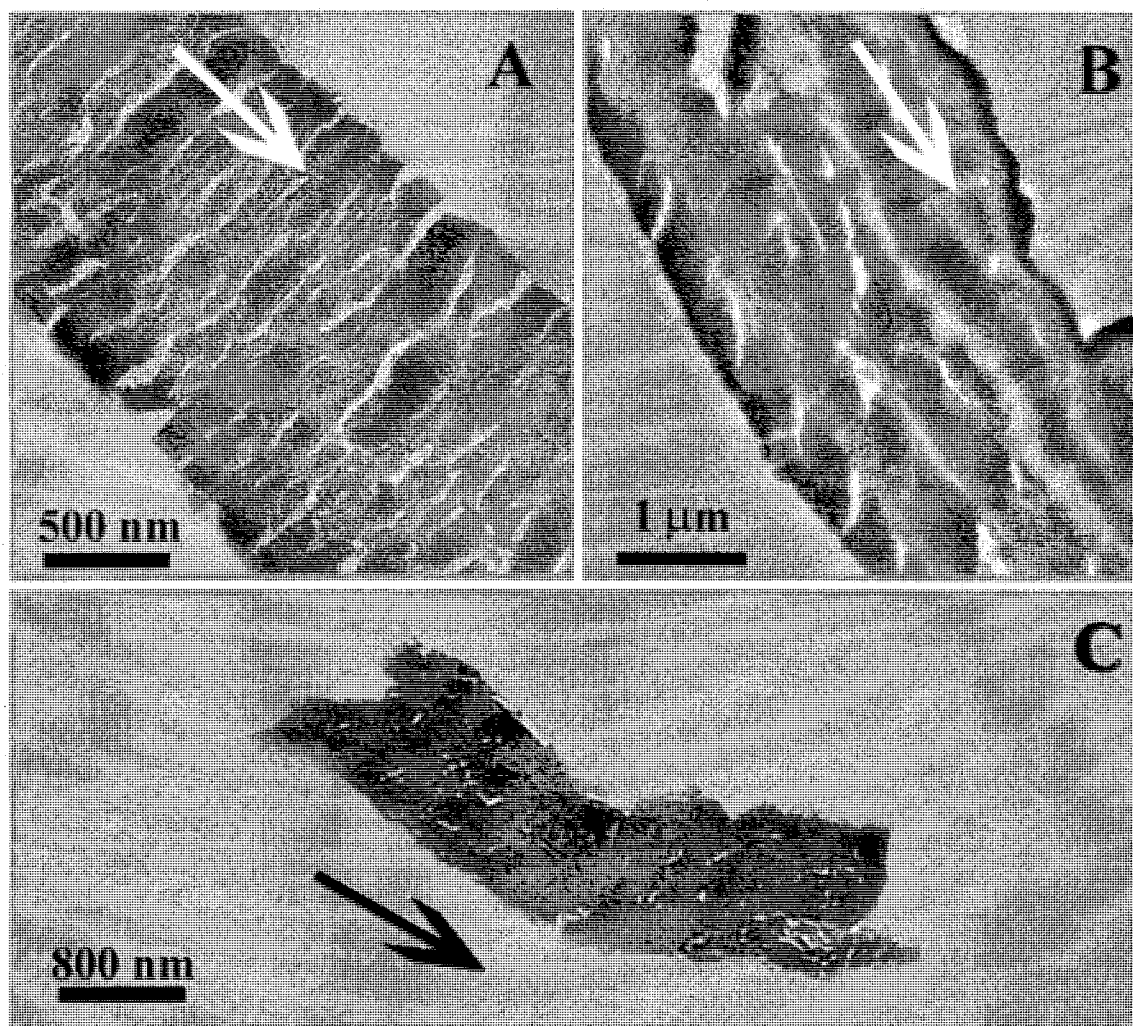
Figure 47. TEM images of cross-sections of CdTe free-standing films, bearing structures of (A) (PDDA/PAA)(PDDA/CdTe)$_{20}$, (B) [(PDDA/PAA)(PDDA/CdTe)$_5$]$_4$, and (C) (PDDA/PAA)(PDDA/C/PDDA/CdTe)$_{10}$. Arrows indicate direction of sectioning.

a 1% aqueous solution (pH = 2.5) of very high molecular weight (750,000). Such conditions of assembly result in the formation of a thick PAA monolayer (Chapter I, Figure 4 D). The formation of cracks perpendicular to the film surface for the "plain" PDDA/CdTe film (Figure 47 A) is probably due to curling of thin slice during cross-sectioning. The presence of PDDA/PAA interlayers straightens the structure and results in the formation of angular cracks inside of each (PDDA/CdTe)$_5$ unit (Figure 47 B). Free-standing films in which every other CdTe layer was substituted with a layer of clay possess higher strength against physical damage from diamond knife and shows no pattern in the formation of the cracks during cross-sectioning procedure (Figure 47 C).

Influence of the substrate on structure of free-standing film

The utilization of cellulose acetate as a substrate allows for the preparation of a wide variety of free-standing films from different materials. However, there are a number of cases when a CA substrate is not suitable. The most obvious one is in the case of biological materials. For example, treatment with acetone results in a dehydration of protein based LBL assembled multilayers. As it was already mentioned, the CA method of preparation of free-standing films becomes difficult and time consuming when highly porous membranes are prepared.

As an alternative to the CA method, two other substrates have been tested: metallic gallium and glass slides or silica wafers. Free-standing films prepared on metallic Ga substrate, which has a low melting point (29.78°C), were obtained by simply heating the sample to a temperature above 30°C. When glass slides or silicon wafers were

used, treatment with a 0.5% solution of HF for 30 seconds was enough to destroy the thin SiO$_2$ layer between substrate and assembled film resulting in a free-standing material.

(PDDA/C)$_{100}$ free-standing films, prepared by both methods, have been embedded into epoxy resin and cross-sectioned. TEM micrographs of these cross-sections are presented in Figure 48. Complete removal of Ga substrate is clearly seen on the micrograph (Figure 48 A). Even though both films are porous, the film, prepared on the glass slide, possess a much higher porosity level (Figure 48 B). Such a difference cannot be attributed to a variation in the preparation procedure. It can be noted that the average thicknesses of both films are close ($\sim$ 1 μm). Furthermore, most of the pores in the films are filled with the embedding resin, which indicates that pores were formed prior embedding procedure and do not originate from the cross-sectional damage.

To understand the reasons behind the difference in the porosity of the films, AFM images of one bilayer (PDDA/C) were taken before and after the treatment with HF (Figure 49 A, B). The sample was treated with the exact conditions required for free-standing film preparation. It was found that such treatment does not introduce additional pores into the bilayer. From section analysis data (Figure 49 C, D) it can be clearly seen that the thickness of clay platelets decreases from 7 nm to 5 nm and their linear dimensions decrease from 193 nm to 152 nm. This means that treatment with a 0.5 % aqueous solution of HF does not introduce additional pores into the obtained film but rather enlarges the size of the already existing ones.
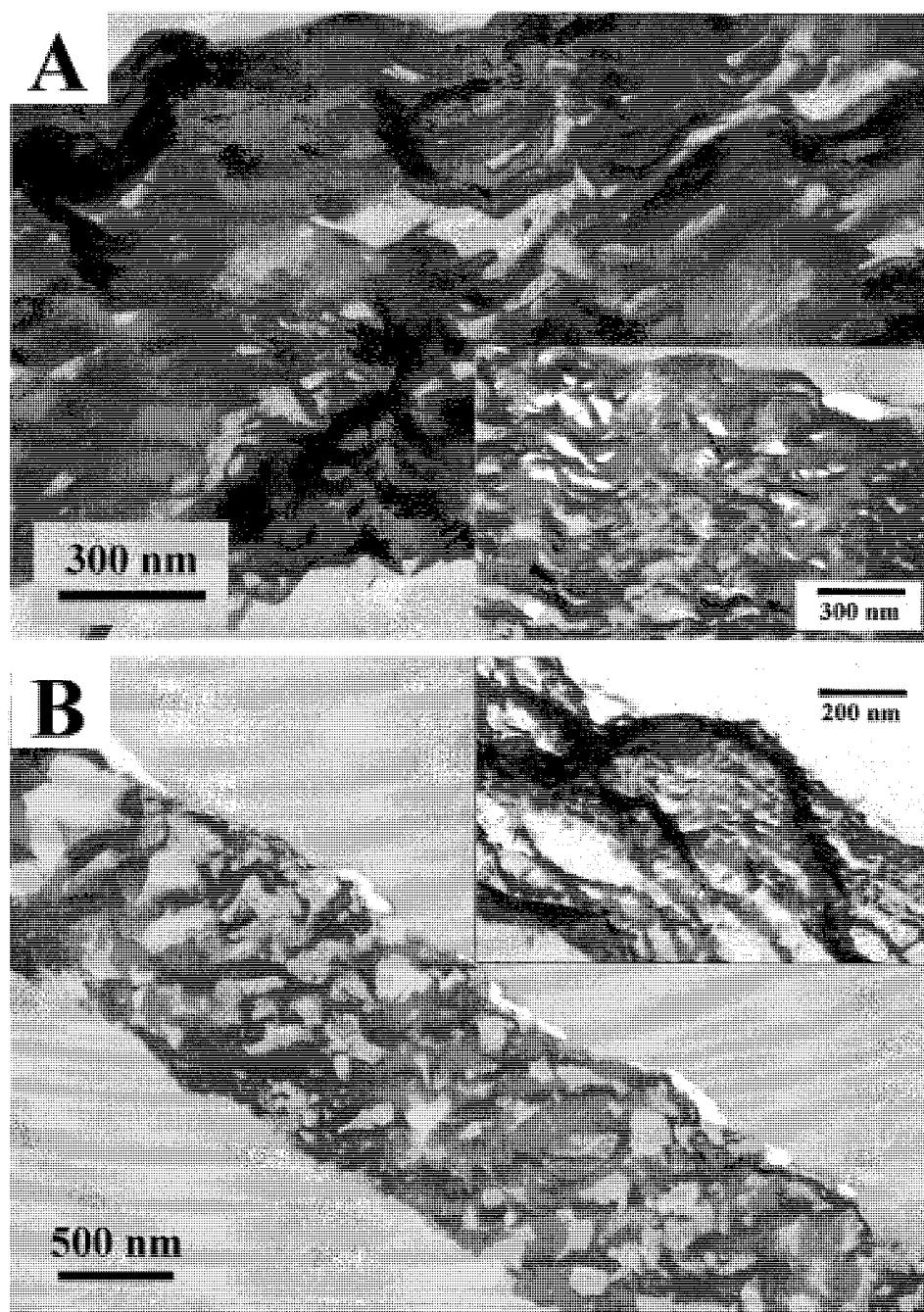
Figure 48. TEM micrographs of (PDDA/C)$_{100}$ free-standing films, prepared on (A) gallium substrate and (B) glass slide.

Figure 49. (A, B) AFM images of PDDA/C bilayer (A) before and (B) after the treatment with 0.5 % aqueous solution of HF. (C, D) Cross-sectional analysis of (A) and (B) AFM scans respectively.

Free-standing films of single wall carbon nanotubes

A free-standing carbon nanotube film has been prepared on a glass slide, followed by cross-linking and delamination after treatment with HF. The delaminated thin films of SWNT (Figure 50, insert) can easily be handled in a variety of ways and transported onto different substrates. They can be made of any desirable size or shape which is determined only by the dimensions of the substrate. The Raman scattering spectra of the separated film (Figure 50, line 3) is identical to that of the supported film and original nanotubes (Figure 50, lines 1 and 2), demonstrating that the structure of the nanotubes remain unaltered during the cross-linking and delamination. The breathing mode frequency shifts from 181 cm^{-1} in the assembled film to 183 cm^{-1} in the cross-linked free-standing film indicating a small expansion in the tube diameters.

The cross-sectional image of the free-standing film (Figure 51) clearly demonstrates the absence of micron-scale inhomogeneities although a occasional inclusion of round 30-60 nm particles can be seen. The slight variations in the gray scale contrast between the different strata shows the actual variations in the SWNT distribution within the sample. They originate from small deviations in the SWNT adsorption conditions, such as dispersion concentration and pH, during the build-up procedure. It can be noted that the top and bottom sides of the film are slightly different in roughness: the one that was adjusted to the flat surface of substrate is somewhat smoother than the "growing" side of the film. SEM microscopy images (Figure 52) show smooth and continuous surface of the sample.
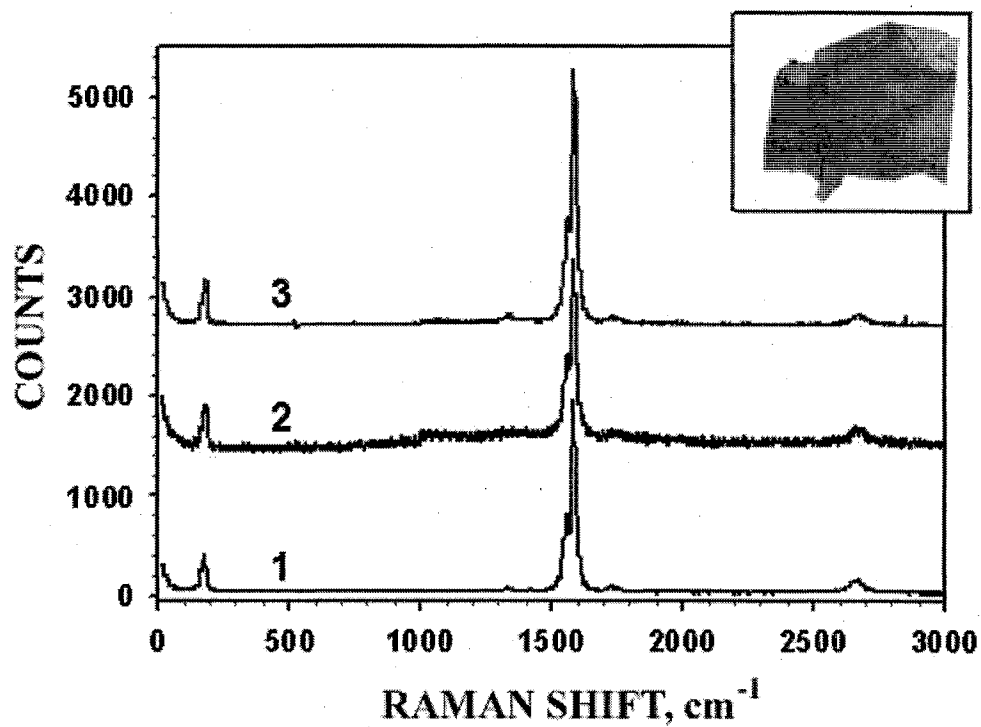
Figure 50. Raman scattering spectra of (1) SWNT dispersion, (2) LBL film on a substrate, and (3) free-standing LBL film. Insert shows optical image of free-standing carbon nanotubes film

Figure 51. Survey (A) and close-up (B) TEM images of SWNT film cross-sections. The top and bottom sides of the film are slightly different in roughness: the one that was adjusted to the flat surface of substrate is somewhat smoother that the "growing" side of the film.
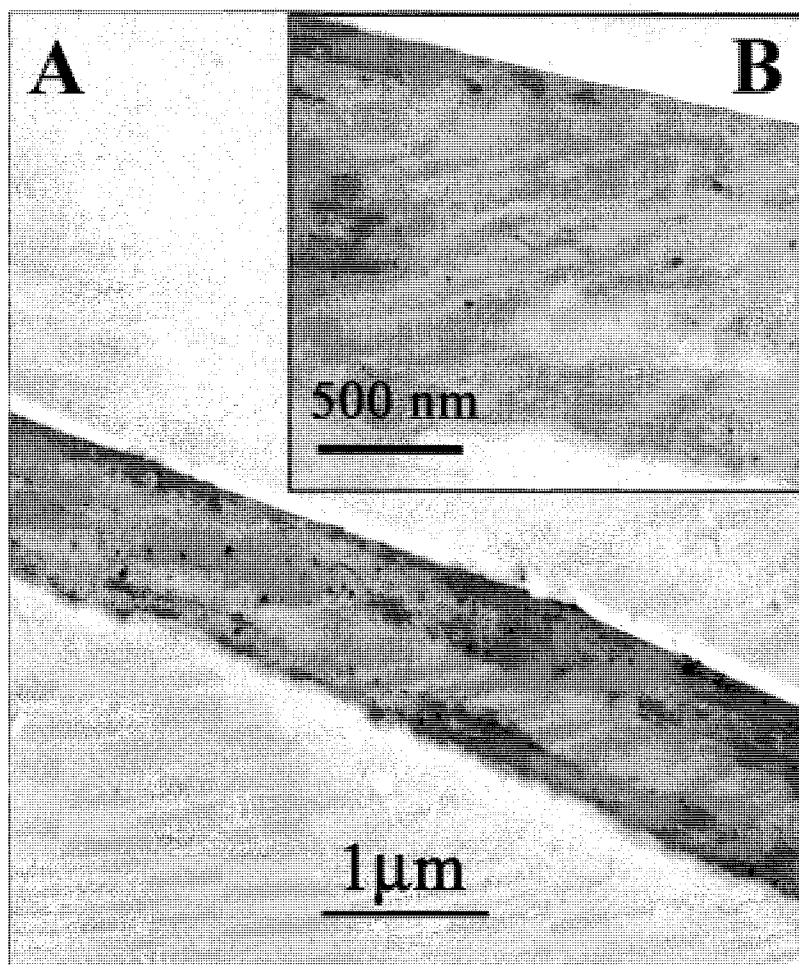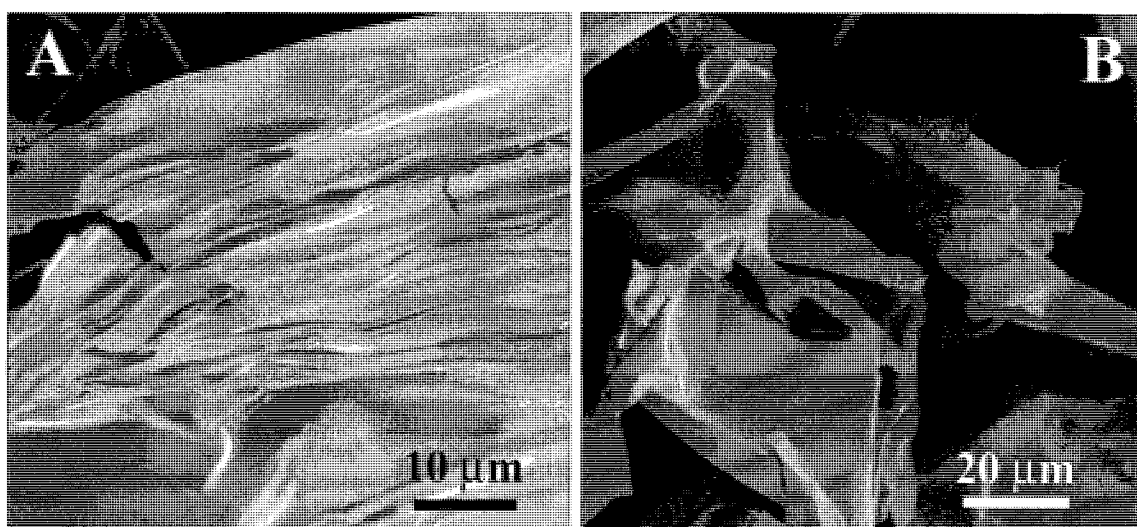
Figure 52. SEM images of the (A) surface and (B) broken edges of the SWNT free-standing LBL film.

Typically, the separation of single/multiwall carbon nanotubes and their bundles in mixed polymer composites can be observed as whiskers visible in TEM and SEM images [9,10]. Examination of the broken parts by SEM (Figure 52 B) and TEM (Figure 53) showed no evidence of a separation of the SWNT bundles from the matrix (whiskers). This can be contrasted with extensive nanotube pullout reported before by several groups [9,10]. Of all the TEM images obtained in different areas of the free-standing films, only one SWNT bundle bridging the break region was observed (Figure 53 B). The same image also shows two broken carbon fiber stubs imbedded in the walls of the crack (marked by arrows). In total, the microscopy results indicate the efficient load transfer in the LBL composite.

Tensile strength of SWNT free-standing films

The mechanical properties of the layered composites of SWNT were tested by recording the displacement and applied force by using pieces cut from ((PEI-b/PAA)(PEI-b/SWNT)$_5$)$_6$ and ((PEI-b/PAA)(PEI-b/SWNT)$_5$)$_8$ free-standing films. The obtained stress (σ) versus strain (ε) curves (Figure 54 A) differed quite markedly from the stretching curves seen previously for SWNT composites [11] and for LBL films made solely from polyelectrolytes, (PEI-b/PAA)$_{40}$, obtained by the same assembly procedure (Figure 54 B). They displayed a characteristic wave-like pattern with a gradual increase of the $d\sigma/d\varepsilon$ derivative which indicates the reorganization of the layered composite under stress. In addition, the stretching curve of the SWNT free-standing film shows a complete
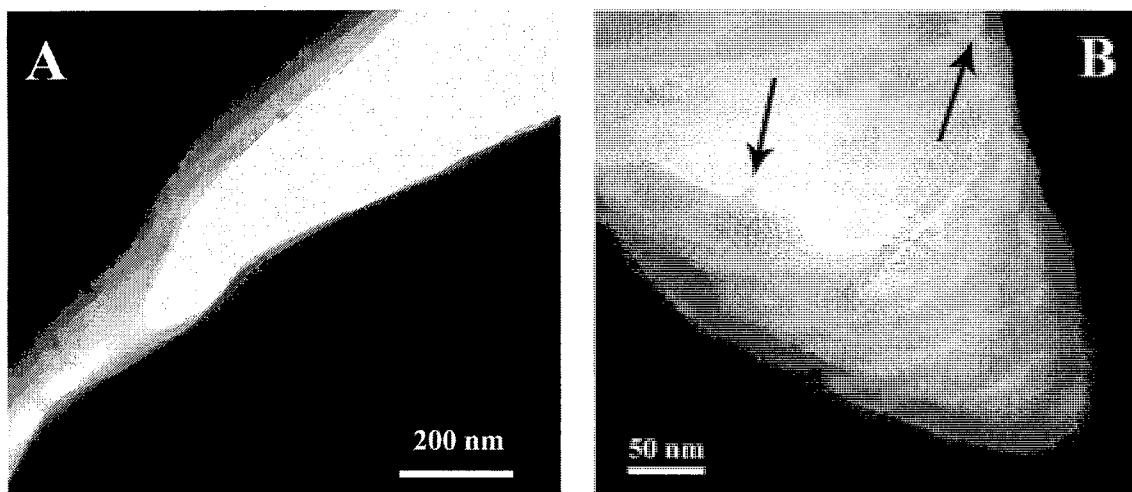
151

Figure 53. TEM images of ruptured areas of free-standing SWNT films. The arrows indicate the stubs of the broken nanotube bundles.
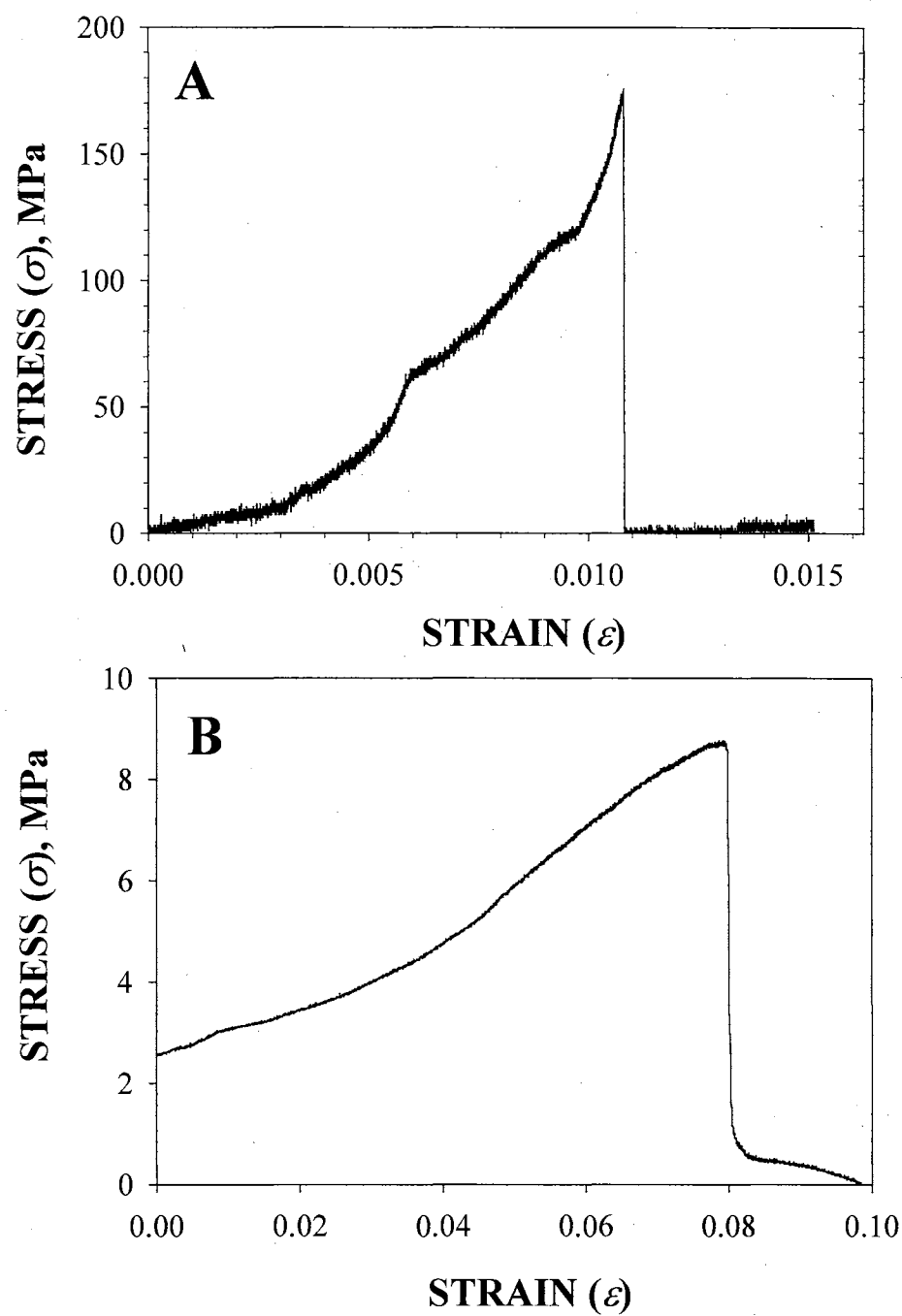
Figure 54. Typical tensile strength testing curves for (A) ((PEI-b/PAA) (PEI-b/SWNT)$_5$)$_8$ and (B) a similar free-standing film made of 50 PDDA/PAA bilayers.

absence of the plateau region for high strains corresponding to plastic deformations. This correlates well with the enhanced connectivity of the nanotubes with the polymer matrix shown by TEM and SEM measurements.

A comparison with the stretching curves for polyelectrolytes (Figure 54 B) clearly shows that the incorporation of nanotubes in the LBL structure resulted in the transfer of SWNT strength to the entire assembly. The stretching curves of the SWNT multilayers display a clear break point. The ultimate tensile strength, T, was found to be 220 +/-40 MPa with some readings being as high as 325 MPa. Table 2 shows the T values for some industrial plastics, ceramics, and recently reported composites, based on carbon fibre or SWNT. It can be noted that the T for the LBL assembled SWNT film is several times greater than the tensile strength of some strong industrial plastics. It is also substantially stronger in tensile strength than some carbon fibre composites made of 50 v.% polypropylene and 50 v.% carbon fibres. A recent study on SWNT/poly(vinylalcohol) ribbons with axially aligned nanotubes reported a tensile strength of 150 MPa [11]. The T values obtained for SWNT LBL films are, in fact, close to those of ultrahard ceramics and cermets such as tungsten monocarbide, silicon monocarbide, and tantalum monocarbide [12].

The tensile strength of single carbon nanotubes was experimentally determined to be in a range of 13 to 50 GPa [9,14]. The lower values obtained for the SWNT multilayers should be attributed mainly to the contribution of polyelectrolytes and some uncertainly in the actual cross-section area at the break point and the degree of cross-linking. Taking in account that the density of SWNT is 1.14 g/cm^3, and that the densities

Table 2. Ultimate tensile stress values (T) of selected materials [11-13]

Substance	T, MPa
Cellulose Acetate	51.70
Polycarbonate	65.48
Acrylic Resin (General Purpose, type II)	68.93
Chromium Diboride ($CrBr_2$)	730.64
Titanium Diboride (TiB_2)	126.83
Zirconium Diboride (ZrB_2)	197.82
Boron Carbide (B_4C) - 980C	155.09
Silicon Carbide (SiC) $25^{\circ}C$	137.86
Silicon Carbide (SiC) hot pressed $20^{\circ}C$	199.89
Tantalum Monocarbide (TaC) max	289.50
Titanium Monocarbide (TiC) $1000^{\circ}C$	118.56
Tungsten Monocarbide (WC)	344.64
Zirconium Monocarbide (ZrC) room	110.29
SWNT/poly(vinylalcohol) ribbons with axially aligned nanotubes (11)	150
Polypropylene filled with 50 v% carbon fibres (13)	53

of the polyelectrolytes used in multilater assembly, such as PDDA (1.04 g/cm^3) and PAA (1.14 g/cm^3) are almost the same, the volume fraction of the SWNT in the composite can be considered to be equal to the mass fraction. The mixing law predicts that a polyelectrolyte matrix with T = 9 MPa makes a negligible contribution to the strength of the composite while taking up about 50% of its volume fraction.

Additionally, the decrease in the mechanical strength of the nanotubes in the process of ionic functionalization (estimate 15 %) [15] should also be considered as a factor affecting the strength of these composites. The tuning of the molecular structure and composition of the SWNT multilayers should lead to a vast improvement in the mechanical properties approaching those of pristine carbon nanotubes.

It is also interesting to compare the T values for the SWNT composite films to those obtained for other LBL films made with inorganic components such as clay platelets and NP. The free-standing films of approximately the same thickness made of "red" CdTe nanoparticles with an internal structure of (PDDA/NP)$_{40}$ and (PDDA/C/PDDA/NP)$_{30}$ displayed a T equal to 40 MPa and 72 MPa respectively. This fact led to the conclusion that inorganic or SWNT components act as "molecular armor" in the layered composites by significantly reinforcing them.

Conclusion

The layer-by-layer assembly technique allows for the preparation of free-standing composite structures, the architecture of which can be controlled on the nanometer scale. This method of preparation can be extended to a variety of other compounds utilized in LBL research, such as polymers, proteins, dyes, metal and semiconductor nanoparticles,

vesicles, viruses, DNA, and others. Different colloids will lead to a palette of thin film materials and membranes whose functional properties can be tuned by varying the layer sequence. Such free-standing membranes can be a unique component of a variety of long-life-time devices ranging from automobile engines to advanced prosthesis.

LBL assembled free-standing films of various architectures made from nanoparticles of magnetite and CdTe, as well as from carbon nanotubes, have been prepared. The introduction of clay interlayers into the nanoparticle film leads to an overall increase in its mechanical properties. Anisotropy in physical damage, caused by diamond knife during the cross-section procedure, was observed for clay and PAA substituted materials.

It was shown that several different substrates, such as cellulose acetate, glass slides or silicon wafers, and metallic Ga, can be used in free-standing films preparation. The choice of substrate is determined by the compounds used in LBL process and the desired structure or resulting multilayer stack. The porosity of the free-standing membrane can be tuned during the substrate removal step.

The high structural homogeneity and interconnectivity in the structural components of the LBL films combined with high SWNT loading leads to a significant improvement in mechanical properties of the SWNT composites. Additional cross-linking of resulting film during and after the LBL growth step makes it possible to obtain a free-standing film with an ultimate stress value close to that of some industrial ultrahard ceramics and cermets.

References

1. Caruso, F.; Caruso, R. A.; Mohnwald, H. *Science* **1998,** *282*(5391), 1111-1114.

2. Caruso, F.; Lichtenfeld, H.; Giersig, M.; Moehwald, H. *J.Am.Chem.Soc.* **1998,** *120*(33), 8523-8524.

3. Schlenoff, J. B.; Ly, H.; Li, M. *J. Amer. Chem. Soc.* **1998,** *120* 7626-7634.

4. Mohwald, H.; Lichtenfeld, H.; Moya, S.; Voigt, A.; Baumler, H.; Sukhorukov, G.; Caruso, F.; Donath, E. *Macromol.Symp.* **1999,** *145*(Polymer Sorption Phenomena), 75-81.

5. Kotov, N. A.; Magonov, S.; Tropsha, E. *Chem. Mater.* **1998,** *10* (3), 886-895.

6. Sullivan, D. M.; Bruening, M. L. *J. Amer. Chem. Soc. 123*(47), 11805-11806.

7. Olde Damink, L. H. H.; Dijkstra, P. J.; Van Luyn, M. J. A.; Van Wachem, P. B.; Nieuwenhuis, P.; Feijen, J. *Journal of Materials Science: Materials in Medicine* **1995,** *6*(8), 460-472.

8. Kotov, N. A.; Haraszti, T.; Turi, L.; Zavala, G.; Geer, R. E.; Dekany, I.; Fendler, J. H. *J. Amer. Chem. Soc.* **1997,** *119* 6821-6832.

9. Li, F.; Cheng, H. M.; Bai, S.; Su, G.; Dresselhaus, M. S. *Applied Physics Letters* **2000,** *77*(20), 3161-3163.

10. Qian, D.; Dickey, E. C.; Andrews, R.; Rantell, T. *Applied Physics Letters* **2000,** *76*(20), 2868-2870.

11. Vigolo, B.; Penicaud, A.; Coulon, C.; Sauder, C.; Pailler, R.; Journet, C.; Bernier, P.; Poulin, P. *Science* **2000,** *290*(5495), 1331-1334.

12. CRC Materials Science and Engineering Handbook. CRC, Boca Raton, FL **(1992).**

13. Fu, S. Y.; Lauke, B.; Mader, E.; Yue, C. Y.; Hu, X.; Mai, Y. W. *Journal of Materials Science* **2001,** *36*(5), 1243-1251.

14. Yu, M. F.; Files, B. S.; Arepalli, S.; Ruoff, R. S. *Physical Review Letters* **2000,** *84*(24), 5552-5555.

15. Garg, A.; Sinnott, S. B. *Chemical Physics Letters* **1998,** *295*(4), 273-278.

CHAPTER VI

CONCLUSIONS AND FUTURE RESEARCH DIRECTIONS

The research, presented in this work, has shown that layer-by-layer (LBL) assembly provides an extremely versatile method for the preparation of thin films. The structure of the growing LBL stack and its physical and chemical properties are tunable and customizable through the choice of materials, assembly conditions, and dipping order. This method can be easily applied to a wide range of organic and inorganic materials, which gives the possibility of preparing composite films with wide spectra of possible applications.

Chapter II introduced the conditions and mechanism of LBL growth of magnetic nanoparticle films. While the magnetite films displayed a "normal" sandwich-like growth mechanism, where complete coverage of the substrate surface of the previously deposited layer occurs at each deposition step, yttrium iron garnet (YIG) nanoparticles (NP) films grow in a domain expansion mode. To switch the growth mechanism for YIG it was necessary to modify the nanoparticle surface with 3-aminopropyltrimetoxysilane to form a positively charged shell around each particle. The hydrocarbon chain attached to the NP resulted in the interaction of similar groups of the polymer while the surface charge prevented coagulation of the colloidal solution.

The possibility of controlling the structure of the growing LBL multilayers was demonstrated in Chapter III. For this task, thiol-capped semiconductor CdTe

160

nanoparticles have been used. Their size-dependent luminescent properties make it possible to prepare asymmetric films without significant adjustment of the assembly conditions when a new type of NP is introduced. The LBL films, consisting of 5-10 layers of each "green", "yellow", "orange", and "red" CdTe nanoparticles with average sizes ranging from 2-3 nm for "green" and 5-6 nm for "red" nanoparticles, have been analyzed by TEM and confocal microscopy. A graded structure in the obtained films was clearly demonstrated.

Nanomaterials with aspect ratios (width to length ratio) different from 1, such as single wall carbon nanotubes (SWNT), can be assembled in multilayers. In Chapter IV conditions for such assembly and alignment of SWNT inside of a monolayer were demonstrated. It was shown, that it is possible to obtain composite materials with a weight load of SWNT up to 50% utilizing the LBL assembly method. In addition, the reversible dependence of the resistivity of the SWNT multilayers on the humidity of the surrounding media was demonstrated.

Chapter V introduced the possibility of preparing free-standing LBL assembled films. The universality of this method, the possibility of its use on several different substrates, and the conditions for their complete removal, have been shown. It also was demonstrated in Chapter V that the introduction of clay interlayers into the structure leads to an overall increase in its mechanical properties. Anisotropy in physical damage, caused by a diamond knife during a cross-section procedure, was observed for clay and PAA substituted materials. Tensile stress measurements have been performed for SWNT free-standing films. It was shown that the ultimate stress value for such assembles is close to some industrial ultrahard ceramics and cermets.

161

In summary, the versatility of the LBL method for thin films of nanocolloids was demonstrated. A variety of inorganic nanomaterials, including nanoparticles, nanosheets, and nanotubes, can be assembled into films utilizing this method. The possibility of free-standing films preparation was demonstrated. The internal structure of the growing films and subsequently their physical properties can be controlled at each deposition step through the assembly conditions and materials used.

For future research three major directions can be highlighted. (1) Further study and preparation of asymmetric assemblies with some finely-tuned parameters, such as the polarizability and the refractive index on the molecular level in asymmetric assemblies. This most possibly will lead to the discovery of unique photonic and electronic devices. (2) The preparation of SWNT LBL films, in which all the nanotubes are aligned in one direction. Exploitation of such assembles may show their unique properties as semiconducting materials. Free-standing films from aligned SWNT will possibly exhibit mechanical properties exceeding ones reported in this work. Finally, (3) utilization of biological materials in LBL deposition will give the possibility of preparing a wide number of artificial films and membranes, ranging from artificial skin to cell walls and blood vessels.

VITA

Arif A. Mamedov 2

Candidate for the Degree of

Doctor of Philosophy

Thesis: LAYER-BY-LAYER ASSEMBLED THIN FILMS OF NANOCOLLOIDS

Major Field: Chemistry

Biographical:

Personal Data: Born in Minsk, Belarus, On June 21, 1973

Education: Graduated from 148th Middle School, Minsk, Belarus in June 1990; received Diploma with Honors (equivalent of Master of Science) in Chemistry from Belarussian State University, Minsk, Belarus in June 1995; completed the requirements for the Doctor of Philosophy degree with a major in Chemistry at Oklahoma State University in December, 2002.

Experience: Employed as an undergraduate research assistant at Chemistry Department of Belarussian State University, Minsk, Belarus, 1992-1994; employed as research assistant at the Institute of Physial-Chemical Problems of Belarussian State University, Minsk, Belarus, 1994-1998; held the position of a production manager at Kontrast-M, Ltd., Minsk, Belarus, 1995-1998; employed by Oklahoma State University, Chemistry Department as a graduate teaching assistant and as a graduate research assistant; 1999-present.

Professional Memberships: Oklahoma Microscopy Society, American Chemical Society.